

Photophysical and Optoelectronic
Properties of Pristine, Doped and Surface-
Functionalized Two-Dimensional Zinc
Oxide Nanostructures

by

Jung-Soo Kang

A thesis
presented to the University of Waterloo
in fulfillment of the
thesis requirement for the degree of
Doctor of Philosophy
in
Chemistry

Waterloo, Ontario, Canada, 2016

© Jung-Soo Kang 2016

AUTHOR'S DECLARATION

I hereby declare that I am the sole author of this thesis. This is a true copy of the thesis, including any required final revisions, as accepted by my examiners.

I understand that my thesis may be made electronically available to the public.

Abstract

As one of the most studied transparent conducting oxides, zinc oxide (ZnO) has received a lot of attention due to its physical, chemical, optical and optoelectronic properties. The present study focusses on the photophysical and optoelectronic properties of ZnO nanostructures, specifically two-dimensional nanostructures. Three types of experiments that involve (a) controlling the size of ZnO nanostructures, (b) inducing impurities into ZnO nanostructures, and (c) surface functionalization by lanthanoid/organic complexes were performed.

It is well known that the thickness has a great influence on the properties of nanostructures. Single-unit-cell thick (0.52 nm), n-type ZnO quantum sheets have been deposited on a p-type Si(100) substrate in an aqueous solution at low temperature (near 0 °C) by a facile electrochemical method without any pre- and post-treatment. Due to the extremely small thickness of ZnO quantum sheets, the quantum confinement effect was found to increase the energy band gap to 4.51 eV, more than 1.1 eV higher than its bulk value. These ZnO quantum sheets were found to produce deep UV (276 nm) and blue photoluminescence emission bands, which enabled qualitative description of the electronic band structure under the influence of quantum confinement effect. Increasing the deposition time caused individual quantum sheets grown in the [100] direction to stack onto one another rather than becoming thicker. This ZnO stacked quantum sheets provided a tunable band gap for this new type of ultrathin two-dimensional nanomaterials that promise new nanoelectronic applications.

With the goal to obtain better optical and optoelectronic properties for light emitting diodes and photodetectors, rare earth transition metal ions, specifically trivalent europium and terbium cations, were embedded into ZnO nanostructures. Europium-doped ZnO nanowall structures have also been achieved by a simple electrochemical deposition method. Upon Eu(III) embedment, the nanowalls were found to become thicker and stacked. X-ray photoelectron spectroscopic study revealed that Zn(OH)₂ was more dominant than ZnO near the surface and the depth-profiling data confirmed that Eu(III) was uniformly distributed in the ZnO-Zn(OH)₂ core-shell structure. We also measured and compared the photoluminescence spectra of as-grown, post-annealed, and 1,10-phenanthroline surface-functionalized europium-doped ZnO nanowalls. Thermal treatment and surface functionalization of europium-doped ZnO generated hypersensitive 620 nm emission (⁵D₀ → ⁷F₂), which led us to propose a unique cascade energy transfer mechanism between ZnO, 1,10-phenanthroline and Eu(III) ion. Hypersensitive green emission at 545 nm (⁵D₄ → ⁷F₅) was also

observed in ZnO nanowalls embedded with the trivalent terbium cations without any post-growth treatment. Photoluminescence emission of terbium was further found to increase up to 10 times by plasmonic effect introduced by surface functionalization with noble-metal nanoparticles. The Tb emission was examined for potential chemosensor application for Rhodamine B by a plausible cascade energy transfer mechanism from ZnO to Rhodamine B via trivalent terbium cations.

In order to modify photophysical properties of ZnO, europium and terbium complexes based on oxydiacetic acid and 1,10-phenanthroline were synthesized and used to surface-functionalize ZnO nanowalls. Excitation spectra showed energy transfer between the rare-earth transitional metal organic complexes and ZnO. These two different types of hybrid complexes exhibited maximum energy transfer efficiency of up to 90%. X-ray photoelectron spectroscopy revealed the chemisorption nature between lanthanoid complexes and ZnO. These data also confirmed that the coordination nature of lanthanoid cations remained unchanged from that in pristine powders. This study provides unique opportunities to understand the interactions between metal oxides and chelating organic molecules.

In this thesis, two-dimensional ZnO nanostructures, particularly nanowalls and quantum sheets, were synthesized by adopting an aqueous solution based electrochemical deposition technique. Single-unit-cell thick ZnO quantum sheets were successfully grown on a Si wafer, and they exhibited properties under quantum-confinement effects, including strong blue-shift of luminescence bands and dramatically widening of the energy band gap. Extensive photophysical investigation of trivalent europium cation embedment led to the development of new cascade energy transfer mechanism between europium cations and ZnO. Terbium-doped ZnO nanowalls produced characteristic emissions without any pre- or post-growth treatment, and they demonstrated chemosensing capability. Surface functionalization of ZnO nanowalls with lanthanoid complexes suggested a convenient way to modify the emission properties of ZnO, which provided insight into interactions between ZnO nanostructures and organic molecules. The present thesis therefore offered better understanding of not only optoelectronic and photophysical properties of transparent conducting semiconductors under quantum confinement in one direction, but also the effect of the dopant and surface functionalization on modifying the photophysical properties. These results could provide a new approach to design appropriate photophysical properties of other metal oxides for chemosensing and light emitting electronics.

Acknowledgements

First, I would like to express my sincerest appreciation to my PhD supervisor, Prof. Kam Tong Leung for his full support throughout my PhD program. His complete dedication to the academia and research not only supported my research but also provided me a turning point and led me to the fascinating world of science and research. I would also like to thank members of my PhD advisory committee: Prof. Juewen Liu (Department of Chemistry, University of Waterloo), Prof. Zhongwei Chen (Department of Chemical Engineering, University of Waterloo) and Prof. Paul Rowntree (Department of Chemistry, University of Guelph) for their invaluable feedbacks and comments on the work.

It is my great pleasure to thank all members of Waterloo Advanced Technology Laboratory (WATLab). Collaborating and discussing different aspects of my research with Dr. Joseph Thomas, Dr. Nina Heinig, Dr. Lei Zhang and Dr. Shanti Rout were very helpful and fruitful. I am also truly appreciative to Prof. Jun-Gill Kang, Dr. Yong-Kwang Jeong and Ms. A-Ri Ham at Chungnam National University (Daejeon, South Korea) for their help to use their unique luminescence measurement setup. I am also grateful to Prof. Youngku Sohn (Yeungnam University, South Korea) and Dr. Jae-Sun Jung (Soulbrain Sigma-Aldrich) for their collaboration. I am also thankful to Dr. Siyoung Oh (Korea Institute of Science and Technology) and Dr. Taeun Yim (Korea Electronics Technology Institute) for their support.

Last but not least, I would like to give my sincere gratitude to my parents and my younger brother for their unlimited support, and their love for strengthening me to accomplish my goals.

Table of Contents

AUTHOR'S DECLARATION.....	ii
Abstract.....	iii
Acknowledgements.....	v
Table of Contents.....	vi
List of Figures.....	ix
List of Tables.....	xiv
Chapter 1 Introduction.....	1
1.1 Transparent Conducting Oxides.....	1
1.2 Zinc Oxide.....	3
1.2.1 Properties of Zinc Oxide.....	3
1.2.2 Deposition Methods.....	5
1.2.3 Applications.....	6
1.3 Properties of Rare-Earth Transition Metals and Its Applications.....	9
1.3.1 Luminescence Properties of Rare-Earth Transition Metal Materials.....	9
1.3.2 Judd-Ofelt Theory.....	12
1.3.3 Characteristics of Europium and Terbium Emissions.....	14
1.3.4 Energy Transfer and Sensitization Mechanism.....	15
1.3.5 Application of Rare-Earth Transition Metals and Its Complexes.....	18
1.4 Scope of the Present Work.....	18
Chapter 2 Experimental Section.....	21
2.1 Electrochemical Deposition for Sample Fabrication.....	21
2.2 Scanning Electron Microscopy, Transmission Electron Microscopy and Atomic Force Microscopy.....	22
2.3 X-ray Photoelectron Spectroscopy and Auger Electron Spectroscopy.....	25
2.4 UV-Vis Spectroscopy.....	28
2.5 Luminescence Spectroscopy.....	29
2.5.1 Photoluminescence and Excitation Measurement.....	29
2.5.2 Lifetime and Absolute Quantum Yield Measurement.....	31
Chapter 3 Optoelectronic and Photophysical Properties of Zinc Oxide Quantum Sheets.....	33
3.1 Introduction.....	33
3.2 Experimental Details.....	34

3.2.1 Fabrication of ZnO Quantum Sheets	34
3.2.2 Characterization Methods.....	34
3.3 Results and Discussion.....	35
3.3.1 Morphology and Topography of ZnO Quantum Sheets.....	35
3.3.2 Chemical Analysis of ZnO Quantum Sheets.....	38
3.3.3 Optoelectronic and Photophysical Properties of ZnO Quantum Sheets.....	39
3.4 Summary	44
Chapter 4 Observation of Mediated Cascade Energy Transfer in Europium-doped ZnO Nanowalls by 1,10-Phenanthroline	45
4.1 Introduction	45
4.2 Experimental Section.....	46
4.3 Results and Discussion.....	47
4.3.1 Morphologies of Eu-doped ZnO Nanowalls	47
4.3.2 Chemical Analysis of Eu-doped ZnO Nanowalls.....	48
4.3.3 Photoluminescence Measurement of Eu-doped ZnO Nanowalls	50
4.3.4 Surface Modification of Eu-doped ZnO nanowalls by 1,10-phenanthroline.....	52
4.3.5 Cascade Energy Transfer Mechanism	55
4.4 Summary	58
Chapter 5 Extraordinary Enhanced Emission of Terbium-doped ZnO Nanowalls and Rhodamine B Detection by Cascade Energy Transfer	59
5.1 Introduction	59
5.2 Experimental Details	60
5.2.1 Chemicals	60
5.2.2 Fabrication of Terbium-Doped ZnO Nanowalls.....	60
5.2.3 Use of Noble Metal Nanoparticles for Localized Surface Plasmon Resonances	61
5.2.4 Surface Modification by Rhodamine B	61
5.2.5 Sample Characterization and Spectroscopic Measurements	61
5.3 Results and Discussion.....	62
5.3.1 Morphologies, Chemical Composition and Structural Analysis of Terbium-doped ZnO Nanowalls.....	62
5.3.2 Photophysical Properties of Terbium-Doped ZnO Nanowalls.....	65
5.3.3 Surface Modification by Rhodamine B	71

5.3.4 Energy Transfer Mechanism of Terbium-Doped ZnO Nanowalls and Hybrid Structure With Rhodamine B	72
5.4 Summary	73
Chapter 6 Photophysical and Interfacial Properties of Rare Earth Transition Metal Complex/ZnO Nanowall Hybrid Structures: Energy Transfer from ZnO to Rare Earth Transition Metal	75
6.1 Introduction.....	75
6.2 Experimental Details.....	77
6.2.1 Chemicals.....	77
6.2.2 Fabrication of ZnO Nanowalls.....	77
6.2.3 Synthesis of Lanthanoid Complexes.....	77
6.2.4 Characterization	77
6.3 Results and Discussion	78
6.3.1 Photoluminescence Measurement of Lanthanoid Complexes	78
6.3.2 PL and Excitation Spectra of Lanthanoid Complex/ZnO Nanowall Hybrid Structures	81
6.3.3 Energy Transfer Mechanisms	84
6.3.4 Energy Transfer Efficiency and Absolute Quantum Yield	87
6.3.5 Investigation of the Interfacial area of Lanthanoid Complex/ZnO Nanowall Hybrid Structures	88
6.3.6 Comparison between Doping and Surface-Functionalization.....	91
6.4 Summary	91
Chapter 7 Concluding Remarks and Outlook	93
7.1 Conclusions.....	93
7.2 Proposed Future Work	95
References.....	97
Appendix A Copyright Permissions	122

List of Figures

Figure 1.1 Stick-and-ball representation of ZnO crystal structures: (a) cubic rocksalt, (b) cubic zinc blende, and (c) hexagonal wurtzite. The shaded gray and black spheres denote Zn and O atoms, respectively.....	3
Figure 1.2 Room-temperature photoluminescence spectra of as-grown ZnO nanorods and ZnO nanorods postannealed at 200, 400 and 600 °C in (a) air and (b) forming gas (90% N ₂ /10% H ₂), and of ZnO nanorods annealed in different atmospheres at (c) 200 °C and (d) 600 °C.....	4
Figure 1.3 Energy levels (in eV) of different defects between the conduction band minimum (E _C) and valence band maximum (E _V) in ZnO. V _{Zn} , V _O , Zn _i , O _i and H _i denote zinc and oxygen vacancies, and zinc, oxygen and hydrogen interstitials, respectively. V _O Zn _i indicates a complex of oxygen vacancy and zinc interstitial.	5
Figure 1.4 Scanning electron micrographs of (a, b) ZnO nanowalls, (c, d) nanodisks, (e, f) nanospikes, and (g, h) nanopillars electrochemically grown on ITO-glass at 70 °C with 0.1 M KCl solution and varying Zn(NO ₃) ₂ ·6H ₂ O concentrations of 0.1, 0.05, 0.01, and 0.001 M, respectively. Insets show the corresponding cross sectional images.	7
Figure 1.5 Scanning electron micrographs of hydrothermally grown ZnO nanowires illustrating (a) length growth (to 1, 2, and 3 times of the original length), and seed effect with first-generation branched growth (b) without and (c) with seeds after polymer removal. Polyethylenimine removal effect is shown with first-generation branched growth (d) without and (e) with polymer removal after nanoparticle seed deposition. Polymers on ZnO nanowires are removed by heating at 350 °C for 10 min.....	8
Figure 1.6 Partial energy level diagrams for the lanthanide aquo ions. The main excited-state energy levels are drawn in red while the (lower-state) final levels and ground-state energy levels are indicated in pale blue and navy blue, respectively. ⁷⁷⁻⁸¹ The Eu and Tb diagrams are highlighted for future references to our studies presented in Chapters 4, 5 and 6.	11
Figure 1.7 Schematic diagram of sensitization of lanthanoid complexes. Nonradiative transition and nonradiative relaxation are represented by zigzag and dotted lines, respectively. The ligand must undergo intersystem crossing (ISC) between the S ₁ and T ₁ states in order to enable the energy transfer (ET) between the ligand and the lanthanoid. The latter step leads to the observed characteristic lanthanoid emission.....	17
Figure 1.8 A schematic diagram of Dexter energy transfer mechanism between the ligand (L) and the metal cation (M).	17

Figure 2.1(a) A standard three-electrode electrochemical deposition setup with (b) a Pt wire counter electrode, a substrate used as the working electrode, and a Ag/AgCl reference electrode.	21
Figure 2.2 Photographs of (a) a Zeiss Merlin field-emission scanning electron microscope, and (b) a Zeiss Libra 200MC transmission electron microscope.	24
Figure 2.3 Photograph of a Digital Instruments Dimension 3100 Scanning Probe Microscope used for atomic force microscopy.	25
Figure 2.4 Schematic diagram of photoelectron and Auger electron emission processes.	26
Figure 2.5 Photographs of (a) a Thermo-VG Scientific ESCALab 250 Microprobe used for photoelectron spectroscopy and (b) a Thermo Microlab 350 used for Auger electron spectroscopy. .	27
Figure 2.6 Photograph of (a) Perkin Elmer Lambda 1050 UV-Vis spectrophotometer and (b) the integrating sphere module used for diffuse reflectance measurement.	28
Figure 2.7 Photograph of the experimental setup depicting the light path (dotted lines) from the incident beam optics (right) to the sample chamber (center) to the exit beam optics (left).	30
Figure 2.8 A schematic diagram of measurement setup for photoluminescence (emission) and excitation spectra.	31
Figure 2.9 A schematic diagram of the photoluminescence lifetime measurement setup.	32
Figure 3.1 SEM images of electrochemically deposited ZnO quantum sheets for (a) 1 min, (b) 5 min, (c) 30 min, and (d) 60 min.	35
Figure 3.2 (a) AFM image of single-unit-cell thick ZnO quantum sheets deposited directly on a Si substrate and (b) its sectional analysis along the linescan marked by the white line in (a). (c) TEM and (d) HRTEM images of ZnO quantum sheet stacks. (e) Schematic molecular model of two layers of single-unit-cell thick ZnO quantum sheets.	37
Figure 3.3 XPS spectra of (a) Zn 2p, (b) O 1s, and (c) Cl 2p as a function of sputtering time from 0 s (i.e. as-deposited), to 60 s, 180 s, 600 s and 1800 s for electrochemically deposited ZnO quantum sheets obtained with 60 min deposition time. (d) O 1s XPS spectrum of a ZnO powder sample.	39
Figure 3.4 UV absorption spectra of ZnO quantum sheets electrodeposited on Si for various deposition times (absorption cut-offs are marked with black vertical markers) and of ZnO bulk powder (left inset). Right inset shows the photograph of ZnO quantum sheets on Si exposed to UV light (at 254 nm).	41
Figure 3.5 Emission spectra ($\lambda_{\text{exn}} = 240$ nm) and excitation spectrum (inset, $\lambda_{\text{ems}} = 450$ nm) of ZnO quantum sheets (lower) and nanowalls (upper). Blue shifts for the band edge and defect emissions between the ZnO quantum sheets and nanowalls are marked.	41

Figure 3.6 (a) XPS valence band spectra of ZnO bulk powder (black) and quantum sheets (red) and (b) schematic diagram of the valence band maxima and conduction band minima of ZnO bulk and quantum sheets.	42
Figure 4.1 SEM images of ZnO nanowalls deposited at 70 °C on ITO-glass in (a) 0.10 M Zn(NO ₃) ₂ ·6H ₂ O mixed with 0.10 M KCl, and with additional (b) 0.01 M, (c) 0.05 M and (d) 0.10 M Eu(NO ₃) ₃ ·5H ₂ O.	47
Figure 4.2 XPS spectra of (a) Eu 3d, (b) Zn 2p and (c) O 1s regions of as-deposited Eu-embedded ZnO nanowalls before sputtering and with a total sputtering time of 1000 s, 2000 s and 3000 s.	49
Figure 4.3 (a) PL (with λ _{exn} = 325 nm) and excitation (exn) spectra (with λ _{ems} = 590 nm) of ZnO:Eu(III) nanowalls obtained with various Eu(III) concentrations, and (b) PL (with λ _{exn} = 325 nm) spectrum of thermally treated ZnO:Eu(III) with 0.10 M Eu(III) concentration.	51
Figure 4.4 PL spectra (λ _{exn} = 325 nm) of (a) as-grown ZnO:Eu(III) nanowalls sample surface-functionalized with 0.010 M phen, and annealed samples surface-functionalized (b) without and with (c) 0.010 M, (d) 0.050 M and (e) 0.10 M of phen.	53
Figure 4.5 PL (λ _{exn} = 325 nm) and excitation (exn) spectra (λ _{ems} = 614 nm) of [Eu(phen) ₂]·(NO ₃) ₃ ... 54	
Figure 4.6 PL spectra (with λ _{exn} = 325 nm) of postannealed ZnO:Eu(III) nanowalls (a) without and with surface-functionalization of (b) 0.01 M and (c) 0.1 M of ethylenediamine.	55
Figure 4.7 A schematic model for the cascade energy transfer of phen-modified ZnO:Eu(III) nanowalls.	56
Figure 4.8 Energy level diagrams for (a) annealed ZnO:Eu(III) nanowalls and (b) the cascade energy transfer mechanism in the phen-modified ZnO:Eu(III) nanowalls.	57
Figure 5.1 SEM image of (a) pristine ZnO nanowalls and Tb-doped ZnO nanowalls obtained with Tb(III) concentrations of (b) 1 mM, (c) 5 mM and (d) 10 mM.	62
Figure 5.2 (a) SEM image and (b) background-subtracted Auger electron spectra of three different locations marked in (a) for as-deposited Tb-doped ZnO nanowalls obtained with Tb(III) concentration of 10 mM. XPS spectra of (c) Tb 3d and (d) O 1s regions for as-grown Tb-doped ZnO nanowalls and upon sputtering for 1000 s, 2000 s, 3000 s, and 4000 s.	64
Figure 5.3 TEM and HRTEM (inset) images of Tb-doped ZnO nanowalls obtained with Tb(III) concentration of 10 mM.	64
Figure 5.4 (a) PL spectra (λ _{exn} = 325 nm) of Tb-doped ZnO nanowalls obtained in electrolyte of Zn ²⁺ concentration of 0.1 M and with 1 mM, 5 mM and 10 mM Tb(III) concentration, and (b) excitation	

spectra ($\lambda_{\text{ems}} = 545 \text{ nm}$) of the Tb-doped ZnO nanowalls obtained with 10 mM Tb(III) concentration measured at 10, 70, 150 and 300 K.....	66
Figure 5.5 (a) Time profiles of the visible emissions ($\lambda_{\text{exn}} = 337.1 \text{ nm}$) at 535, 545, 560, and 600 nm from Tb-doped ZnO nanowalls obtained with 10 mM Tb(III) concentration, and (b) curve-fitting of the time profile measured with $\lambda_{\text{ems}} = 545 \text{ nm}$	68
Figure 5.6 PL spectra ($\lambda_{\text{exn}} = 325 \text{ nm}$) of Tb-doped ZnO nanowalls decorated with the appropriate amounts of (a) Ag NPs, (b) Pt NPs, and (c) Au NPs to exhibit the maximal LSPR effect (with the same Y-scale) compared with untreated Tb-doped ZnO nanowalls. Insets show the corresponding PL spectra after subtracting the broad backgrounds.	70
Figure 5.7 Emission spectra ($\lambda_{\text{exn}} = 325 \text{ nm}$) of Tb-doped ZnO nanowalls without and with 1 and 3 drops of Rhodamine B (RhB) treatment. These spectra have been normalized at their respective maximum band intensities.	71
Figure 5.8 Energy-level diagrams illustrating the energy transfer mechanisms between (a) ZnO nanowalls and dopant Tb(III), resulting in the ZnO near band gap emission (at 376 nm) and several characteristic Tb(III) emissions in the visible range, and (b) ZnO:Tb(III) nanowalls and Rhodamine B (RhB) producing the red emission from the RhB/ZnO:Tb(III) nanowall hybrid structure.....	73
Figure 6.1 Excitation spectra (blue lines, 200-500 nm) with (a) $\lambda_{\text{ems}} = 614.4 \text{ nm}$ for EuPhen and (b) $\lambda_{\text{ems}} = 595 \text{ nm}$ for EuODA powders and emission spectra (black lines, 400-700 nm) with (a) $\lambda_{\text{exn}} = 350 \text{ nm}$ for EuPhen and (b) $\lambda_{\text{exn}} = 396 \text{ nm}$ for EuODA powders. Magnetic dipole transition ($^5D_0 \rightarrow ^7F_1$) of Eu is shown in inset of (a). (c, e) Schematic molecular structures and (d, f) photographs under UV illumination at 365 nm of (c, d) EuPhen and (e, f) EuODA.....	80
Figure 6.2 Excitation (blue, 200-500 nm) with (a) $\lambda_{\text{ems}} = 540.6 \text{ nm}$ for TbPhen and (b) $\lambda_{\text{ems}} = 541.6 \text{ nm}$ for TbODA, and emission spectra (black, 400-700 nm) with (a) $\lambda_{\text{exn}} = 350 \text{ nm}$ for TbPhen and (b) $\lambda_{\text{exn}} = 354 \text{ nm}$ for TbODA. (c, e) Schematic molecular structures and (d, f) photographs under UV illumination at 365 nm of (c, d) TbPhen and (e, f) TbODA.	81
Figure 6.3 PL spectra ($\lambda_{\text{exn}} = 325 \text{ nm}$) of ZnO nanowalls surface-functionalized with increasing amounts of (a) EuPhen, (b) EuODA, (c) TbPhen and (d) TbODA, with the corresponding excitation spectra ($\lambda_{\text{ems}} = 614.4, 595, 540.6, \text{ and } 541.6 \text{ nm}$) for the respective samples shown as insets.	83
Figure 6.4 (a) A spectroscopic representation of processes involved in the cascade energy transfer from ZnO to EuPhen or TbPhen complex. The band-edge emission of ZnO nanowalls and excitation and phosphorescence spectra of phen are marked as BE, P* and PP, respectively. Schematic energy	

level diagrams for sensitized luminescence of ZnO nanowalls surface-functionalized by (b) EuPhen and (c) TbPhen.	85
Figure 6.5 (a) A spectroscopic representation of processes involved in the non-cascade energy transfer from ZnO to EuODA or TbODA complexes. The band-edge (BE) emission of ZnO are shown along with the excitation spectra of Eu and Tb cations. Schematic energy diagrams of sensitized luminescence of ZnO nanowalls surface-functionalized by (b) EuODA and (c) TbODA. .	86
Figure 6.6 XPS spectra of (a) C 1s and (b) N 1s regions of Phen powder, EuPhen and TbPhen complexes, and ZnO nanowalls drop-casted with EuPhen and TbPhen complexes.	89
Figure 6.7 XPS spectra of (a) C 1s and (b) O 1s of ODA powder, EuODA and TbODA complexes, and ZnO nanowalls drop-casted with EuODA and TbODA complexes.	90

List of Tables

Table 1.1 Properties of common TCOs.	2
Table 1.2 Characteristics of the emission transitions of trivalent europium and terbium cations. ⁹⁵⁻⁹⁹	15
Table 6.1 Absolute PL quantum yields (%) of LnPhen and LnODA in powder state, and as surface-functionalized ZnO nanowalls ($\lambda_{\text{exn}} = 325$ nm).	88

Chapter 1

Introduction

1.1 Transparent Conducting Oxides

Since the discovery of transparent conducting oxides (TCOs) in 1907 by Badeker,¹ they have received a lot of attention for their potential applications as active components in solar cells, light emitting diodes and photodetectors. This was mainly because of high optical transparency in the visible range of the electromagnetic spectrum and relatively low electrical resistivity ($<10^{-3} \Omega\cdot\text{cm}$) upon appropriate modification of TCOs by introducing impurities or defects.² The low electrical resistivity is caused by the electrons from extrinsic dopants or intrinsic defects which occupy the conduction band of TCOs and yield the high carrier concentration. Furthermore, since the electrons from defects and dopants already populate the lowest unoccupied energy levels in the conduction band, electrons in the valence band are excited to the higher energy level in unoccupied conduction band levels than the lowest unoccupied conduction band and resulted in placing the higher conduction band minimum in energy than pristine TCOs.^{3,4} The resulting blue-shift of the conduction band minimum is called the Moss-Burnstein shift and leads to widening the energy band gap of modified TCOs. TCOs are primarily binary or ternary oxide materials often synthesized with various dopants and the properties of some common TCOs with their dopant configurations are summarized in Table 1.1.

Due to the toxicity of cadmium, present as the main component in the first discovered TCO materials (CdO, CdS and CdSe), intense effort has been made to uncover other more environmentally safe semiconducting TCO materials such as indium oxide, tin oxide and zinc oxide.¹ One of the most popular doped indium oxide, tin-doped indium oxide or commonly known as indium tin oxide (ITO) was developed while investigating heat problems of sodium lamps by Groth et al.^{5,6} Tin, zinc, titanium, fluorine and molybdenum have been used as dopants and the resulting doped TCO materials demonstrate good optical (80~85% transmittance) and electrical properties (with low resistivity of $0.77\text{-}4.4 \times 10^{-4} \Omega\cdot\text{cm}$).⁷⁻¹² For tin oxide, fluorine was used as one of the most common dopants to give fluorine-doped tin oxide (FTO). By depositing FTO on an ITO substrate, the resulting FTO/ITO hybrid architecture showed even better electrical and photovoltaic properties than ITO.¹³ In the case of zinc oxide, several elements such as aluminum, gallium, zirconium, boron and titanium were used as dopants and the electrical and optical properties of both aluminum-doped and gallium-doped zinc oxides appear to be similar to those of ITO, as shown in Table 1.1.¹⁴⁻²⁰

Among these doped TCOs, ITO has been one of the most widely used materials for a wide range of applications. However, according to United States Geological Survey, the cost of indium metal remains very high, at US\$570/kg in 2013 and estimated US\$695/kg in 2014.²¹ For FTO, the chemicals used for fluorine doping such as hydrofluoric acid, carbon tetrafluoride and ammonium fluoride have high toxicity and significant adverse environmental impact. Furthermore, although FTO has major low-cost advantage over ITO, ITO outperforms FTO in electrical and optical applications. On the other hand, zinc oxide is considerably less costly (at US\$1.5/kg, based on the cost of zinc metal in 201) and about 10 times less expensive than metallic tin*. It is also non-toxic, and there is an affluent abundance (~1.9 billion tons) worldwide. Since zinc oxide has similar electrical and optical properties as pristine indium oxide and tin oxide (Table 1.1), the aforementioned additional advantages have made ZnO a low-cost, environment-friendly alternative to ITO and FTO and is therefore the focus of the present work.^{21,22}

Table 1.1 Properties of common TCOs.

Materials	Dopant	Resistivity ($10^{-3} \Omega \cdot \text{cm}$)	Transmittance (%)	Energy bandgap (eV)
Indium Oxide	None ^{23,24}	0.85-6.7	80	3.75
	Sn ^{11,12} (ITO)	0.077-0.129	>85	3.64
	Zn ⁸	0.24	80	3.88
	Ti ¹⁰	0.411	>83	3.4~3.8
	F ⁷	0.44	>80	3.72
	Mo ⁹	0.17	>80	4
Tin Oxide	None ^{24,25}	3.57	~80	3.6
	F ²⁶ (FTO)	0.22-0.47	85	4.11
	Sb ²⁷	0.9	70~85	4.13-4.22
Zinc Oxide	None ^{24,28}	1.7	~90	3.15-3.37
	Zr ¹⁸	2.07	~90	3.28-3.35
	B ¹⁹	0.79	~88	3.24~3.35
	Ti ²⁰	9.02	>85	3.33
	Al ^{14,16}	0.0854-0.191	75-90	3.51-3.86
	Ga ^{15,17}	0.0812-0.53	~90	3.37-3.51

* Based on the official price of metallic tin and zinc traded at the London metal exchange in the fourth week of September, 2015.

1.2 Zinc Oxide

1.2.1 Properties of Zinc Oxide

Zinc oxide is a IIb-VI binary compound and it shows three different crystal structures (shown in Figure 1.1): rocksalt, zinc blende and hexagonal wurtzite. The most stable structure is hexagonal wurtzite, while zinc blende and rocksalt structures can be observed only under certain conditions, such as high pressure or epitaxial growth on a cubic structured substrate.²⁹ As shown in Figure 1.1, the hexagonal wurtzite structure of ZnO consists of tetrahedrally coordinated oxygen and zinc atoms with lattice parameters $a = b = 3.2498$ and $c = 5.2066$ Å, and sp^3 ionic bonding between a Zn^{2+} cation and an O^{2-} anion. ZnO shows direct transition between the conduction band and valence band with an energy band gap of 3.37 eV at 300 K.

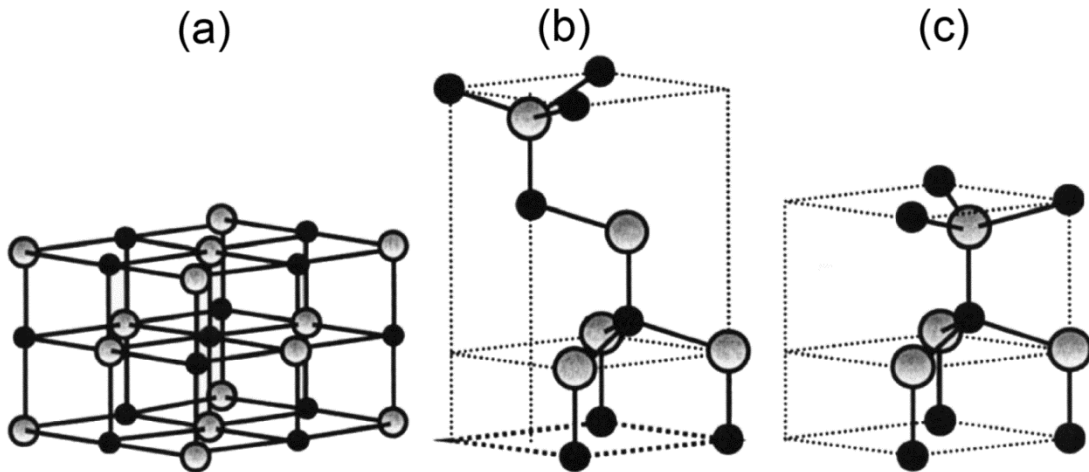


Figure 1.1 Stick-and-ball representation of ZnO crystal structures: (a) cubic rocksalt, (b) cubic zinc blende, and (c) hexagonal wurtzite. The shaded gray and black spheres denote Zn and O atoms, respectively.[†]

It has been found that almost all of the ZnO nanostructured materials are n-type and they have high electrical conductivity. Recent studies showed that native defects, specifically zinc and oxygen vacancies, have relatively low formation energies than other defects such as zinc and oxygen interstitials.³⁰ Depending on the conditions, oxygen vacancies can act as electron donor sites by

[†] Reprinted with permission from Özgür, Ü.; Alivov, Y. I.; Liu, C.; Teke, A.; Reshchikov, M. A.; Doğan, S.; Avrutin, V.; Cho, S. J.; Morkoç, H.; Morkoç, H. A Comprehensive Review of ZnO Materials and Devices. *J. Appl. Phys.* **2005**, 98 (4), 1–103. Copyright 2005, AIP Publishing LLC.

releasing trapped electrons, thereby causing high conductivity and n-type semiconducting behavior. These defects also have strong influence on the optical properties, especially luminescence emission of ZnO. Figure 1.2 shows typical photoluminescence spectra of as-grown and thermally treated ZnO nanorods.³¹ A deep ultraviolet (UV) emission generated by the large energy band gap and several visible emissions were observed upon excitation by 325 nm light. Visible emissions could be caused by defects such as interstitials and Zn and O vacancies. A green emission was found even after thermal annealing and this was attributed to formation of defect complexes related to Zn vacancies.³¹ The energy level diagrams of ZnO with different types of defects that could give rise to various visible-range emissions are shown in Figure 1.3.

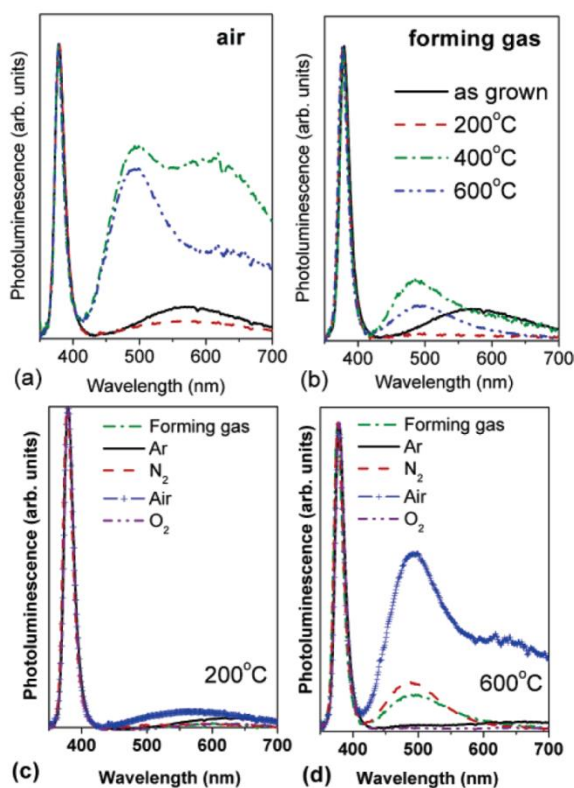


Figure 1.2 Room-temperature photoluminescence spectra of as-grown ZnO nanorods and ZnO nanorods postannealed at 200, 400 and 600 °C in (a) air and (b) forming gas (90% N₂/10% H₂), and of ZnO nanorods annealed in different atmospheres at (c) 200 °C and (d) 600 °C.[‡]

[‡] Reprinted with permission from Tam, K. H.; Cheung, C. K.; Leung, Y. H.; Djurisić, a B.; Ling, C. C.; Beling, C. D.; Fung, S.; Kwok, W. M.; Chan, W. K.; Phillips, D. L.; Ding, L.; Ge, W. K. Defects in ZnO Nanorods Prepared by a Hydrothermal Method. *J. Phys. Chem. B* **2006**, 110 (42), 20865–20871. Copyright 2006 American Chemical Society.

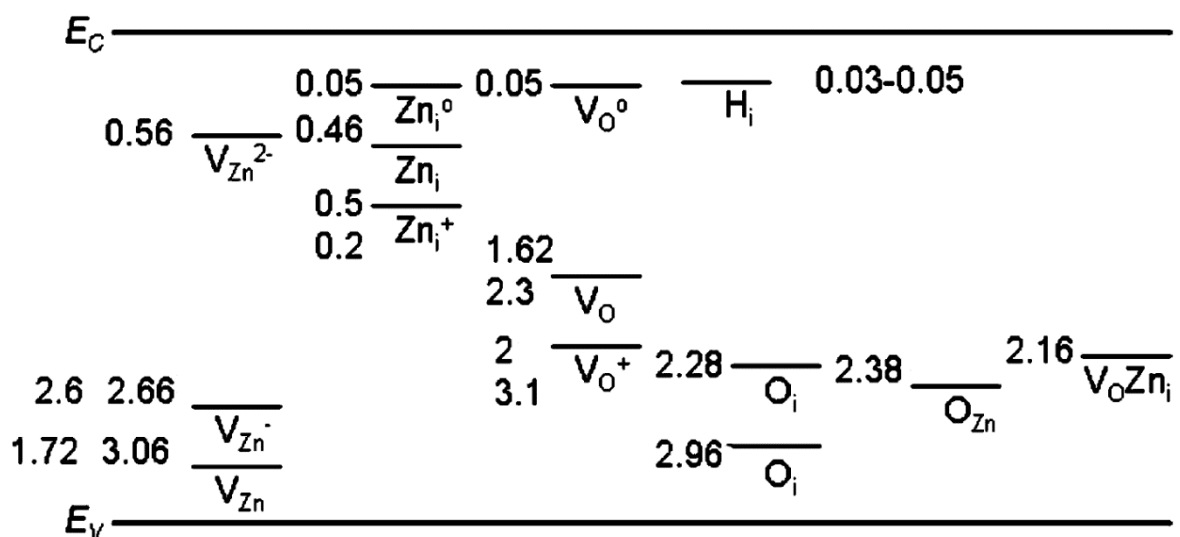


Figure 1.3 Energy levels (in eV) of different defects between the conduction band minimum (E_C) and valence band maximum (E_V) in ZnO. V_{Zn} , V_O , Zn_i , O_i and H_i denote zinc and oxygen vacancies, and zinc, oxygen and hydrogen interstitials, respectively. $V_O Zn_i$ indicates a complex of oxygen vacancy and zinc interstitial.[§]

1.2.2 Deposition Methods

ZnO has attracted great interest due to its prominent electrical and optical properties, chemical and thermal stability, as well as nontoxicity and biocompatibility. Fabrication of ZnO structures in the nanoscale regime has exploited several advantages, such as quantum confinement effect on optoelectronic and photophysical properties and enhancement of surface area to volume ratio. Various deposition methods have been developed to synthesize different types of ZnO nanostructures. Several physical vapor deposition (thermal evaporation, magnetron sputtering, and pulsed laser deposition) and chemical vapor deposition (including metal-organic chemical vapor deposition and plasma-enhanced chemical vapor deposition) as well as wet-chemistry synthesis methods (hydrothermal, solvothermal and sol-gel methods) have been employed. Among these, both physical and vapour deposition techniques have produced a wide variety of one-dimensional nanostructures, including

[§] Reprinted with permission from Tam, K. H.; Cheung, C. K.; Leung, Y. H.; Djurisić, a B.; Ling, C. C.; Beling, C. D.; Fung, S.; Kwok, W. M.; Chan, W. K.; Phillips, D. L.; Ding, L.; Ge, W. K. Defects in ZnO Nanorods Prepared by a Hydrothermal Method. *J. Phys. Chem. B* **2006**, 110 (42), 20865–20871. Copyright 2006 American Chemical Society.

nanowires and nanorods, and thin films.^{32–37} On the other hand, wet-chemistry methods have been used to produce zero-dimensional nanostructures (nanoparticles), in addition to nanowires and thin films.^{38–41} Although physical and chemical vapor deposition methods have the advantages of obtaining better-quality crystal structures and good control of morphologies, they usually require relatively high temperature and catalysts. In contrast, wet-chemistry methods generally employ relatively low temperature. However, their synthesis time could take up to several days and they are less environment-friendly due to the often need for the use of organic solvents. Unlike other wet-chemistry methods, electrochemical deposition offers several advantages, including usage of simple aqueous solutions, lower deposition temperature, shorter growth time, relative ease of scale-up, and high cost-effectiveness for commercialization. In addition, electrodeposition provides a greater variety of nanostructures than physical and chemical vapor deposition methods. Figure 1.4 shows examples of several morphologies of one- and two-dimensional ZnO nanostructures obtained by electrochemical deposition.^{42,43}

1.2.3 Applications

Since ZnO has a wide direct band gap of 3.37 eV and produces near band-edge emission in the UV to blue region, optoelectronic devices such as UV/blue-range light emitters and photodetectors represent two of the most popular applications of ZnO nanostructures. UV light emitting diodes (LEDs) and UV detectors with detection range of 325–375 nm have been fabricated based on various ZnO nanostructures including nanowires, quantum dots and nanorods, and their performance was found to be comparable to GaN-based devices.^{44–48} Alvi et al. have also constructed LEDs using other ZnO nanostructures including nanowalls, nanoflowers, and nanotubes.⁴⁹ In addition to the wide direct band gap, the high exciton binding energy (60 meV) of ZnO protects excitons from thermal dissociation, which enables the construction of ZnO-based dye-sensitized solar cells. Ko et al. have demonstrated the good performance of ZnO based solar cells by employing quasi-one-dimensional ZnO nanostructures such as nanotrees (Figure 1.5), the conversion efficiency of which could be improved by more than two times.^{50,51} ZnO has also been employed as photocatalysts in photoelectrochemical water-splitting and degradation of organic materials. By implementing hybrid structures with gallium nitride, stable water-splitting reaction using visible light was achieved.⁵² Photodegradation ability of organic pollutants by ZnO-based materials were also reported and showed higher photodegeneration rate than titanium oxide.^{53–55} The present work explores the potential use of ZnO quantum sheets and nanowalls for optical and optoelectronic applications.

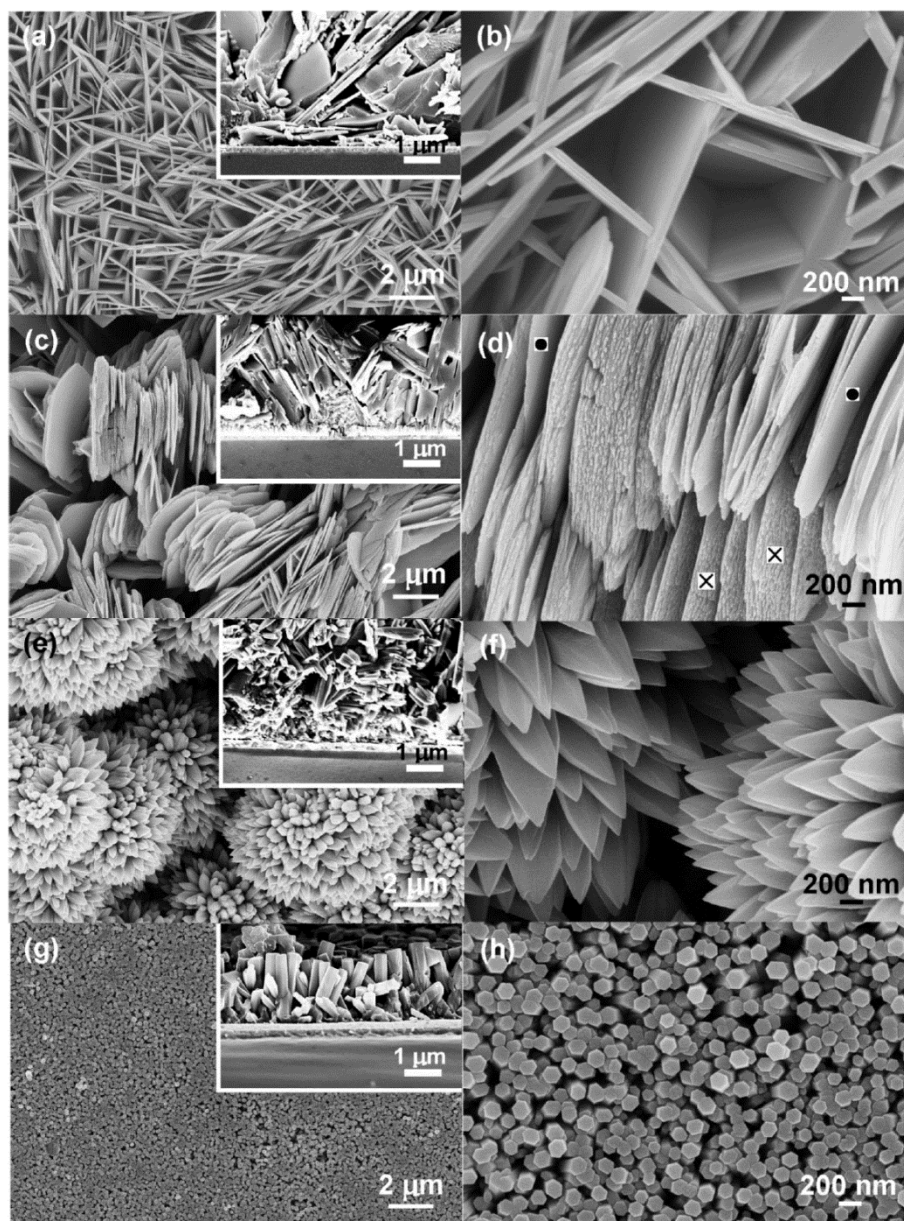


Figure 1.4 Scanning electron micrographs of (a, b) ZnO nanowalls, (c, d) nanodisks, (e, f) nanopikes, and (g, h) nanopillars electrochemically grown on ITO-glass at 70 °C with 0.1 M KCl solution and varying $\text{Zn}(\text{NO}_3)_2 \cdot 6\text{H}_2\text{O}$ concentrations of 0.1, 0.05, 0.01, and 0.001 M, respectively. Insets show the corresponding cross sectional images.**

** Reprinted with permission from Pradhan, D.; Leung, K. T. Controlled Growth of Two-Dimensional and One-Dimensional ZnO Nanostructures on Indium Tin Oxide Coated Glass by Direct Electrodeposition. *Langmuir* **2008**, 24 (17), 9707–9716. Copyright 2008 American Chemical Society.

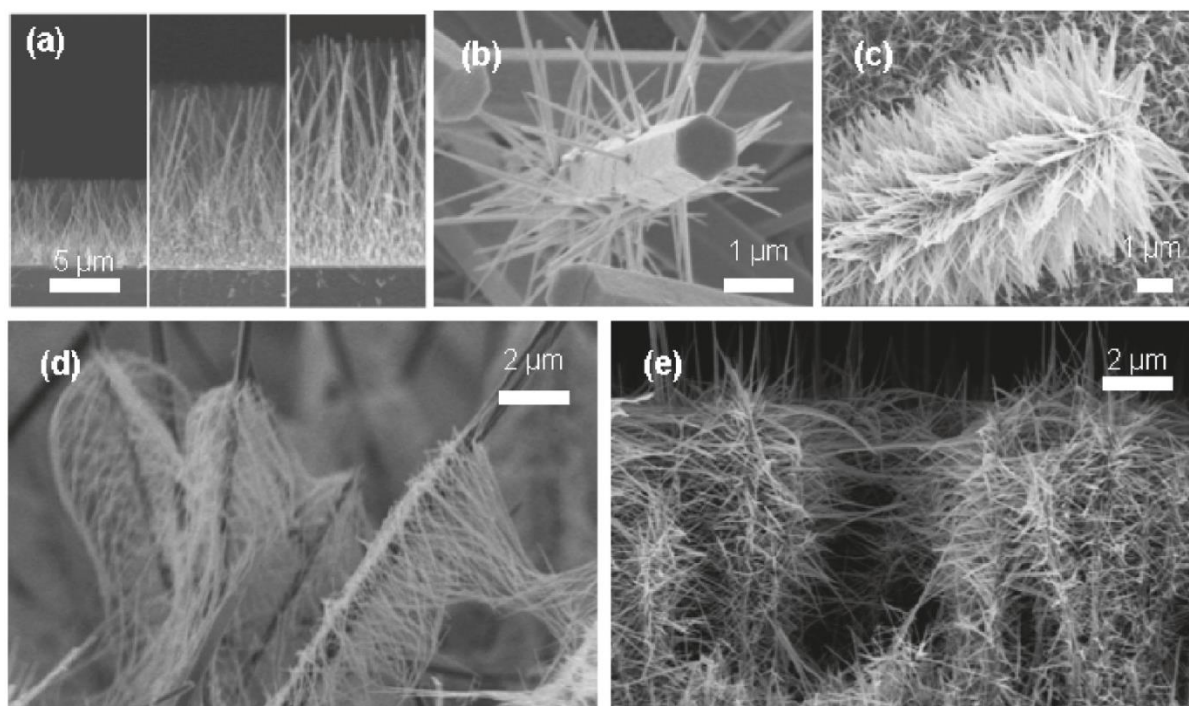


Figure 1.5 Scanning electron micrographs of hydrothermally grown ZnO nanowires illustrating (a) length growth (to 1, 2, and 3 times of the original length), and seed effect with first-generation branched growth (b) without and (c) with seeds after polymer removal. Polyethylenimine removal effect is shown with first-generation branched growth (d) without and (e) with polymer removal after nanoparticle seed deposition. Polymers on ZnO nanowires are removed by heating at 350 °C for 10 min.^{††}

ZnO nanostructures have also been extensively studied for chemical and gas sensing applications because of its high specific surface areas, favorable electron conductivity, and excellent chemical and thermal stability. Once the target materials are adsorbed on the ZnO nanostructure surface, the concentration of electrons on the conduction band of ZnO could be affected by accepting or donating electrons and the resulting changes of conductivity can be quantified. Fan et al. fabricated oxygen sensing devices based on single-crystalline ZnO nanowires and showed significantly enhanced sensitivity compared to bulk or thin-film based sensors at room temperature.⁵⁶ Other chemicals such

^{††} Reprinted with permission from Ko, S. H.; Lee, D.; Kang, H. W.; Nam, K. H.; Yeo, J. Y.; Hong, S. J.; Grigoropoulos, C. P.; Sung, H. J. Nanoforest of Hydrothermally Grown Hierarchical ZnO Nanowires for a High Efficiency Dye-Sensitized Solar Cell. *Nano Lett.* **2011**, *11* (2), 666–671. Copyright 2011 American Chemical Society.

as hydrogen sulfide, ethanol, chlorobenzene, carbon monoxide, ammonia and hydrogen gas were tested with several different ZnO nanostructures (nanorods, nanoplates and nanoparticles) and showed wide detection range and fast response time for hydrogen.⁵⁷⁻⁵⁹

Good biocompatibility with a high isoelectric point (8.7~10.3) is also a key factor for ZnO-based biosensor applications because materials with a high isoelectric point could facilitate adsorption of biomolecules with a lower isoelectric point by electrostatic interactions.⁶⁰ By functionalizing ZnO nanostructures with enzymes capable of reduction-oxidation reactions, enzyme-based electrochemical biosensors can be developed. A glucose biosensor based on ZnO nanotubes functionalized with glucose oxidase has been found to perform over a wide detection range and with a fast response time.⁶¹ Several biosensors using chitosan to functionalize ZnO nanoparticles with cholesterol oxidase, flower-like ZnO nanostructures with horseradish peroxidase, and ZnO nanoparticles with tyrosinase were fabricated to detect hydrogen peroxide, cholesterol and phenol, respectively.⁶²⁻⁶⁴ Cholesterol oxidase in ZnO/chitosan composite materials achieved a lifetime of 85 days, and both the H₂O₂ detection capability and storage stability were improved.^{62,63} Li et al. developed a phenol biosensor using ZnO and tyrosinase and showed enhanced stability and lower detection limit than TiO₂ or Au/C based biosensors.⁶⁴

1.3 Properties of Rare-Earth Transition Metals and Its Applications

1.3.1 Luminescence Properties of Rare-Earth Transition Metal Materials

Rare-earth (RE) transition metals include 15 lanthanoids (⁵⁷La to ⁷¹Lu), scandium (²¹Sc), and yttrium (³⁹Y).⁶⁵ In 1906, the observation of luminescence emission of Eu from Eu-doped Y₂O₃ triggered significant research activities in the field of lanthanoid luminescence. The discovery of Nd emission from Nd-doped yttrium aluminum garnet laser and of optical signal enhancement using Er-doped optical fiber cable became the cornerstones for optical and optoelectronic applications of RE materials.⁶⁶⁻⁶⁸

Lanthanoids form trivalent cations in nature and their electron configurations can be defined by numerical order of the 4f^N (N = 0 – 14) orbital. Except for lanthanum (La, Z=57) and lutetium (Lu, Z=71), which have completely empty and full 4f shells respectively, their 4f electron configurations yield optical emission ranging from the UV to near-infrared regions, upon excitation by UV radiation. The electron energy level diagrams, electron configurations and luminescent properties for trivalent lanthanoid cations are summarized in Figure 1.6.⁶⁹ The excitation spectra of the lanthanoid

luminescence generated by crystalline structures or aqueous solutions of RE materials showed that these emissions are based on the $f \leftrightarrow f$ transitions involving the 4f orbitals. However, the selection rule dictates that an electronic transition between energy levels with the same parity is forbidden. In a free lanthanoid atom, for the same total angular momentum quantum number (J), states with different spin (S) and orbital angular momenta (L) can be mixed by spin-orbit interaction, thus coupling S and L to form new energy states called the intermediate coupling states. The selection rules for the intermediate coupling states allow electric dipole transition when the differences of the spin quantum numbers (S) for the initial and final states is $\Delta S = \pm 1$ and of the orbital angular momentum quantum numbers is $\Delta L = 0, \pm 1$ and ± 2 . Nevertheless, electric dipole transition could still be forbidden for transitions between levels with the same parity.

Since the $f \leftrightarrow f$ transition caused by electric dipole interactions is theoretically forbidden, magnetic dipole and/or electric quadrupole interactions are considered.^{70,71} However, not all transitions could be accounted for by involving just magnetic dipole interactions.⁷² By employing electric quadrupole interactions, it is possible to identify all the transitions despite accurate estimate of the spectral intensities has remained a big challenge.⁷¹ A plausible solution involving electric dipole interactions induced by crystal-field potential was therefore developed. This novel approach has attracted great interest.⁷³ In 1962, Judd and Ofelt independently reported theoretical developments for what is known as the Judd-Ofelt Theory.^{74,75}

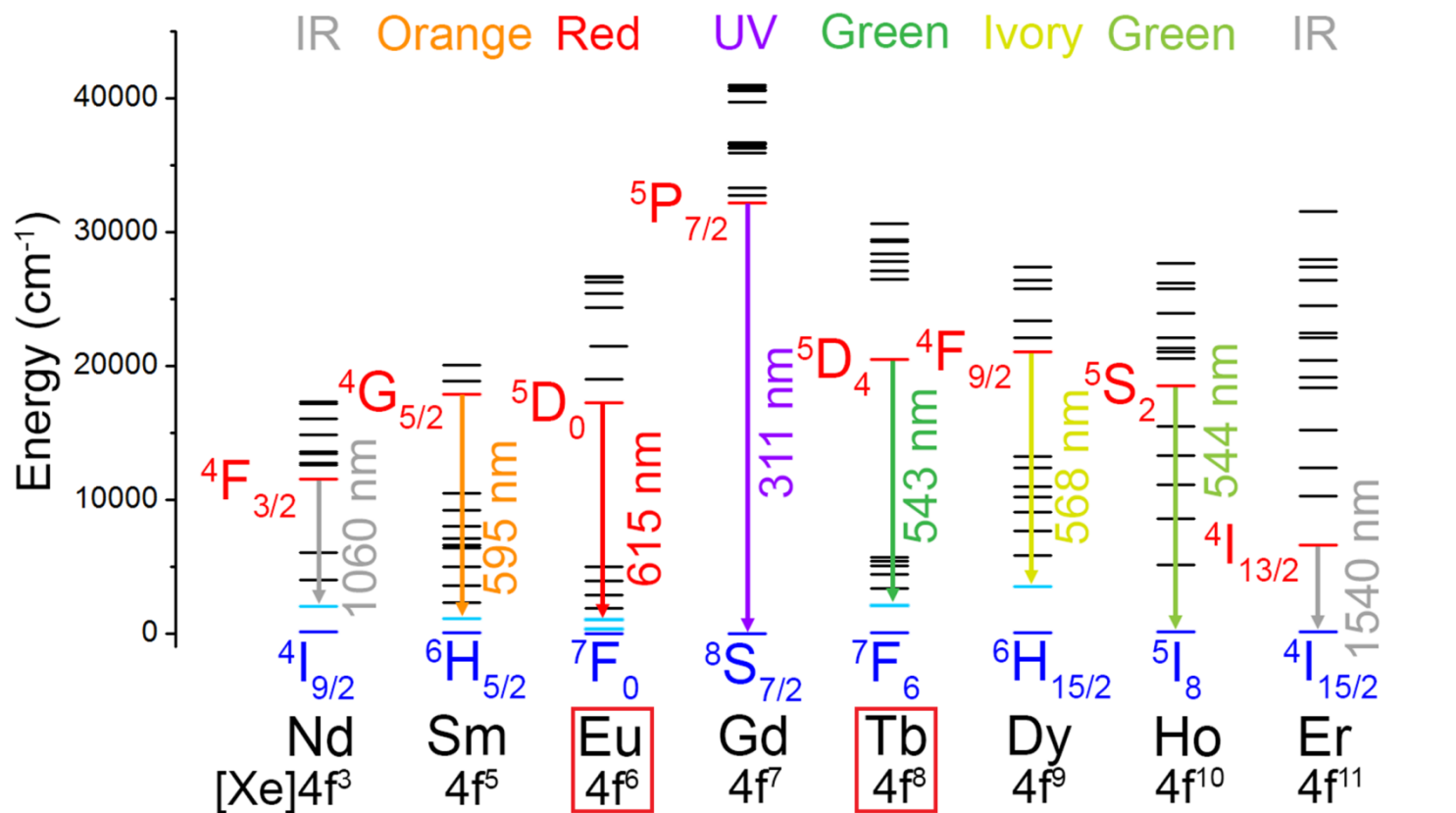


Figure 1.6 Partial energy level diagrams for the lanthanide aquo ions. The main excited-state energy levels are drawn in red while the (lower-state) final levels and ground-state energy levels are indicated in pale blue and navy blue, respectively.^{76–80} The Eu and Tb diagrams are highlighted for future references to our studies presented in Chapters 4, 5 and 6.

1.3.2 Judd-Ofelt Theory

The intensity of emission generated by the electric dipole interaction, P_{ED} , can be defined as follows:⁷⁴

$$P_{ED} = \chi \left(\frac{8\pi^2 mc\bar{\nu}}{h} \right) \left| \langle G | \mathbf{D}_q^{(1)} | E \rangle \right|^2 \quad (1.1)$$

where m = mass of electron, h = Planck's constant, c = speed of light, $\bar{\nu}$ = wavenumber of the transition energy (cm^{-1}), χ = Lorenz local field correction constant and $\mathbf{D}_q^{(1)}$ is an electric dipole operator (tensor operator of rank 1). Considering only the 4f orbitals, the ground-state wavefunction $|G\rangle$ and excited-state wavefunction $|E\rangle$ can be expressed as $|f^n; \alpha SLJ\rangle$ and $|f^n; \alpha' S' L' J'\rangle$, respectively, where f indicates 4f orbital, n is the number of electrons in the 4f orbital and α corresponds to quantum numbers other than S , L and J . The strong spin-orbit interaction in the lanthanoid elements leads to linear combination of LS-coupled states that give rise to the intermediate coupling states. Equation (1.1) can be rewritten as:

$$P_{ED} = \chi \left(\frac{8\pi^2 mc\bar{\nu}}{h} \right) \left| \langle \psi_a^0 | P | \psi_b^0 \rangle \right|^2 \quad (1.2)$$

where P is an electric dipole operator, ψ_a^0 is the ground-state wavefunction $|f^n; \alpha [SL]J\rangle$ and ψ_b^0 is the excited-state wavefunction $|f^n; \alpha' [S'L']J'\rangle$ (in which the square brackets for $[SL]$ refer to the coupled states). However, the $f \leftrightarrow f$ transition remains forbidden because the excited state and the ground state have the same parity.

In order to circumvent this problem, Judd and Ofelt assumed perturbation of orbitals with different parities induced by the crystal-field potential.^{74,75} The crystal field theory was introduced by Bethe and Van Vleck, and the crystal field potential was generated by the attractive and repulsive interactions of a lanthanoid cation with the neighboring atoms of a host crystal and/or with the attaching organic ligand molecules.^{81,82} The crystal field of a non-central symmetric crystal structure causes perturbation to the electronic states with different parities. Since the 4f orbital has an odd parity, mixing it with an even-parity orbital (5d) would produce mixed-parity states that would allow electric dipole transitions. Incorporating parity perturbation by the crystal-field potential to the Equation 1.2 yields:

$$P_{ED} = \chi \left(\frac{8\pi^2 mc\bar{\nu}}{h} \right) \left| \langle \psi_a | P | \psi_b \rangle \right|^2 \quad (1.3)$$

where

$$|\psi_a\rangle = |\psi_a^0\rangle + \sum_{\beta} \frac{\langle \psi_a^0 | V_{CF} | \psi_{\beta} \rangle}{E_a - E_{\beta}} |\psi_{\beta}\rangle \quad (1.4)$$

$$|\psi_b\rangle = |\psi_b^0\rangle + \sum_{\beta} \frac{\langle \psi_b^0 | V_{CF} | \psi_{\beta} \rangle}{E_b - E_{\beta}} |\psi_{\beta}\rangle \quad (1.5)$$

$|\psi_{\beta}\rangle$ is the wavefunction for the mixed-parity state and V_{CF} is the crystal field potential operator.^{74,75,83,84} To simplify the equations, several mathematical techniques involving the Wigner-Eckart theorem, the 3-j symbol and the 6-j symbol were implemented and more details were given in Refs. 74-80. The final equation proposed by Judd and Ofelt to account for the intensity of the electric dipole transition is given as:^{73-75,84}

$$P_{ED} = \chi \left(\frac{8\pi^2 mc \bar{\nu}}{h} \right) (2J + 1)^{-1} \sum_{\lambda=2,4,6} \Omega_{\lambda} \langle \psi_a^0 \| U^{(\lambda)} \| \psi_b^0 \rangle^2$$

where the reduced tensor unit resulted from the Wigner-Eckart theorem, $U^{(\lambda)}$, is determined by the electron energy level and orbital wavefunctions and it has minimal influence on the emission intensity. The intensity parameter Ω_{λ} consists of the mixing effect of the f and d orbitals, and it is derived from the electric dipole moment and the crystal field. It is also directly related to the emission intensity and its value can be determined by optimization of experimental results.^{73-75,84}

Fundamentally, the intensity of emission produced by the f \leftrightarrow f transition is not affected by the nature of coordination and chemical bonding because electrons in the 4f orbitals of a lanthanoid cation are well protected by 5s and 5p orbitals. However, while existing as a free cation in an aqueous solution, some transitions have showed significant intensity enhancement of tens or hundreds times due to subtle changes in the chemical environment.^{85,86} These transitions are known as hypersensitive transitions.⁸⁷ Since the standard Judd-Ofelt theory was not able to account for the large intensity increase of hypersensitive transitions, an additional mechanism, originally known as inhomogeneous-dielectric mechanism and later as dynamic coupling, was introduced. In the standard Judd-Ofelt theory, the nature of chemical bonding and crystal structures of lanthanoid cations had been treated as a source of parity perturbation by introducing the crystal field potential and the lanthanoid cations were considered as free ions.^{73,74} The dynamic coupling mechanism proposed that the environment of lanthanoid cations, specifically the elements belonging to the ligand molecules and/or the host lattice could directly interact with the lanthanoid cations and could also perturb the wavefunctions of the

lanthanoid cations and thereby enhance the amplitude of transition. These enhancements produced the remarkable increases observed in the intensities of the hypersensitive transitions.^{73,87-89}

Another supplemental improvement to the standard Judd-Ofelt theory was J-mixing, which was used to explain a few forbidden electronic transitions. In the J-mixing formalism, the role of the crystal-field potential was expanded further and the potential was used to induce combination of wavefunctions of different J states into those of nearby J states with the same azimuthal total angular quantum number (M_J).⁹⁰⁻⁹² In certain crystal structures, the emission from the forbidden transitions, such as the $^5D_0 \leftrightarrow ^7F_0$ transition in trivalent europium cations, has been observed.^{90,92} In this case, depending on the site-symmetry of trivalent europium cation, mixing between $M_J=0$ states of the 7F_0 and 7F_2 states by the crystal-field potential has enabled this forbidden transitions.⁹⁰

1.3.3 Characteristics of Europium and Terbium Emissions

The emissions from the trivalent lanthanoid cations are generally found to occur in the UV to near-IR range. Among them, europium and terbium have received the most attention because of the strong emission intensities, the hypersensitive emissions and the long lifetimes found for the observed emissions.⁹³ Since electrons in the 4f orbitals are well shielded by the 5s and 5p orbitals, the environment of lanthanoid cations should have minimal influence on the position of the emission (originating from the 4f orbitals). However, the occurrence of transitions and their spectral intensities are found to depend on the host crystal structure and chemical bonding nature of surrounding environment.

In the case of trivalent europium complexes, most of the emissions are originated from the 5D_0 excited state (Figure 1.6).⁹⁴ The emission intensities of $^5D_0 \rightarrow ^7F_1$ and $^5D_0 \rightarrow ^7F_2$ are dramatically higher. The higher intensity for the latter emission is due to the hypersensitive transition of 7F_2 triggered by the nature of the complexes.⁹³ For the $^5D_0 \rightarrow ^7F_1$ transition, it is magnetic dipole allowed and is generally less affected by the surrounding environment than the electric dipole transition $^5D_0 \rightarrow ^7F_2$ transition.^{84,95}

For the trivalent terbium complexes, the 5D_4 energy level becomes the primary excited level of the transitions (Figure 1.6).⁹⁴ The $^5D_4 \rightarrow ^7F_5$ transition shows the strongest and hypersensitive emission intensity among the observed transitions.⁹⁶ The intensities for the $^5D_4 \rightarrow ^7F_6$, $^5D_4 \rightarrow ^7F_4$ and $^5D_4 \rightarrow ^7F_2$ emission transitions are moderately affected by the chemical environment and coordination nature of

the complexes.⁹⁵ Details of the relevant trivalent europium and terbium emissions are summarized in Table 1.2.

Table 1.2 Characteristics of the emission transitions of trivalent europium and terbium cations.⁹⁴⁻⁹⁸

Excited State	Final State	Wavelength (nm)	Emission Intensity
Europium ⁵ D ₀	⁷ F ₀	580	Weak
	⁷ F ₁	590	Strong
	⁷ F ₂	615	Strong, Hypersensitive
	⁷ F ₃	645	Weak
	⁷ F ₄	700	Medium
Terbium ⁵ D ₄	⁷ F ₆	490	Medium
	⁷ F ₅	545	Strong, Hypersensitive
	⁷ F ₄	585	Medium
	⁷ F ₃	520	Medium
	⁷ F ₂	650	Weak

1.3.4 Energy Transfer and Sensitization Mechanism

Although lanthanoid luminescence has unique characteristics, such as hypersensitive transitions that are sensitive to the surrounding environment and well-defined multiple emission bands, the luminescence yield are usually very small in comparison to the organic based fluorophores.⁹³ Because the $f \leftrightarrow f$ transition could occur due to the induced electric dipole moment generated by the crystal field perturbation of the electronic states, the absorption coefficients of the transitions are very small, which lead to weak emissions. However, the solution to this problem appeared to be uncovered, when Weissman observed characteristic europium emission from trivalent europium organic complexes. Upon irradiation of the europium complexes using excitation wavelength of the ligand, the complex produced intense luminescence.⁹⁹ Since the absorption bands of the ligand have a wider range and higher intensity than those of the trivalent lanthanoid cations, the ligand is able to absorb more energy. Under certain conditions, the absorbed energy by the ligand could be transferred to the lanthanoid cations, which then generate stronger emission than that caused by direct excitation of the cations. This phenomenon is known as sensitization by energy transfer from the ligand donor to the lanthanoid cation acceptor.^{93,94,97} A schematic diagram of the sensitization and energy-transfer process is shown in Figure 1.7.

The energy transfer process starts with the excitation of the organic ligands (the donor) of the lanthanoid complexes. Upon excitation ($S_0 \rightarrow S_1$) of the donor to the excited singlet state (S_1), the organic ligand undergoes vibrational relaxation and proceeds to the lowest vibronic level of S_1 .¹⁰⁰ Two competitive de-excitation processes involving radiative and nonradiative transitions could occur. The radiative, fluorescence process is generated by $S_1 \rightarrow S_0$ emission of the ligands. The nonradiative process involves an intersystem crossing (ISC) transition from the singlet S_1 state to the triplet T_1 state.¹⁰¹ After the ISC process, if the donor then undergoes a radiative relaxation, the emission is called phosphorescence. Since the $T_1 \rightarrow S_0$ transition is spin-forbidden by the Pauli exclusion principle, the intensity of the phosphorescence is significantly lower than fluorescence and its lifetime is longer than fluorescence.¹⁰¹ Alternatively, a nonradiative energy transfer transition from T_1 to the excited states of lanthanoid cations (an acceptor) can take place.¹⁰¹ The excited acceptor state then undergoes nonradiative relaxation to the resonance level of lanthanoids, which subsequently leads to the characteristic lanthanoid emissions to the ground level.

The efficiency of the energy transfer in lanthanoid complexes depends on the separation between the ligand and the lanthanoid ions. Taking the phase and bonding nature of the complex under consideration, the Dexter theory has incorporated the concept of the energy transfer mechanism occurring in the lanthanoid complexes.¹⁰² In the Dexter theory, the energy transfer mechanism is based on the exchange of electrons between the ligand and the lanthanoid cation via overlapping orbital wavefunctions, and the energy transfer rate depends exponentially on the separation between the ligands and the lanthanoid cations.^{100,102} Figure 1.8 shows a simplified schematic diagram of the energy transfer mechanism between the ligand (L) and the metal cation (M). Once the ligand of the lanthanoid complex is excited (Figure 1.8b), the lanthanoid cation receives energy by exchange of electrons between an electron in the excited state of the ligand molecule and an electron in the ground state of the lanthanoid cation (Figure 1.8c). Since there is chemical bonding between the ligand and the lanthanoid cation in most complexes, the separation is sufficiently short that such energy transfer could occur. The Dexter theory could therefore be used to easily account for the emission features found in lanthanoid complexes.

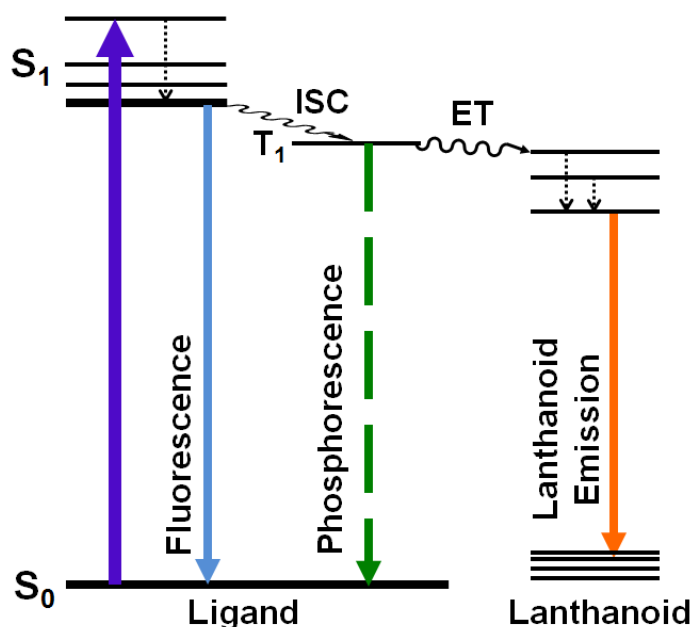


Figure 1.7 Schematic diagram of sensitization of lanthanoid complexes. Nonradiative transition and nonradiative relaxation are represented by zigzag and dotted lines, respectively. The ligand must undergo intersystem crossing (ISC) between the S_1 and T_1 states in order to enable the energy transfer (ET) between the ligand and the lanthanoid. The latter step leads to the observed characteristic lanthanoid emission.

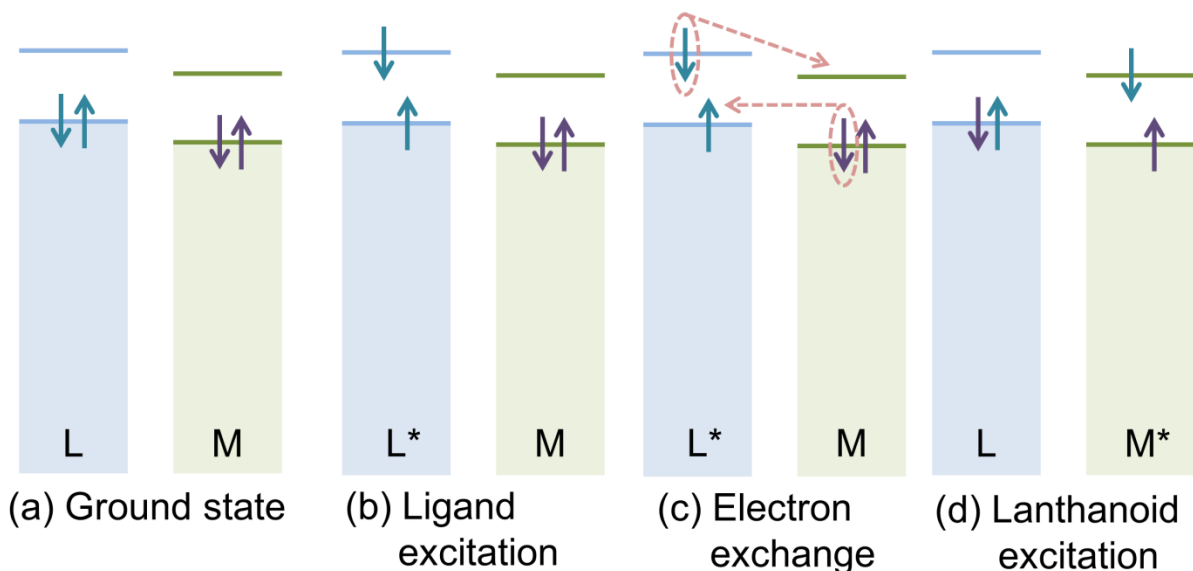


Figure 1.8 A schematic diagram of Dexter energy transfer mechanism between the ligand (L) and the metal cation (M).

1.3.5 Application of Rare-Earth Transition Metals and Its Complexes

Due to the unique luminescence properties, lanthanoid based materials have been widely studied to explore their optical and optoelectronic applications. The first fluorophore based on europium-doped yttrium orthovanadate is still in use for cathode-ray tubes and fluorescent lamps.¹⁰³ Yttrium orthovanadate with neodymium as a dopant showed near-infrared laser emission (809 nm).¹⁰⁴ Several kinds of complexes based on single and multiple lanthanoid elements, including europium, terbium, samarium, dysprosium and cerium, incorporated with conducting polymers were synthesized and used as active components for a monochromatic LED and a white LED, respectively.^{105–112} Other lanthanoids such as erbium and neodymium were used as dopants for fabricating plastic optical fiber cables in order to intensify optical signals for telecommunication with their near-infrared emission.¹¹³

Due to their large spin-orbit coupling and induced crystal-field potential from the ligands, lanthanoids and their complexes had strong magnetic properties, which enables them to be used for related applications.¹¹⁴ For example, gadolinium and its complexes are one of the favorite materials for use as an imaging contrast enhancer for magnetic resonance imaging technology.¹¹⁵ Single molecular spintronic devices based on gadolinium and dysprosium were also tested and showed promising performance.^{116,117} Other lanthanoids used as a dopant also exhibited room-temperature ferromagnetism with a magnetic field of 0.2 Telsa.¹¹⁸

1.4 Scope of the Present Work

Zinc oxide is one of the most important TCO semiconducting materials and it has attracted great interests because of its optical and optoelectronic properties. In order to modify its energy band gap and luminescence properties, the use of a dopant introduced into the ZnO host material has been widely studied.^{119–130} Various studies on doping several 3d transition elements, such as copper, nickel, and cobalt, showed minimal changes in the energy band gap and only produced stronger defect-related emissions of ZnO.^{119–122} Among the lanthanoid elements, europium is a preferred dopant because of its hypersensitive transition and strong characteristic red emission. However, the mechanism of energy transfer from ZnO to trivalent europium cations remains unclear.^{123–126} In the case of terbium doping, only a few studies have successfully generated characteristic terbium emissions from terbium-doped ZnO.^{127–130} Other elements that produce visible emission upon excitation, such as cerium, dysprosium and samarium, have also been used as dopants, and they showed very weak to none of lanthanoid characteristic transitions.^{131–135}

As nanostructured materials are expected to have different properties than their bulk state because of quantum confinement (or nanoscale size) effect, the optical, optoelectronic and photophysical properties of ZnO low-dimensional nanostructures, especially quantum dots (0-D) and nanowires (1-D), have been extensively investigated.¹³⁶⁻¹⁴⁰ However, only minimal energy widening in the band gap was observed, and both the details of electronic energy levels and luminescence properties under the influence of quantum confinement effect remain unknown.

In this work, we focus on exploiting the optical and optoelectronic properties of ultra-thin two-dimensional ZnO nanostructured materials, particularly ZnO nanosheets and nanowalls, doped or surface-functionalized with appropriate lanthanoid elements or complexes. In Chapter 1, a general introduction to the properties of ZnO and theoretical background of characteristic luminescence of lanthanoid elements are given (above). Details about the synthesis of ZnO nanostructures and brief introduction to the principles of characterization techniques used in the present work are described in Chapter 2. Chapters 3 to 6 present respective studies on pristine ZnO nanostructures, trivalent europium and terbium doped ZnO nanowalls, and surface-functionalized ZnO nanowalls by europium and terbium complexes. A summary of the present work is given in Chapter 7.

In Chapter 3, a single-unit-cell thick ZnO quantum sheet (2-D nanostructure) is prepared on a Si substrate and its optoelectronic and photophysical properties are explored. Quantum confinement effect caused by the single-unit-cell thickness results in significant widening of energy band gap and interesting changes in the fluorescence spectra. Influence of quantum confinement effect on the electronic band structure is also investigated.

Among the two dimensional nanostructures, ZnO nanowalls are selected due to their high loading capability for dopants or organic chelating agents and their high surface to volume ratio. ZnO nanowalls doped with europium (Chapter 4) and terbium (Chapter 5) are fabricated on ITO-coated glass substrates, and the energy-transfer mechanism and photophysical properties are studied. In case of europium doping (Chapter 4), the energy-transfer pathway from ZnO to trivalent europium cations is examined and the results lead us to propose a new energy-transfer mechanism involving cascade energy transfer from ZnO to trivalent europium cation via 1,10-phenanthroline. For terbium-doped ZnO nanowalls (Chapter 5), characteristic terbium emission is observed, remarkably without any post-growth treatment for the first time. Furthermore, the plasmonic effect of noble metal nanoparticles on the terbium-doped ZnO nanowalls has been investigated by examining the spectral

intensity of photoluminescence. The possibility of terbium emission for chemosensing application is also explored.

In Chapter 6, we present a study on surface functionalization of ZnO nanowalls using europium and terbium complexes. Since the characteristic luminescence of europium and terbium can be enhanced by the attached ligand, two appropriately chosen organic molecules (chelating agents), 1,10-phenanthroline (energy-mediator) and oxydiacetic acid (non-energy-mediator), are employed to synthesize lanthanoid complexes. The photophysical properties and chemical bonding nature of these lanthanoid complexes as synthesized and as surface-functionalized on ZnO are investigated. The energy-transfer mechanism from ZnO to lanthanoid complexes is constructed, and the surface interactions between ZnO and complexes are explored.

The overall objective of this thesis is to investigate quantum confinement effect in two dimensional ZnO nanostructures and energy transfer mechanism between these ultrathin nanostructures and lanthanoid cations. The present study provides new understanding of optoelectronic and luminescence properties of pristine and lanthanoid-doped ZnO nanostructures. By taking advantage of the quantum confinement effect, single-unit-cell thick ZnO quantum sheets could open new door to optoelectronic applications for these ultrathin two-dimensional nanomaterials. Investigating the photophysical properties of europium-doped and terbium-doped ZnO nanowalls provides new insight to understand the energy transfer mechanism of lanthanoid cations and the host materials. Surface functionalization of ZnO nanowalls with europium and terbium complexes delivers another method to modify and enhance the photophysical properties of ZnO. The chemical nature of the complexes and the resulting hybrid structures upon adsorption on ZnO nanowalls are investigated in detail, which provides new understanding of the energy transfer mechanism and photophysical properties of the ZnO/lanthanoid complex hybrid structures.

Chapter 2

Experimental Section

2.1 Electrochemical Deposition for Sample Fabrication

To fabricate ZnO nanostructures, conventional electrochemical deposition is carried out in an aqueous solution using a three-electrode electrochemical cell, consisting of a reference, a counter and a working electrode. An electrochemical cell is placed in the temperature-controlled water bath and is connected to an electrochemical station, CH Instruments CHI 660E. A typical setup of electrochemical deposition with a three-electrode electrochemical cell is shown in Figure 2.1. A potentiostatic amperometric method, which measures current flow as a function of deposition time at a constant potential, is adopted. An aqueous solution is used for electrochemical deposition and it usually contains the primary electrolyte that provides the major source of zinc cations, and a supporting electrolyte that increases the conductivity of the solution. A p-type Si wafer or an ITO-coated glass is selected as the working electrode and a Pt wire is used as a counter electrode. An Ag/AgCl electrode filled with 1 M aqueous KCl solution is chosen as the reference electrode to provide a standard point of applied voltage because its potential difference to the standard hydrogen electrode (defined as the zero potential) remains unchanged due to its constant compositions.^{141–143}

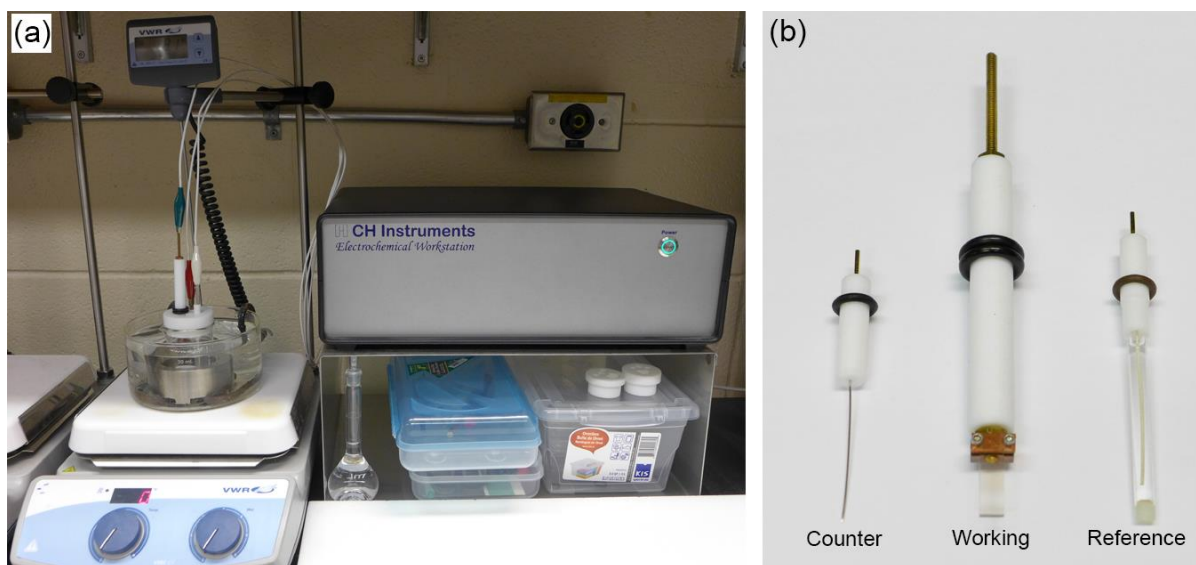


Figure 2.1(a) A standard three-electrode electrochemical deposition setup with (b) a Pt wire counter electrode, a substrate used as the working electrode, and a Ag/AgCl reference electrode.

2.2 Scanning Electron Microscopy, Transmission Electron Microscopy and Atomic Force Microscopy

Scanning electron microscopy (SEM), transmission electron microscopy (TEM) and atomic force microscopy (AFM) are employed to explore the morphological, microstructural and topographical information of the sample, respectively. The SEM is based on a similar principle to that of optical microscopy except it uses an electron beam instead of light to obtain an image of detailed information about the surface in reflective mode.¹⁴⁴ Irradiating a sample with an energetic electron beam generates several signals including secondary electrons, backscattered electrons, and characteristic X-rays. Secondary electrons (with kinetic energy < 50 eV) are used to build an image containing morphological information of the specimen. On the other hand, backscattered electrons (with kinetic energy > 50 eV) could be used to provide different contrast based on the atomic number (the so-called Z contrast) because backscattered electrons are generated by inelastic scattering between the incident electron and atoms in the specimen. Energy dispersive X-ray (EDX) analysis uses the emitted characteristic X-ray signals (as a result of the high-energy electron impact of the incident electron beam) to provide elemental composition information. In the present work, EDX is used to verify the presence of lanthanoid dopants in the sample before further chemical composition analysis by X-ray Photoelectron Spectroscopy or Auger Electron Spectroscopy. Figure 2.2a shows a photograph of a Zeiss Merlin microscope, a state-of-the-art field-emission SEM equipped with an in-lens and an external secondary electron detectors, two backscattered electron detectors, an EDX spectrometer, a charge compensation system, and a plasma sample cleaner.

Two different TEM systems, a FEI Tecnai F20 microscope from University of Calgary and a Zeiss Libra 200MC microscope on-campus (shown in Figure 2.2b), have been employed to obtain high-resolution TEM images and the structural information of ZnO nanostructures at different stages of the present work. Since a TEM utilizes electrons that pass through the entire sample, not only atomic resolution images of columns of atoms but also information regarding crystal structures can be obtained. The latter is achieved by performing selected area electron diffraction and/or fast Fourier transform (FFT) of the high-resolution TEM images. Samples for TEM analysis were often prepared by physically removing the ZnO nanostructures from the substrate and dispersing them in the water. This was then followed by placing a droplet of the aqueous solution containing ZnO nanostructures onto TEM grids with holey or lacey carbon. The high-resolution TEM images were acquired by

operating the TEM at 200 kV and the crystallographical information of ZnO nanostructures was achieved by a FFT process.

A Digital Instruments Dimension 3100 Scanning Probe Microscope (shown in Figure 2.3) was used to obtain topographical information. In atomic force microscopy (AFM), interactions between a probe tip and the sample surface generate repulsive and attractive forces. The sum of these forces is measured as a degree of cantilever deflection that is measured by the location of the laser beam on the photodiode detector.¹⁴⁴ The cantilever holder is controlled by a piezoelectric tube and offers extremely fine vertical resolution. AFM has three different operational modes: contact, tapping and non-contact mode. In contact mode, the tip is in contact with the surface of the sample and the system monitors the change or degree of the force or the height of the tip. In contrast, a tip is oscillating in non-contact mode (where the tip is not in contact with the surface) and tapping mode (where the tip is in intermittent contact with the surface), and the system measures the change in the resonance frequency in order to detect the variation in the force. Tapping mode is most popular for AFM operation, because it is less destructive than contact mode and is also easier to operate and more sensitive than non-contact mode.¹⁴⁵ In this study, sub-nanometer sized ZnO structures were explored by using tapping mode and the details are given in Chapter 3.

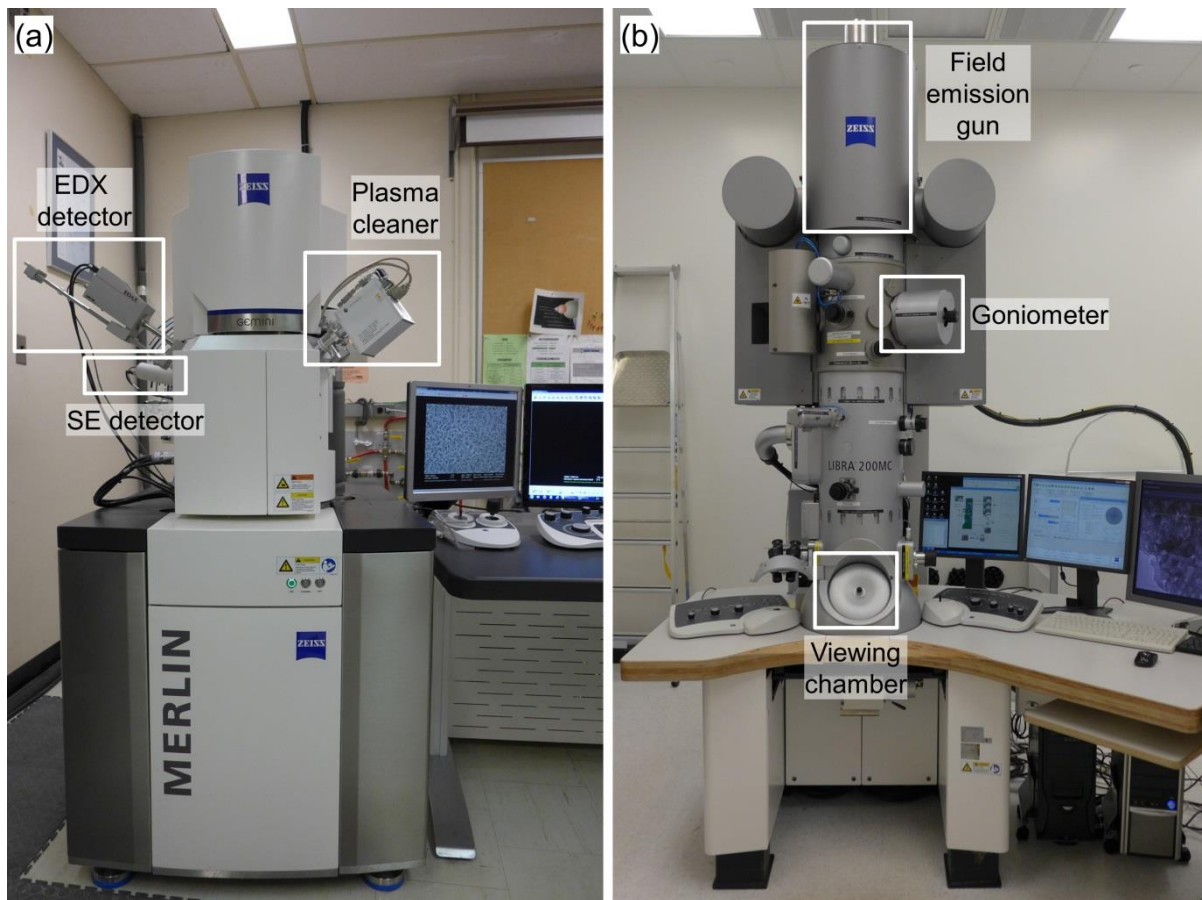


Figure 2.2 Photographs of (a) a Zeiss Merlin field-emission scanning electron microscope, and (b) a Zeiss Libra 200MC transmission electron microscope.

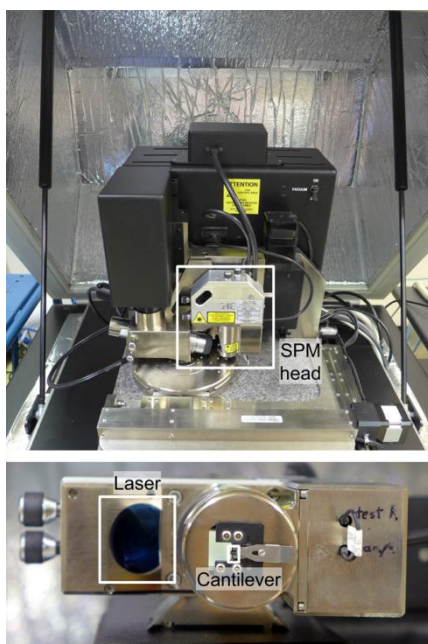


Figure 2.3 Photograph of a Digital Instruments Dimension 3100 Scanning Probe Microscope used for atomic force microscopy.

2.3 X-ray Photoelectron Spectroscopy and Auger Electron Spectroscopy

The chemical composition and bonding nature of pristine, doped and surface-functionalized ZnO nanostructures were analyzed by X-ray photoelectron spectroscopy (XPS) and Auger electron spectroscopy (AES). Figure 2.4 shows a schematic diagram of the photoelectron and Auger electron emission processes. Upon absorption of an X-ray photon with known photon energy ($h\nu$), photoelectrons with kinetic energy (E_K) are emitted from the sample and their kinetic energy is determined. For a known spectrometer work function (ϕ), the binding energy of the electron (E_B) in the sample before photoejection can be obtained from the Einstein equation: $E_B = h\nu - E_K - \phi$. Core-level binding energy shifts have been found to depend on the chemical environment of the atom within the molecule, and they can be used to provide chemical identification of the local bonding characters.¹⁴⁶ As only photoelectrons escaped without further collision are detected to generate the photopeaks at the characteristic energy (as defined by the Einstein equation), the XPS technique is therefore extremely surface sensitive. The generally short inelastic mean free path of an electron is 0.5 nm to 10 nm, depending on the kinetic energy of the photoelectrons (2-2000 eV). In the present

work, a Thermo-VG Scientific ESCALab 250 Microprobe, shown in Figure 2.5a, was employed for XPS analysis. By employing Ar^+ sputtering, XPS spectra can be collected as a function of sputtering depth, thus providing depth profiling composition analysis of the chemical states of the sample.

In AES, Auger electrons generated by the Auger electron emission process are detected. In the Auger electron emission process (Figure 2.4), an electron vacancy in an electron energy level is created by photoionization or high-energy electron impact ionization. In a radiation-less decay process, this vacancy is filled by an electron from the upper energy level. Any surplus energy from the energy difference between the vacancy level and the upper level can be transferred to another electron and results in its ejection from the atom. This departed electron is called the Auger electron. Auger electron emission is extremely surface sensitive due to the same restriction of inelastic mean free path as photoelectrons.^{144,147} For the Auger electron depicted in Figure 2.4, the Auger process is designated as the KL_2L_3 transition (in the order of vacancy level, origin of the electron filling the vacancy, and the origin of the ejected electron).^{144,146} In addition, by using a high-energy electron gun as the excitation source, a probe area of a few tenths of nanometers can be obtained, which provides a high spatial resolution for measuring the elemental composition of individual nanostructures. Figure 2.5b shows a Thermo MicroLab 350 AES system utilized for the present study.

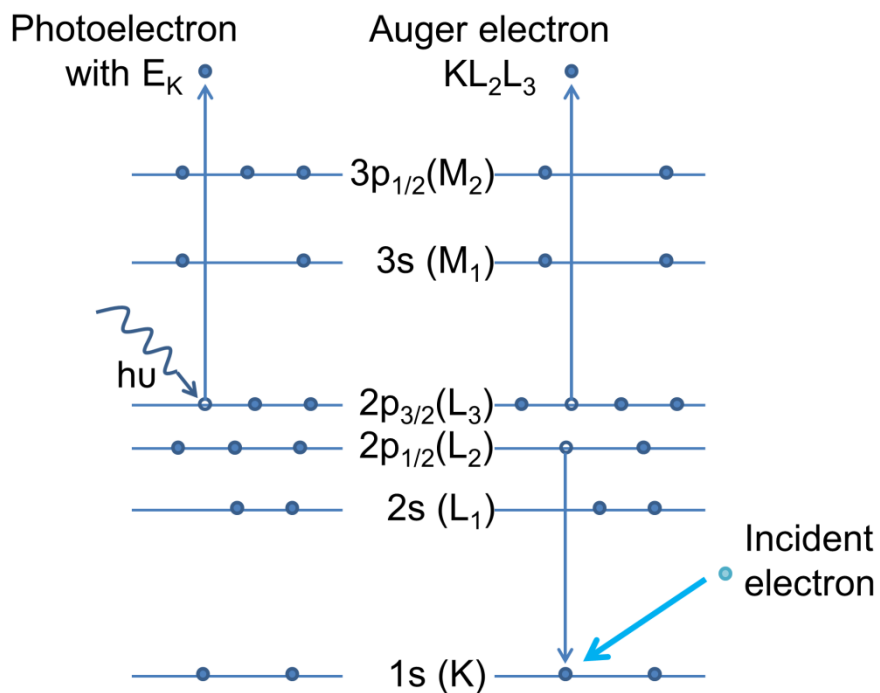


Figure 2.4 Schematic diagram of photoelectron and Auger electron emission processes.

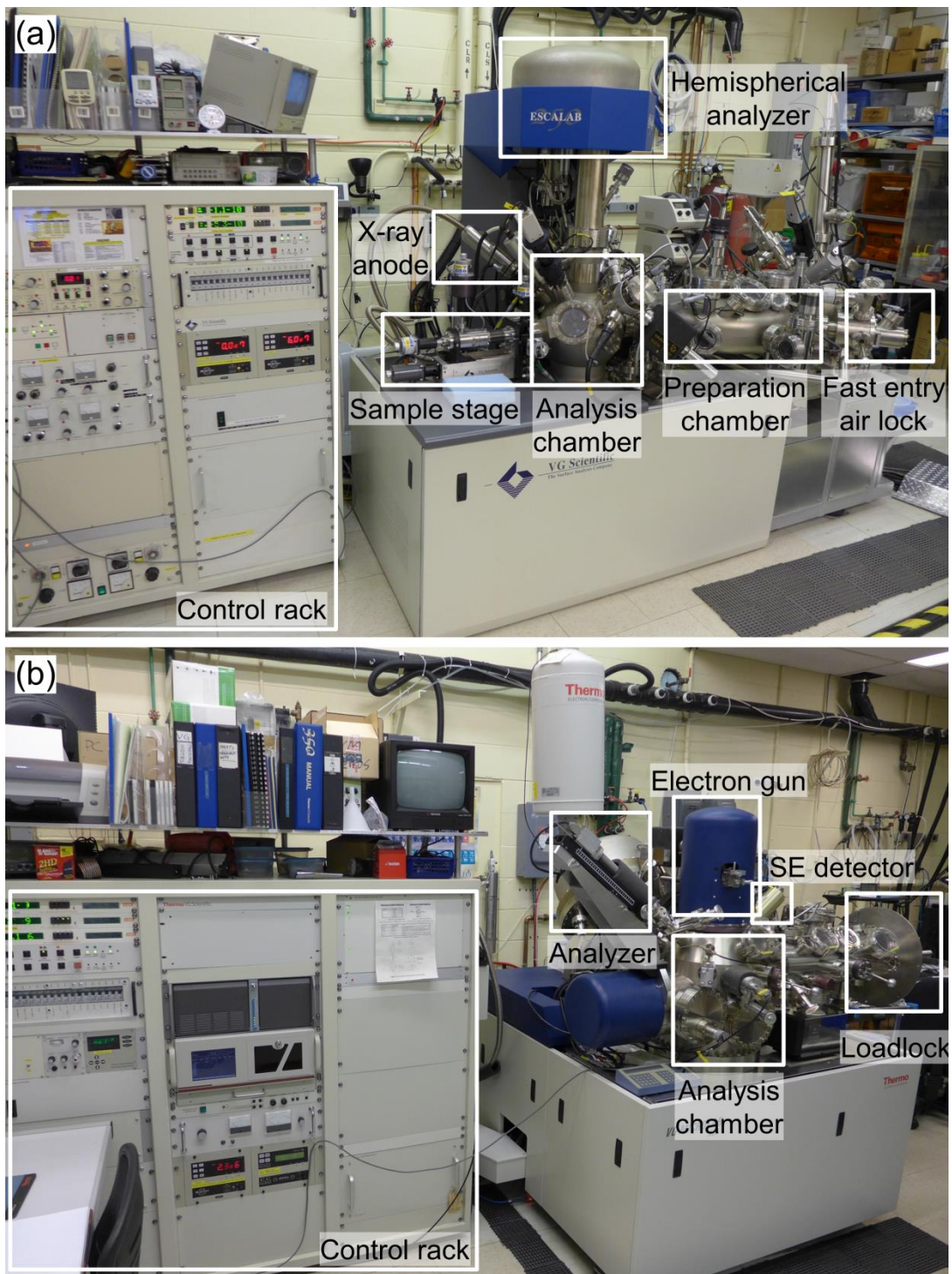


Figure 2.5 Photographs of (a) a Thermo-VG Scientific ESCALab 250 Microprobe used for photoelectron spectroscopy and (b) a Thermo Microlab 350 used for Auger electron spectroscopy.

2.4 UV-Vis Spectroscopy

To investigate the optoelectronic properties of ZnO nanostructures, UV-Vis diffuse reflectance spectroscopy was conducted by using a Perkin Elmer Lambda 1050 UV/Vis/NIR spectrophotometer equipped with a 150 mm integrating sphere module, shown in Figure 2.6. A sample was placed on the sample holder located at the outer shell of the integrating sphere and the diffuse reflectance of the sample was measured. The absorption spectra were obtained by converting the reflectance (R) to the absorption coefficient (α) by using the Kubelka-Munk equation: $\alpha/S = (1 - R)^2/(2R)$, where S is the scattering factor of the sample.¹⁴⁸ The Kubelka-Munk equation was developed for the diffuse reflectance measurement of the thin films such as paper, textile and paints,¹⁴⁹ often by making, for simplicity, several assumptions such as uniform thickness, diffusive and homogeneous illumination.¹⁵⁰ In the present work, diffuse reflectance spectra of ZnO quantum sheets were obtained and converted to absorption spectra to calculate the energy band gap of ZnO quantum sheets (Chapter 3).

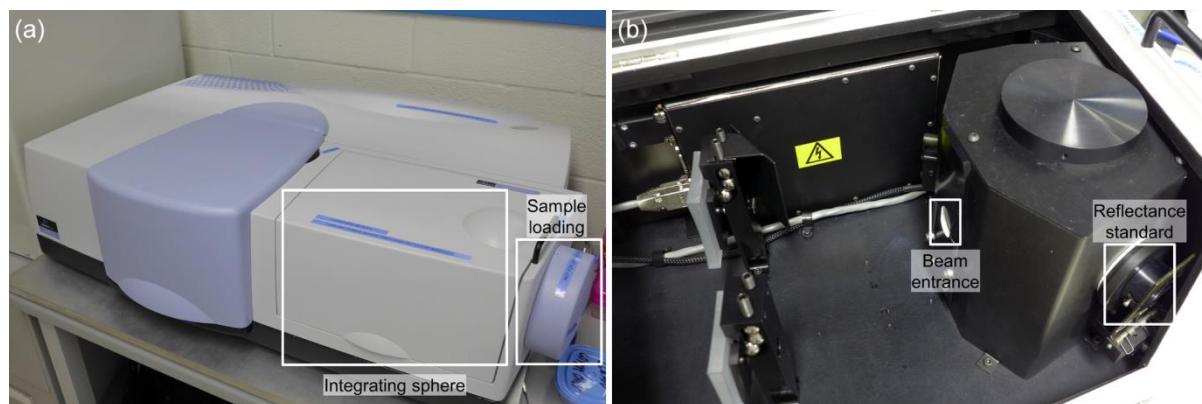


Figure 2.6 Photograph of (a) Perkin Elmer Lambda 1050 UV-Vis spectrophotometer and (b) the integrating sphere module used for diffuse reflectance measurement.

2.5 Luminescence Spectroscopy

When an excited molecule undergoes a radiative relaxation process to a lower energy level, the emission of light is called luminescence. There are two types of luminescence: fluorescence and phosphorescence. The former corresponds to a de-excitation transition between singlet states while the latter corresponds to a transition between a triplet excited state and a singlet ground state. In addition, luminescence can be further classified according to its excitation source. If the excitation source is provided by an electron beam, an electric current, chemical reactions or photons, the emission of light is referred to as cathodoluminescence, electroluminescence, chemiluminescence and photoluminescence, respectively. In the present work, the samples are excited by light irradiation, the emission process therefore corresponds to the photoluminescence process.

2.5.1 Photoluminescence and Excitation Measurement

The experimental setup was one of the few unique custom-built photoluminescence systems in the world. It was located at the Department of Chemistry, Chungnam National University (Daejeon, South Korea) and the luminescence studies reported in the present work were conducted in collaboration with Professor Jun-Gill Kang and his group at Chungnam National University. A photograph of the experimental setup is shown in Figure 2.7, with its schematic optics layout shown in Figure 2.8. In the present work, both a high-pressure 1000-W Xe arc lamp (Oriel) and a 30-mW 325 nm helium-cadmium laser (Kimmon Koha, IK3301R-G) were used as the excitation sources to generate the photoluminescence spectra. For photoluminescence measurement, the incident light wavelength was pre-selected while any light emitting from the sample was collected as a function of the (emitting light) wavelength. Depending on the excitation light sources, the resulting spectrum is referred as the PL (laser excitation) or emission (Xe arc lamp excitation) spectrum in the present work. With the sample placed in the sample holder, the sample was irradiated with incident light from the 325 nm He-Cd laser or the Xe arc lamp (operated with a working power of 600 W) passing through a Czerny-Turner monochromator with a focal length of 0.3 m (Acton SpectraPro SP-2300i, Princeton Instruments). For the light from the Xe arc lamp, two quartz lenses were used to control the focus of the incident light. The luminescence was then observed at 90° from the excitation light beam direction. The emitted radiation was focused by using two quartz lenses onto the entrance slit of a second 0.5 m Czerny-Turner monochromator (Acton Research Cooperation, VM-505) equipped with a cooled Hamamatsu R-933-14 photomultiplier tube powered by a high voltage power supply (Oriel). On the other hand, the excitation measurements were performed by fixing the wavelength of the

emitting light constant at an appropriately chosen value, while the wavelength of the incident light to the sample was varied over a pre-set range. The photomultiplier tube connected to the emission monochromator was used to measure the intensity change as a function of excitation wavelength. The resulting spectrum is referred as the excitation spectrum in the present work. For this type of experiments, a UV cut-off filter was placed before the emission monochromator (M2) to eliminate unwanted stray light and any second-order light from the excitation source. For experiments carried out with the sample held at different temperature ranging from 10 K to 300 K, the sample was mounted on the cold finger of a closed cycle liquid helium refrigerator (CCS-120, Janis Research Company) and the air was evacuated to prevent water and ice condensation on the surface of the sample.

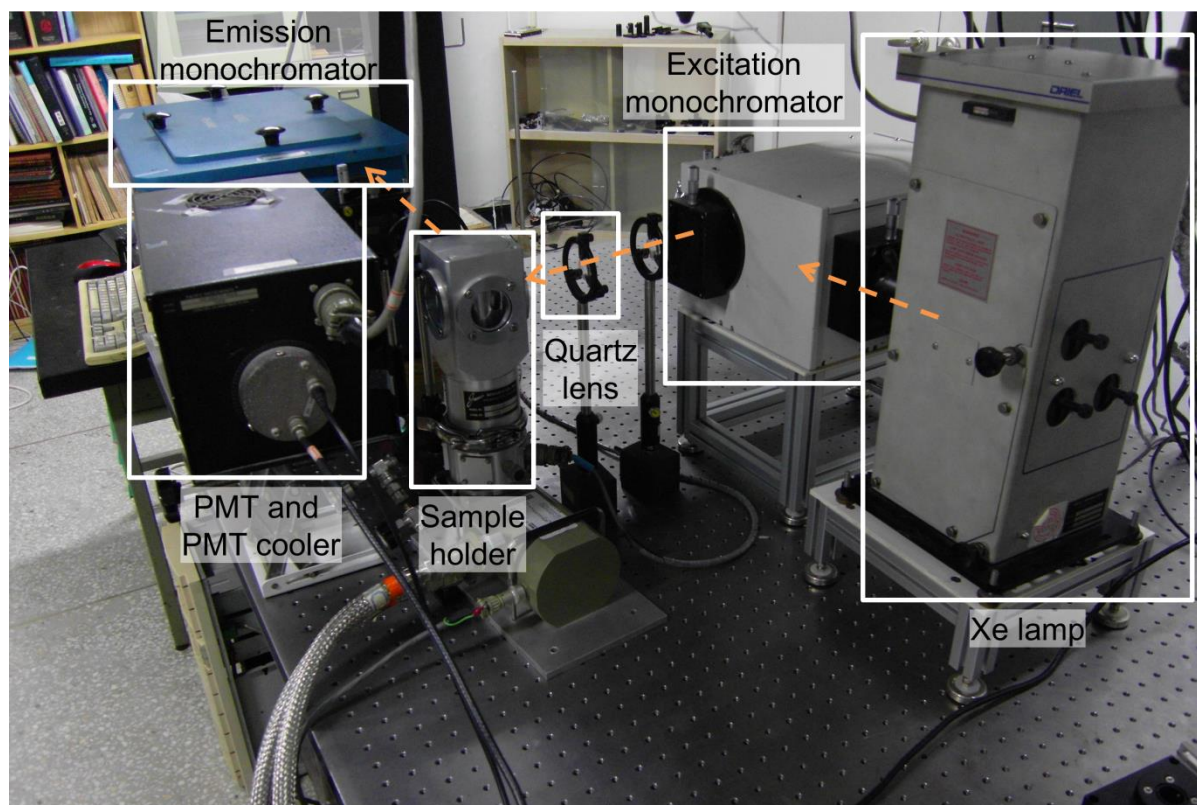


Figure 2.7 Photograph of the experimental setup depicting the light path (dotted lines) from the incident beam optics (right) to the sample chamber (center) to the exit beam optics (left).

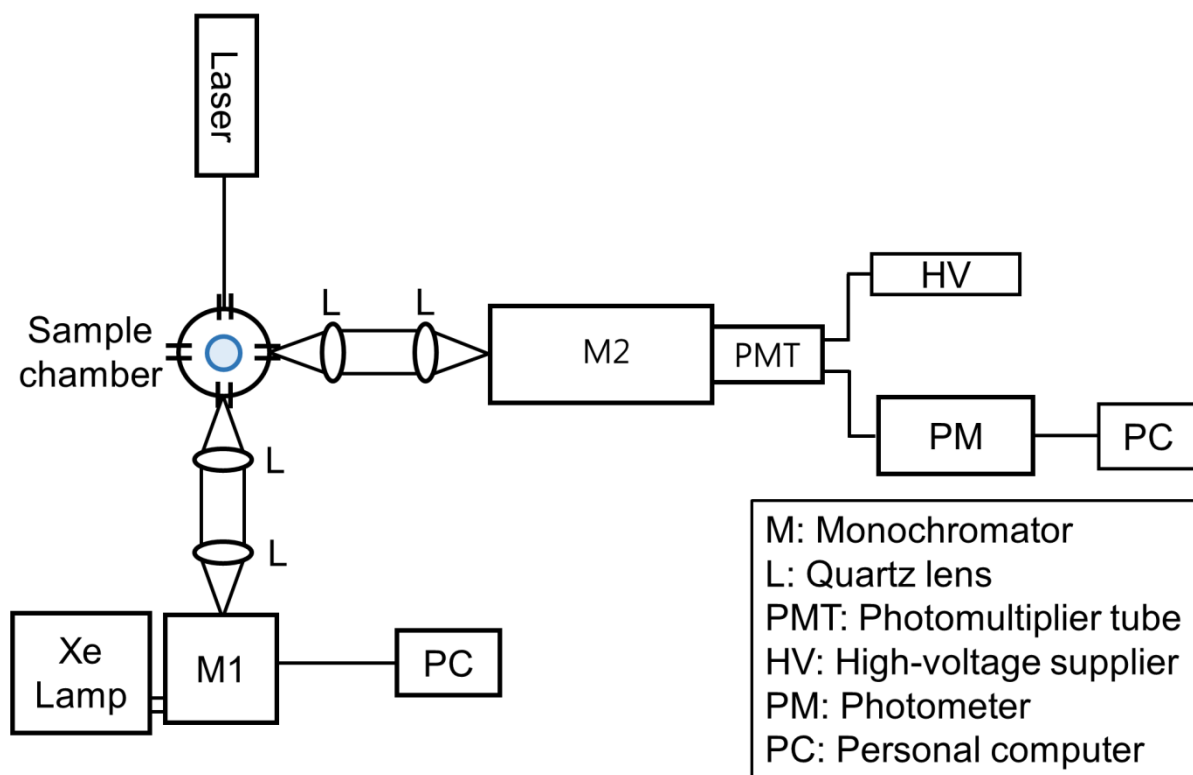


Figure 2.8 A schematic diagram of measurement setup for photoluminescence (emission) and excitation spectra.

2.5.2 Lifetime and Absolute Quantum Yield Measurement

Lifetime is defined as the average time that the molecules spent in the excited energy level before going through the photonic transitions. A schematic diagram of the experimental arrangement for photoluminescence lifetime measurement is shown in Figure 2.9. The sample was excited by light coming from a 56-mW 337.1 nm N₂ pulsed laser (GL-3300, Photon Technology International). The emitted light from the sample was detected at 90° from the excitation source and passed through the M2 monochromator coupled with a cooled Hamamatsu R-933-14 photomultiplier tube. The signal was fed to an oscilloscope (Agilent 54832B) triggered by the synchronized trigger source of the N₂ laser. The final result was obtained from averaging 300 individual measurements in order to improve the signal-to-noise ratio.

The quantum yield is determined by the ratio between the amount of the emitted photons from the sample and the amount of the photons absorbed by the sample. To eliminate the emission contribution

of the scattered and/or reflected light by the sample and/or the integrating sphere and to increase the accuracy of absolute quantum yield, three separate measurements were performed for each sample. Emission signals were measured from the following: (a) incident laser light with the empty integrating sphere (to obtain the background contribution), (b) incident laser light directed to the wall of integrating sphere such that there was no direct interaction with the laser (to obtain indirect excitation contribution), and (c) incident laser light directed at the sample (to obtain total emission). The final emission could then be computed from signal (c) – signal (a) – signal (b). More details are given in the work of de Mello et al.¹⁵¹ The experimental setup of measuring absolute quantum yield is similar to those of photoluminescence measurement (using the laser source). Instead of the sample holder, a 10 inch integrating sphere was used to house the sample.

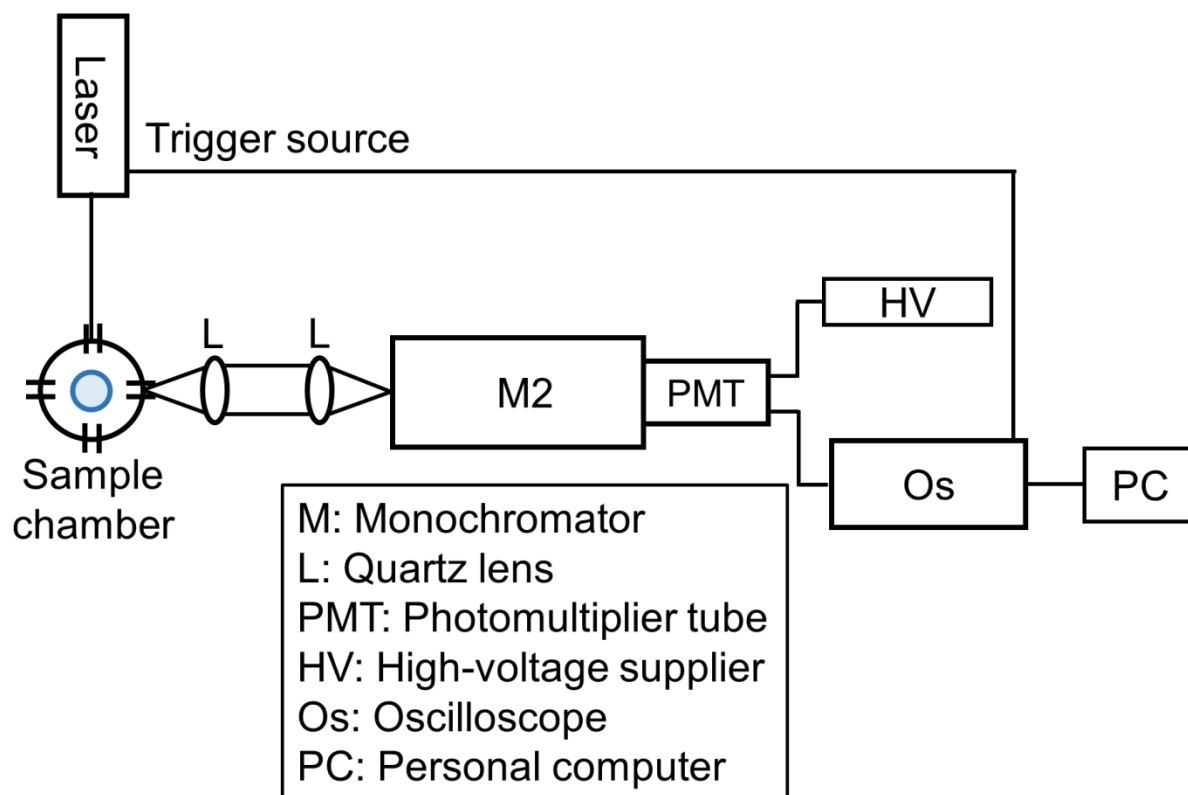


Figure 2.9 A schematic diagram of the photoluminescence lifetime measurement setup.

Chapter 3

Optoelectronic and Photophysical Properties of Zinc Oxide Quantum Sheets

3.1 Introduction

The size of nanostructures intimately affects their properties, especially their electronic and optoelectronic properties, because of the quantum confinement effect.¹⁵² The minimum thickness for elemental materials is the size of a single atom. For binary and multi-component systems, the dimension of a unit cell represents the lowest limit. To date, the single-unit-cell thick nanostructures have been discovered only for very few binary materials. Their potential applications, however, remain largely unexplored and are limited to ferromagnetism and catalysis.^{153–155} On the other hand, transparent conducting oxides (TCOs) are one of the most fascinating (binary) materials because of their optical transparency and metal-like conductivity.

As a TCO semiconducting material, Zinc Oxide (ZnO) has attracted great interest because of its wide direct band gap (~3.37 eV), large exciton energy (60 meV), good thermal and chemical stability, low toxicity and high biocompatibility.^{156–158} A broad range of potential applications of ZnO have been demonstrated for solar cells, light emitting diodes, sensors and nanogenerators.^{157,158} ZnO nanostructures can be deposited on various substrates by a variety of methods, including physical vapour, chemical vapour and wet-chemistry deposition. However, the parameters of many such deposition techniques could be quite demanding due to the needs of high deposition temperature, catalysts, expensive substrates, high post-growth annealing temperature, seed layer, environmentally hostile organic solvents or relatively longer deposition time.^{159–165} In contrast, electrochemical deposition offers a more facile alternative because ZnO deposition could be performed in a single step in an aqueous solution with a deposition time of less than 2 hours.^{43,166}

Since quantum confinement effect has unique influence on the optical, optoelectronic and electronic properties, various ZnO nanostructures were studied. However, acquiring nanostructures with size less than the small Bohr radius (2.34 nm) of ZnO has become a major obstacle to observe quantum confinement effect. Differences between energy band gaps of the bulk and ZnO quantum dots (~0.4 eV), nanowires and nanosheets (~0.2 eV) have thus far been found to be rather small because of larger size of these synthesized nanostructures..^{136,140,167–170} Here, we report the fabrication of single-unit-cell thick ZnO quantum structures on a Si substrate without using any pre- and post-

growth treatments such as seeding, annealing or exfoliation. We further show that the energy band gap of these single-unit-cell thick ZnO quantum sheet stacks can be varied over a wide range, from 4.51 to 3.35 eV, by manipulating the stack thickness as a function of deposition time.

3.2 Experimental Details

3.2.1 Fabrication of ZnO Quantum Sheets

ZnO quantum sheets were prepared by electrochemical deposition using a conventional three-electrode electrochemical system in a water bath. The deposition temperature was fixed at 10 °C and kept stable by controlling the temperature of the water bath using a recirculator. A 15 mL solution of 0.1 M $\text{Zn}(\text{NO}_3)_2 \cdot 6\text{H}_2\text{O}$ (98%, Sigma-Aldrich) mixed with 0.1 M KCl ($\geq 99.0\%$, Sigma-Aldrich) serving as a supporting electrolyte was used as the electrolyte. Si(100) wafer was prepared by using the RCA cleaning method and was used as the working electrode. Electrochemical depositions were carried out at an applied potential of -1.1 V with respect to a Ag/AgCl reference electrode and with a Pt wire serving as the counter electrode. The deposition time was varied to control growth of the ZnO quantum sheets.

3.2.2 Characterization Methods

The surface morphology was examined by using field-emission scanning electron microscopy (SEM) in a Zeiss Merlin microscope. Atomic force microscopy (AFM) was used to investigate the topography and thickness of ZnO quantum sheets in a Digital Instruments Dimension 3100 Nanoscope IV. Transmission electron microscopy (TEM) was performed on a few layers of the ZnO quantum sheets on a holey carbon grid in a FEI Tecnai F20 microscope operated at 200 kV. Diffuse reflectance spectra were collected by using an UV-Vis spectrometer (Perkin Elmer Lambda 1050) equipped with a 150 mm integrating sphere module (Labsphere). X-ray photoelectron spectroscopy (XPS) was used to investigate the chemical composition of ZnO quantum sheets as a function of sputtering depth in a Thermo-VG Scientific ESCALab 250 Microprobe equipped with a monochromatic Al K α source (1486.6 eV). For photoluminescence (PL) and excitation spectroscopic measurements, the sample was irradiated by a 1000-W Xe arc lamp (Oriel, operating power 600 W) with an excitation monochromator (Acton SP-2300i). The emission from ZnO quantum sheets was monitored by a 0.5-m Czerny-Turner monochromator (ARC) equipped with a cooled Hamamatsu R-933-14 photomultiplier tube.

3.3 Results and Discussion

3.3.1 Morphology and Topography of ZnO Quantum Sheets

Figure 3.1 shows the scanning electron microscopy (SEM) images of single-unit-cell thick ZnO quantum sheets electrodeposited on Si(100) substrates at 10 °C for different deposition times. For 1 min and 5 min depositions, the quantum sheets appear fan-shaped and with the dimensions of 500 nm \times 500 nm (Figures 3.1a and 3.1b). As we increase the deposition time, the size and density of the quantum sheets gradually increase, expanding the coverage of the quantum sheets over the entire substrate uniformly. Wrinkling of quantum sheets is also observed, which is likely due to the large surface energy. The quantum sheets could grow to micron size with longer deposition times (Figures 3.1c and 3.1d).

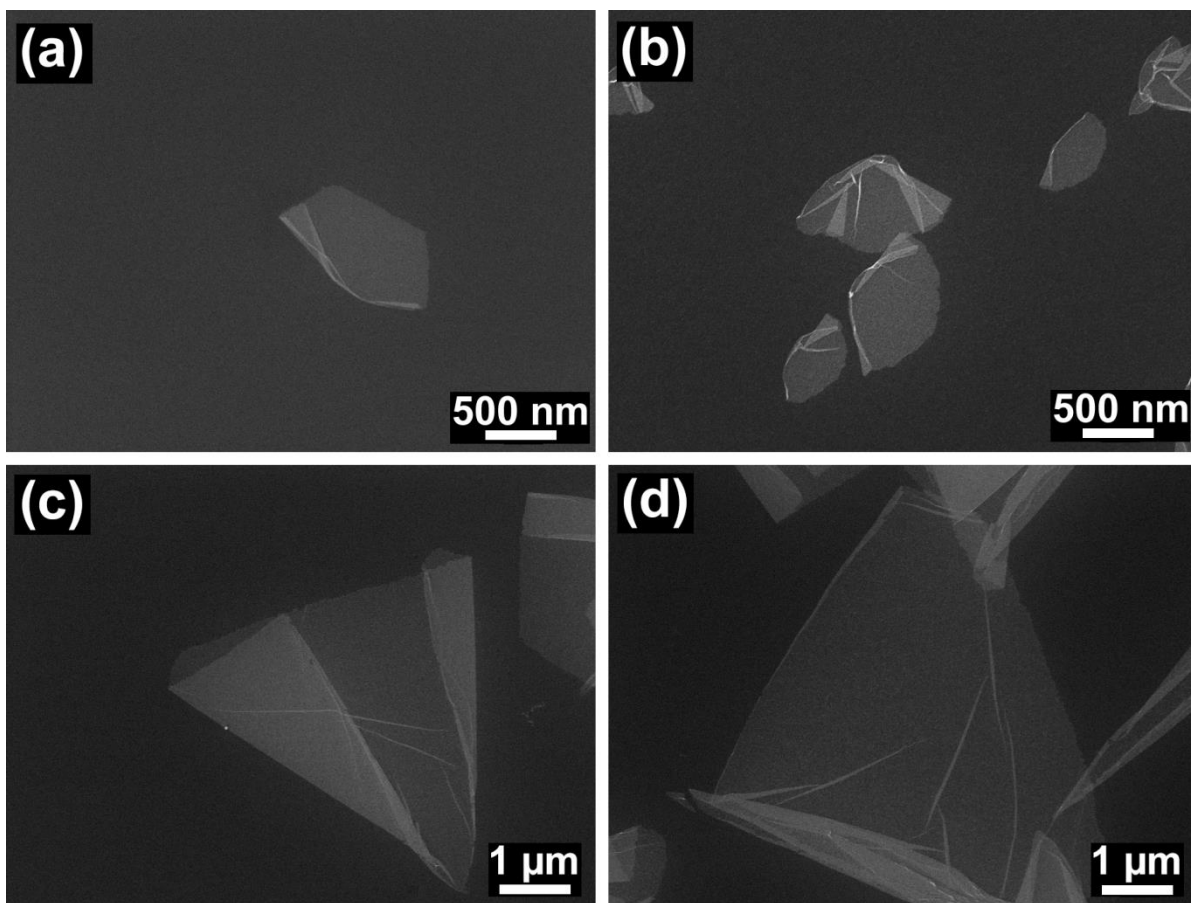


Figure 3.1 SEM images of electrochemically deposited ZnO quantum sheets at 10 °C for (a) 1 min, (b) 5 min, (c) 30 min, and (d) 60 min.

Atomic force microscopy (AFM) studies are employed to investigate the thickness of ZnO quantum sheets. The AFM image of ZnO quantum sheets obtained with a 30 min deposition time, shown in Figure 3.2a, clearly illustrates two steps, while the corresponding height profile along the linescan across the steps, shown in Figure 3.2b, can be used to determine the thickness of the quantum sheet. The height from the Si substrate to the lowest lying quantum sheet (first step) and that from this quantum sheet to a second higher lying quantum sheet (second step) are 0.84 nm and 0.56 nm, respectively. As the first step corresponds to the thickness of a quantum sheet plus a small gap between this sheet and Si substrate, the second step therefore better represents the thickness of the ZnO quantum sheet. The height of the second step, 0.56 nm, is an excellent match to the inter-planar spacing along the c-axis of the ZnO unit cell (0.52 nm, JCPDS 00-036-1451). This provides strong evidence that the growth mechanism of ZnO quantum sheets is layer-by-layer growth, which indicates that individual quantum sheets maintain single-unit-cell thickness regardless of the deposition time and that the layer-by-layer growth of ZnO quantum sheets occurs along the a- or b-axis direction. This is in good accord with the growth direction of ZnO quantum sheets revealed by high resolution TEM (HRTEM) shown in Figures 3.2c and 3.2d. Acquiring a HRTEM image of a single quantum sheet (retrieved onto a holey carbon TEM grid) is particularly challenging because of its fragility and its sensitivity to the 200 kV electron beam. Instead of a single ZnO quantum sheet, we collected HRTEM images of a few layers of ZnO quantum sheets. Figure 3.2d shows a HRTEM image with a lattice spacing of 2.7 Å, corresponding to the [100] direction of ZnO. Figure 3.2e shows a schematic model of the growth of double layers of single-unit-cell thick ZnO quantum sheets on a Si substrate based on the AFM and HRTEM results.

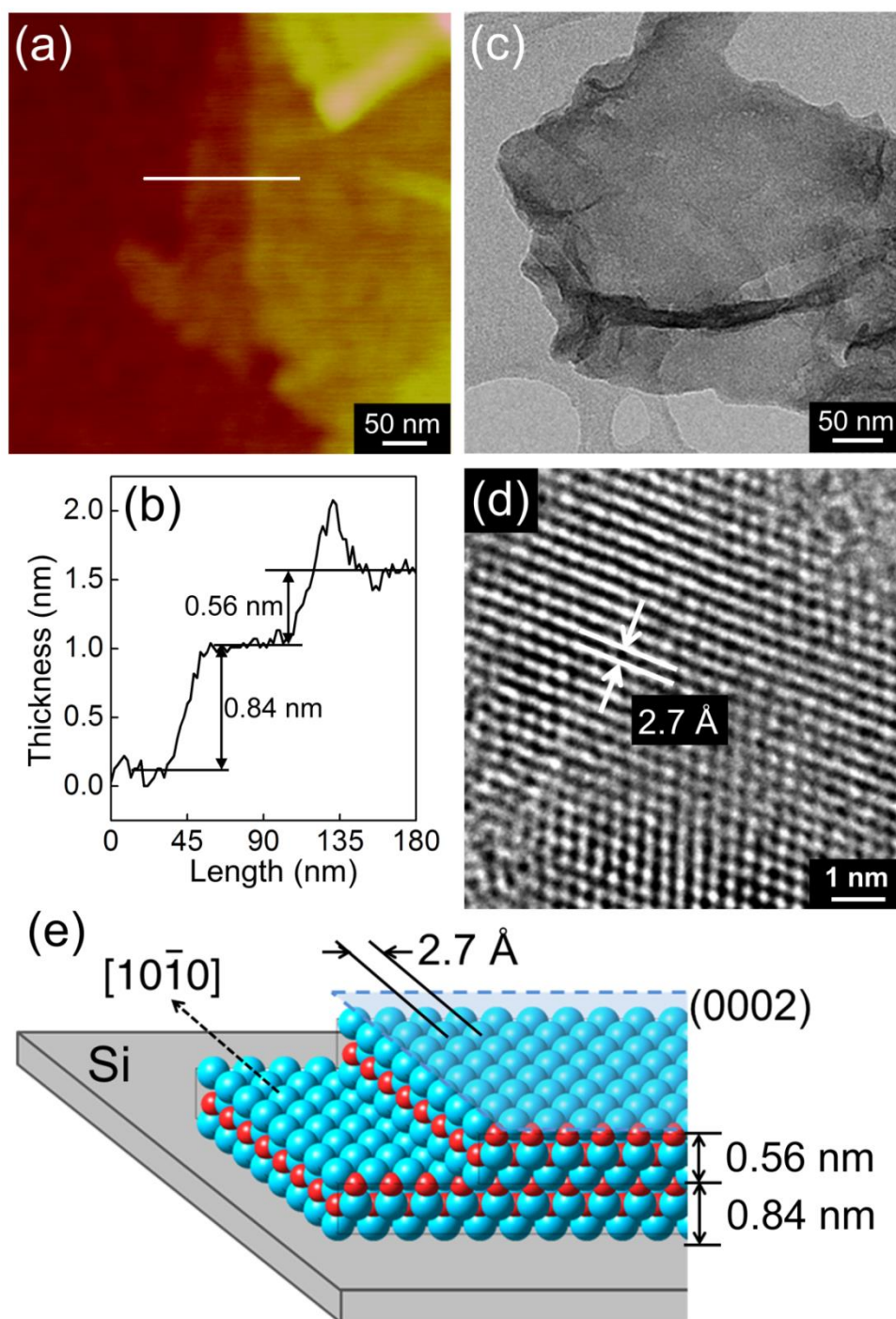


Figure 3.2 (a) AFM image of single-unit-cell thick ZnO quantum sheets deposited directly on a Si substrate and (b) its sectional analysis along the linescan marked by the white line in (a). (c) TEM and (d) HRTEM images of ZnO quantum sheet stacks. (e) Schematic molecular model of two layers of single-unit-cell thick ZnO quantum sheets.

3.3.2 Chemical Analysis of ZnO Quantum Sheets

Chemical composition analysis of as-grown ZnO quantum sheet is performed by using X-ray photoelectron spectroscopy (XPS). Figure 3.3 shows the XPS spectra of Zn 2p, O 1s and Cl 2p regions of ZnO quantum sheets as a function of sputtering time. For the as-prepared sample, XPS peaks are found at higher binding energies than their respective reference positions, and they gradually shift to lower binding energies with increasing sputtering time. This change in the peak positions is due to minor sample charging effect caused by the presence of non-conducting Zn(OH)₂ on the sample surfaces (in accord with the formation mechanism of ZnO).^{171,172} The Zn 2p_{3/2} (2p_{1/2}) feature located at 1022.3 eV (1045.4 eV), with a spin-orbit splitting of 23.0 eV (± 0.1 eV), is well matched with the literature value for the Zn²⁺ state.¹⁷³ This result is in good accord with the presence of a single Zn(II) divalent state corresponding to both ZnO and Zn(OH)₂. Upon 180 s sputtering, the O 1s spectra (Figure 3.3b) clearly show two peaks at 532.9 eV and 531.2 eV, attributed to Zn(OH)₂ and ZnO, respectively, in excellent agreement with the O 1s spectrum of ZnO powder (Figure 3.3d). Upon further sputtering, the Zn(OH)₂ component decreases significantly, confirming that its existence is limited to the near-surface region of the sample.

It is well known that the growth of ZnO nanostructures is greatly affected by the electrolyte concentration. The Cl⁻ ion plays an important role in the growth of two-dimensional ZnO nanostructures, in which the adsorption of Cl⁻ ions on the (0001) crystal plane obstructs the growth in the [0001] direction, thereby limiting the growth to two-dimensional structures.¹⁷⁴ The presence of Cl⁻ ion as shown in Figure 3.3c therefore confirms this two-dimensional growth mechanism for our ZnO quantum sheets.

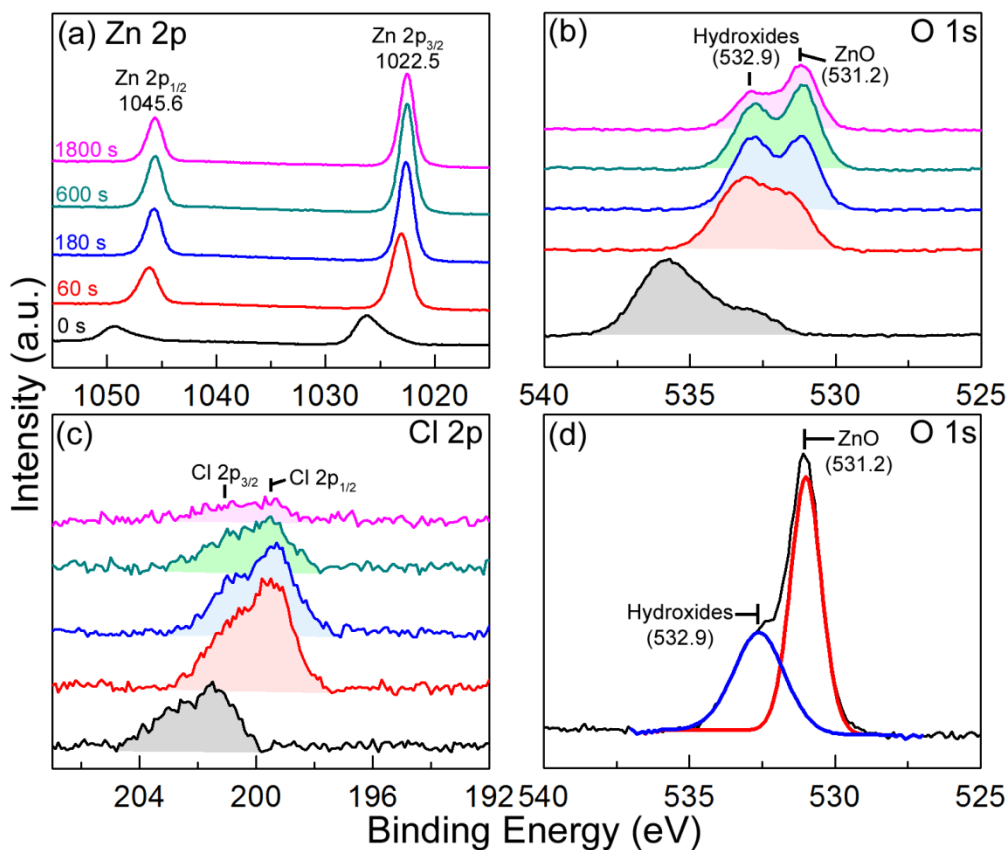


Figure 3.3 XPS spectra of (a) Zn 2p, (b) O 1s, and (c) Cl 2p as a function of sputtering time from 0 s (i.e. as-deposited), to 60 s, 180 s, 600 s and 1800 s for electrochemically deposited ZnO quantum sheets obtained with 60 min deposition time. (d) O 1s XPS spectrum of a ZnO powder sample.

3.3.3 Optoelectronic and Photophysical Properties of ZnO Quantum Sheets

Since the reported Bohr radius of ZnO (2.34 nm) is larger than the thickness of quantum sheet stack, quantum confinement effect is expected for the ZnO quantum sheets.¹⁷⁰ Optical properties of ZnO quantum sheets and bulk (pellet) are examined by UV diffuse reflectance spectroscopy, and the resulted spectra are shown in Figure 3.4. The absorption coefficient α can be obtained from the reflectance R by the Kubelka-Munk equation: $\alpha/S = (1 - R)^2/(2R)$, where S is the scattering coefficient. Due to its limited amount of material, the quantum sheets obtained with the shortest deposition time (1 min) do not provide sufficiently detectable signal in the UV absorption curve. For ZnO quantum sheets obtained with 5 min, 30 min and 60 min deposition time, absorption cut-offs

located, respectively, at 225 nm, 275 nm and 370 nm are observed and marked with black lines in Figure 3.4.

To further investigate the photophysical properties, emission and excitation spectra of ZnO quantum sheets are measured and shown in Figure 3.5. ZnO quantum sheets are excited at the higher-energy wavelengths of the three aforementioned absorption cut-offs (Figure 3.4). For excitation at 350 nm, the first absorption cut-off does not produce any PL emission, as is similarly found for the absorption cut-off of ZnO bulk powder. On the other hand, ZnO quantum sheets excited at 240 nm shows a strong blue-shifted emission spectrum, specifically with a ZnO band-edge emission shift by 91 nm and a ZnO defect emission shift by 124 nm, and the overall spectral shape resembling that of the emission of ZnO nanowalls. Instead of the bulk state (provided by ZnO powder), nanowall structure is used to compare with quantum sheets due to the strong defect emission (at 561 nm) generated by ZnO nanowalls and essentially the same band-edge emission position (at 376 nm) found for both the bulk and the nanowalls. The spectral envelopes of ZnO quantum sheets and nanowalls are remarkably similar. Evidently, ZnO quantum sheets exhibit relatively stronger defect emission than nanowalls, likely due to the physical wrinkles found in the quantum sheets. The blue emission from ZnO quantum sheets excited by a standard 254 nm UV lamp is shown in a photograph in Figure 3.4 inset. In addition, this emission is sufficiently powerful to be easily seen with naked eye. The corresponding excitation spectrum (for emission wavelength set at $\lambda_{\text{ems}} = 450$ nm) shows a well resolved peak between 235 nm and 300 nm (Figure 3.5, inset), which suggests that the energy band gap of ZnO quantum sheets is 4.51 eV.

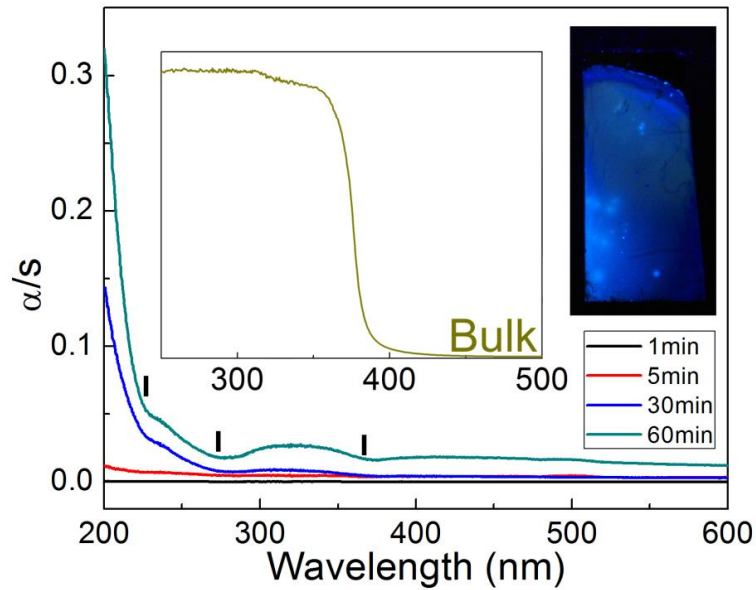


Figure 3.4 UV absorption spectra of ZnO quantum sheets electrodeposited on Si for various deposition times (absorption cut-offs are marked with black vertical markers) and of ZnO bulk powder (left inset). Right inset shows the photograph of ZnO quantum sheets on Si exposed to UV light (at 254 nm).

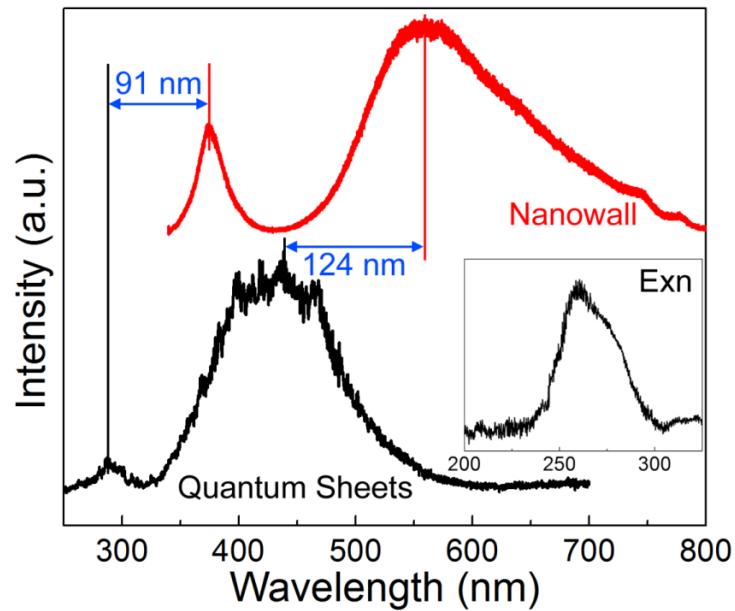


Figure 3.5 Emission spectra ($\lambda_{\text{exn}} = 240 \text{ nm}$) and excitation spectrum (inset, $\lambda_{\text{ems}} = 450 \text{ nm}$) of ZnO quantum sheets (lower) and nanowalls (upper). Blue shifts for the band edge and defect emissions between the ZnO quantum sheets and nanowalls are marked.

The PL spectra and UV diffuse reflectance spectra therefore demonstrate the quantum confinement effect on the energy band gap of ZnO quantum sheets. Several studies have reported quantum confinement effect on 0-D structures (quantum dots) and 1-D structures (nanorods), but influence on 2-D structures has yet to be presented. To discover the details of quantum confinement effect on electronic band structure, XPS spectra of the valence band region of ZnO bulk powder and quantum sheets are collected and shown in Figure 3.6a. The energy scale of the spectra has been calibrated by the position of Zn $2p_{3/2}$ (at 1022.5 eV). The valence band maxima of the bulk powder and quantum sheets are determined by the intersection of the linear fit of the photoemission edge with the background, and they are found to be 3.17 eV and 3.45 eV below the Fermi level, respectively. Based on these results, the corresponding conduction band minima of the bulk and quantum sheets are calculated and the resulting valence band structures are shown schematically in Figure 3.6b. Comparison between the bulk and quantum sheets reveals that the valence band maximum and conduction band minimum of the quantum sheets are respectively, 0.28 eV lower and 0.98 eV higher than those of the bulk, respectively.

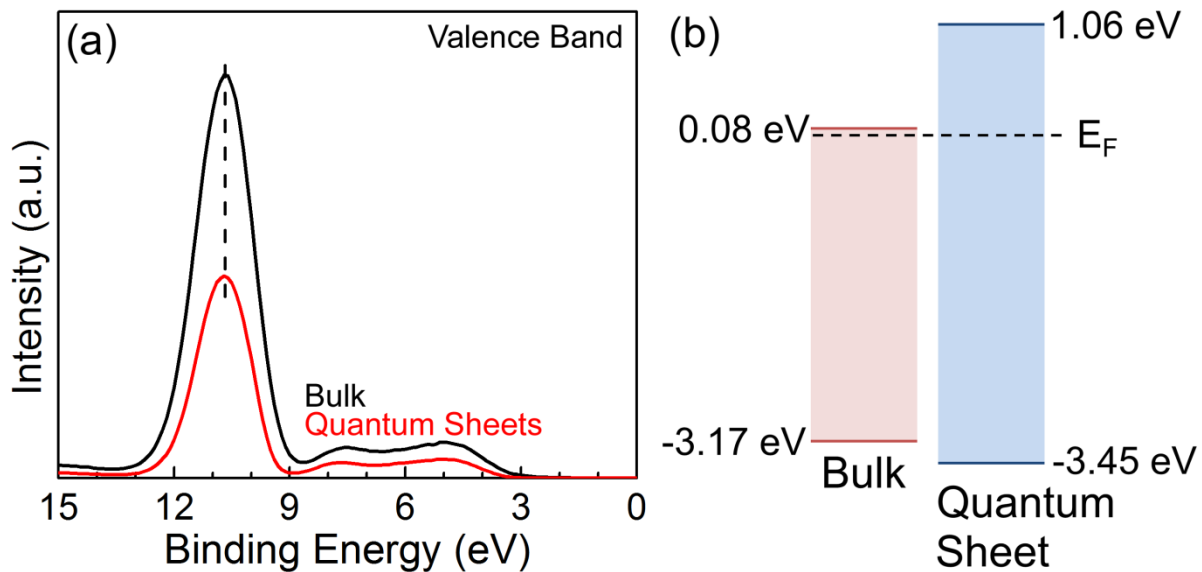


Figure 3.6 (a) XPS valence band spectra of ZnO bulk powder (black) and quantum sheets (red) and (b) schematic diagram of the valence band maxima and conduction band minima of ZnO bulk and quantum sheets.

The quantum confinement effect depends on the smallest dimension of the nanostructure. In 2D nanostructures, the thickness of the quantum sheet plays a vital role in the observed increase in the band gap (given the large length and width of a quantum sheet relative to its thickness).¹² The observed increase in the energy band gap of the quantum sheet by over 1.1 eV from the bulk value is therefore significant and can be attributed to the quantum confinement effect. From Figure 3.4, the absorption cut-off profiles of ZnO quantum sheet samples generally increase in intensity with increasing area and thickness of the quantum sheets. The corresponding profile for the 60-min sample shows that the intensity of absorption cut-off at 370 nm matches that of the bulk sample. Consistent with the growth mechanism of quantum sheets, height profile analysis of a large number of AFM images, however, indicates that the thickness of individual quantum sheets is the same regardless of the amount of deposition time. These results therefore suggest that electrostatic interactions between the quantum sheets lead to quantum sheet stacks with the overall thickness that governs the observed changes in the intensity of the absorption cut-offs and in the energy band gaps.

As the quantum sheets start to stack on top of one another during the layer-by-layer growth, orbital reconstruction occurs between the interfacial ZnO hybridized orbitals of individual quantum sheets, thus making up the quantum sheet stacks. In particular, orbital reconstruction induces band dispersion of the quantum sheet stacks such that the highest occupied molecular orbital (HOMO) in the valence band is raised while the lowest unoccupied molecular orbital (LUMO) in the conduction band is lowered. As a result, the energy gap between the resulting HOMO and LUMO becomes smaller than that before orbital reconstruction. As ZnO quantum sheets are accumulated by the layer-by-layer stacking, they behave more like the bulk, even though individual constituent quantum sheets remain quantum confined. For the 30-min deposited sample, the absorption peak demonstrates the presence of stacks of single-unit-cell thick quantum sheets with increasing overall thickness that leads to a smaller band gap. Comparing the 60-min sample with the 30-min sample, some of the quantum sheet stacks obtained from the 60-min deposition are sufficiently thick to behave like the bulk. This produces the biggest intensity increase in the bulk-like absorption cut-off among three absorption peaks. Our UV absorption results therefore demonstrate that modification of band gap energy of single-unit-cell thick ZnO quantum sheet stacks can be achieved by controlling the overall stack thickness through the deposition time.

3.4 Summary

The single-unit-cell thick ZnO quantum sheets are successfully deposited on a Si wafer by electrochemical deposition. By lowering deposition temperature near 0 °C, ZnO quantum sheets are obtained without any pre- and post-growth treatment. HRTEM and AFM studies reveal that individual ZnO quantum sheet have a similar growth mechanism as other 2-D ZnO nanostructures. Instead of thickness increment of a single quantum sheet, layer-by-layer stacking is observed with increasing deposition time. Due to its thickness, the electronic structure of ZnO quantum sheets is affected by the quantum confinement effect. PL measurement shows that ZnO quantum sheets have very deep UV and blue emissions. The energy band gap of ZnO quantum sheets is found to expand by more than 1.1 eV, with the valence band maximum and conduction band minimum, respectively, 0.28 eV lower and 0.98 eV higher than those of the bulk.

Chapter 4

Observation of Mediated Cascade Energy Transfer in Europium-doped ZnO Nanowalls by 1,10-Phenanthroline^{‡‡}

4.1 Introduction

Rare earth transition metal doped ZnO nanomaterials are recognized as promising candidates for applications in optoelectronics, light-emitting devices, spintronics and photocatalysis.^{175–184} Among rare earth ions, the trivalent Eu(III) ion has attracted great interest because of its unique optical properties, arisen from the hypersensitive $^5D_0 \rightarrow ^7F_2$ red emission (~620 nm) from Eu(III).^{185–187} Recently, nanostructured Eu-doped ZnO has been prepared by various methods, including hydrothermal synthesis, thermal evaporation, electrochemical deposition, sol-gel, and laser ablation.^{123,124,188–198} These techniques produced Eu-doped ZnO nanostructures with various morphologies including nanospheres, nanoparticles, nanoneedles, nanorods, nanowires and nanoflowers.^{192–197} Upon excitation by UV irradiation, these Eu-doped ZnO (written here as ZnO:Eu(III)) nanomaterials produced a band-edge emission at 369 nm and a broad defect-emission at 500–750 nm from ZnO, and/or a red emission from Eu(III). The appearance of the red emission was dependent on the excitation energy and on whether thermal annealing has been performed or not. The Eu(III)-related luminescence arisen from the band-gap excitation has been discussed in terms of the energy transfer from ZnO to Eu(III).^{182,196,198} Alternatively, the red emission from ZnO:Eu(III) nanospheres and nanorods could also be attributed to the direct excitation of Eu(III) to a charge-transfer state, instead of the energy transfer pathway.¹⁹⁷

Detailed knowledge of the structural and optical properties of ZnO:Eu(III) nanostructured materials grown on a selected substrate is important to industrial applications. Extensive research has been conducted to deposit ZnO films or nanostructures on a transparent substrate like indium tin oxide coated glass (ITO-glass), and to characterize their structural, optical and electrical properties.^{199–207} The deep-level emission from ZnO, appearing in the visible region, has been found to be highly dependent on its morphology, defects and doping.^{31,207–212} Here, we fabricate ZnO nanowalls doped with various concentrations of Eu(III) on ITO-glass by a simple electrochemical deposition method

^{‡‡} This chapter is adapted with permission from Kang, J.-S.; Jeong, Y.-K.; Kang, J.-G.; Zhao, L.; Sohn, Y.; Pradhan, D.; Leung, K. T. Observation of Mediated Cascade Energy Transfer in Europium-Doped ZnO Nanowalls by 1,10-Phenanthroline. *J. Phys. Chem. C* **2015**, *119* (4), 2142–2147. Copyright 2015 American Chemical Society.

and investigate the photophysical properties of the prepared nanowalls on ITO-glass. We also clarify the change in the chemical-state composition of Eu by depth-profiling X-ray photoelectron spectroscopy (XPS). Furthermore, by functionalizing the surface of ZnO:Eu(III) nanowalls using an ultraviolet range energy donor such as 1,10-Phenanthroline (phen), we investigate its effect on the photoluminescence (PL) of the Eu-doped ZnO nanowalls. We propose a cascade energy transfer model from ZnO to Eu(III) via phen, in order to provide new insight to the emission and energy transfer processes in surface-functionalized ZnO:Eu(III) nanostructures.

4.2 Experimental Section

Europium-doped ZnO nanowall structures were prepared by electrochemical deposition at 70°C, described in detail elsewhere.^{43,213} Briefly, we employed a potenti/galvanostat electrochemical workstation (CH Instruments 660A) and a three-electrode glass cell, with a Ag/AgCl reference electrode and a Pt wire counter electrode. The working electrode was single-sided polished, SiO₂-passivated float glass coated with an ITO film (200-500 nm thick with a sheet resistance of 4-8 ohm) obtained from Delta Technologies Limited (Minnesota, USA). ZnO nanowall structures were deposited at -1.2 V vs Ag/AgCl by amperometry in a solution of 0.1 M Zn(NO₃)₂·6H₂O (Sigma-Aldrich, ≥99.0% purity) with 0.1 M KCl used as the supporting electrolyte. To prepare Eu-doped ZnO nanowalls, we simply added Eu(NO₃)₃·5H₂O (Sigma-Aldrich, 99.9% purity) solutions of different concentrations (0.01, 0.05 and 0.10 M) to the electrolyte solution and follow the electrochemical deposition procedure. After the deposition, we rinsed the samples with Millipore water thoroughly and dried under nitrogen flow before analysis. Surface modification of Eu-doped ZnO nanowalls were performed by dipping the samples into 1,10-phenanthroline (Sigma-Aldrich, ≥99% purity) or ethylenediamine (Sigma-Aldrich, ≥99.5% purity) with various concentrations. For both cases, CH₂Cl₂ (Sigma-Aldrich, ≥99.9% purity) was used as a solvent.

Scanning electron microscopy (SEM) images were obtained using a field-emission Zeiss UltraPlus microscope. For depth-profiling X-ray photoelectron spectroscopy, we utilized a Thermo-VG Scientific ESCALab 250 Microprobe with a monochromatic Al K α source (1486.6 eV), and an energy resolution of 0.4-0.5 eV full width at half-maximum. For photoluminescence and excitation spectroscopic measurements, an excitation source of a He-Cd 325 nm laser line and an Oriel 1000 W lamp (operated at 600 W) with an Oriel MS257 monochromator were used, respectively. The spectra were taken by an ARC 0.5 m Czerny-Turner monochromator and a cooled Hamamatsu R-933-14 photomultiplier tube.

4.3 Results and Discussion

4.3.1 Morphologies of Eu-doped ZnO Nanowalls

Figure 4.1 shows the SEM images of undoped and Eu-doped ZnO nanowalls. For the undoped ZnO sample, the ledge thickness of the pristine nanowalls is measured to be 50-100 nm (Figure 4.1a). On the other hand, Eu-embedded ZnO nanowalls are found to be stacked together, forming relatively thicker structures with the ledge thickness of 150-400 nm for 0.01 M Eu-doped nanowalls (Figure 4.1b) and 300-700 nm for 0.05 M (Figure 4.1c) and 0.10 M Eu-doped nanowalls (Figure 4.1d). Although the stacking of individual nanowalls in Eu-embedded samples is quite apparent in the nanowalls with less dopant, heavier doped nanowalls appear merged together forming a thicker edge with smoother surface.

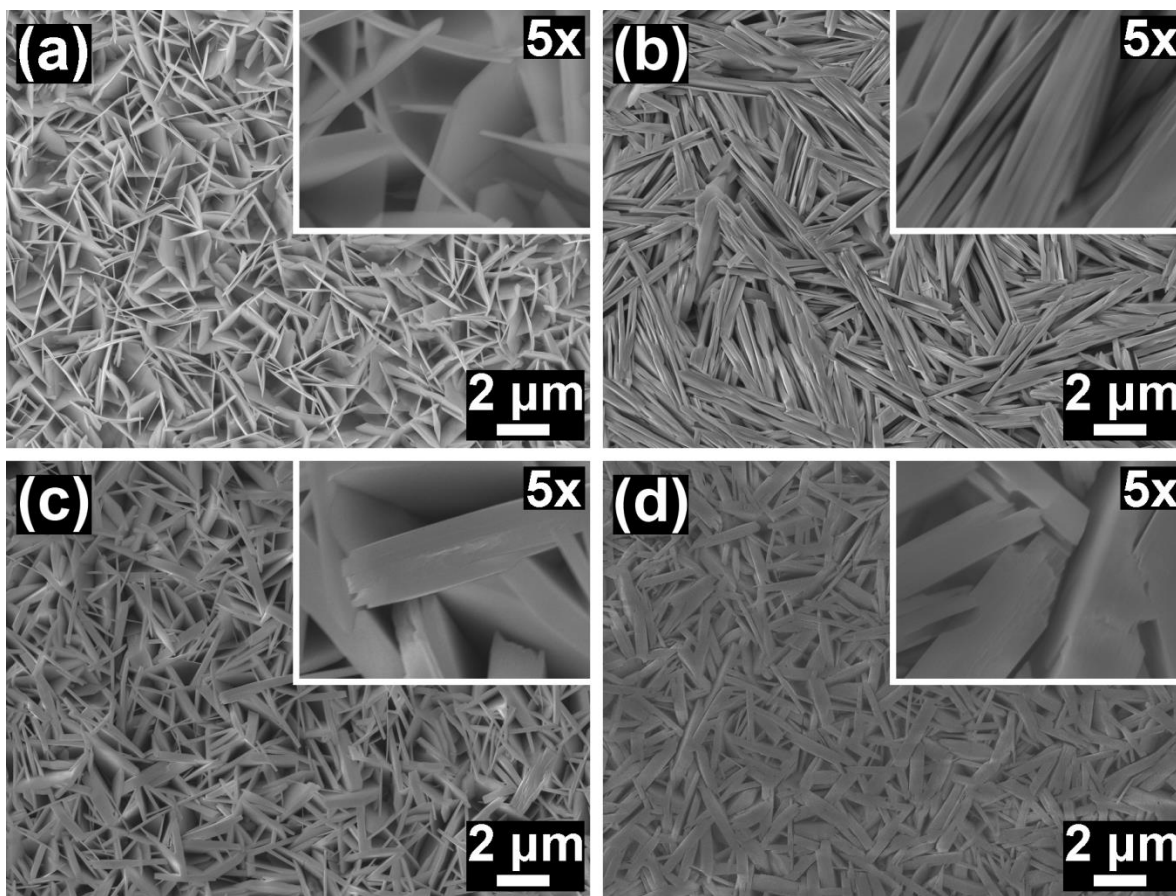


Figure 4.1 SEM images of ZnO nanowalls deposited at 70 °C on ITO-glass in (a) 0.10 M $\text{Zn}(\text{NO}_3)_2 \cdot 6\text{H}_2\text{O}$ mixed with 0.10 M KCl, and with additional (b) 0.01 M, (c) 0.05 M and (d) 0.10 M $\text{Eu}(\text{NO}_3)_3 \cdot 5\text{H}_2\text{O}$.

4.3.2 Chemical Analysis of Eu-doped ZnO Nanowalls

Figure 4.2 shows the XPS spectra, collected as a function of sputtering depth, of the Eu 3d, Zn 2p, and O 1s regions of Eu-doped ZnO nanowalls obtained in the 0.05:0.1 M Eu(III):Zn²⁺ electrolyte. For the as-prepared sample, a single broad O 1s peak at 532.9 eV is observed. With increasing Ar⁺ ion sputtering time, a new peak emerges at 531.2 eV and becomes more dominant. The O 1s peaks at 532.9 eV and 531.2 eV can be attributed to Zn(OH)₂ and/or Eu hydroxides and to ZnO, respectively. The Zn 2p_{3/2} (Zn 2p_{1/2}) peak, initially located at 1023.3 eV (1046.4 eV) before sputtering, is found to evolve into a considerably more intense peak at 1022.5 eV (1045.6 eV) upon sputtering for 500 s. We also observe a strong Eu(III) Eu 3d_{5/2} (Eu 3d_{3/2}) peak at 1135.5 eV (1165.0 eV) and a considerably weaker Eu(II) Eu 3d_{5/2} (Eu 3d_{3/2}) feature at 1126.5 eV (1156 eV).²¹⁴ This indicates that both Eu(III) and Eu(II) coexist in the ZnO nanowall structure. The relative Eu(III)/Eu(II) composition ratio is 1.8 and found to be nearly constant with increasing sputtering depth. Of special interest is the definite presence of Eu(II) even though only Eu(III) ions were used in our electrolytes. Because of the larger ionic radius of Eu(III) than that of Zn(II) and of the charge imbalance, it is less likely for Eu(III) than Eu(II) to be uniformly incorporated into ZnO matrix. It therefore appears that Eu(III) is first reduced to Eu(II) in order to alleviate the charge imbalance, thereby creating defects inside the nanowalls, during the electrodeposition.

For pristine ZnO nanowalls, Pradhan et al. demonstrated their ZnO/Zn(OH)₂ core/shell structure, along with details of the growth mechanism consistent with the XPS results of electrodeposited ZnO nanostructures.^{43,213} The observed O 1s and Zn 2p spectra for the Eu-doped ZnO nanowalls closely resemble those for undoped ZnO nanowalls reported by Pradhan et al., indicating a similar ZnO/Zn(OH)₂ core/shell structure that is likely obtained by a similar growth mechanism.

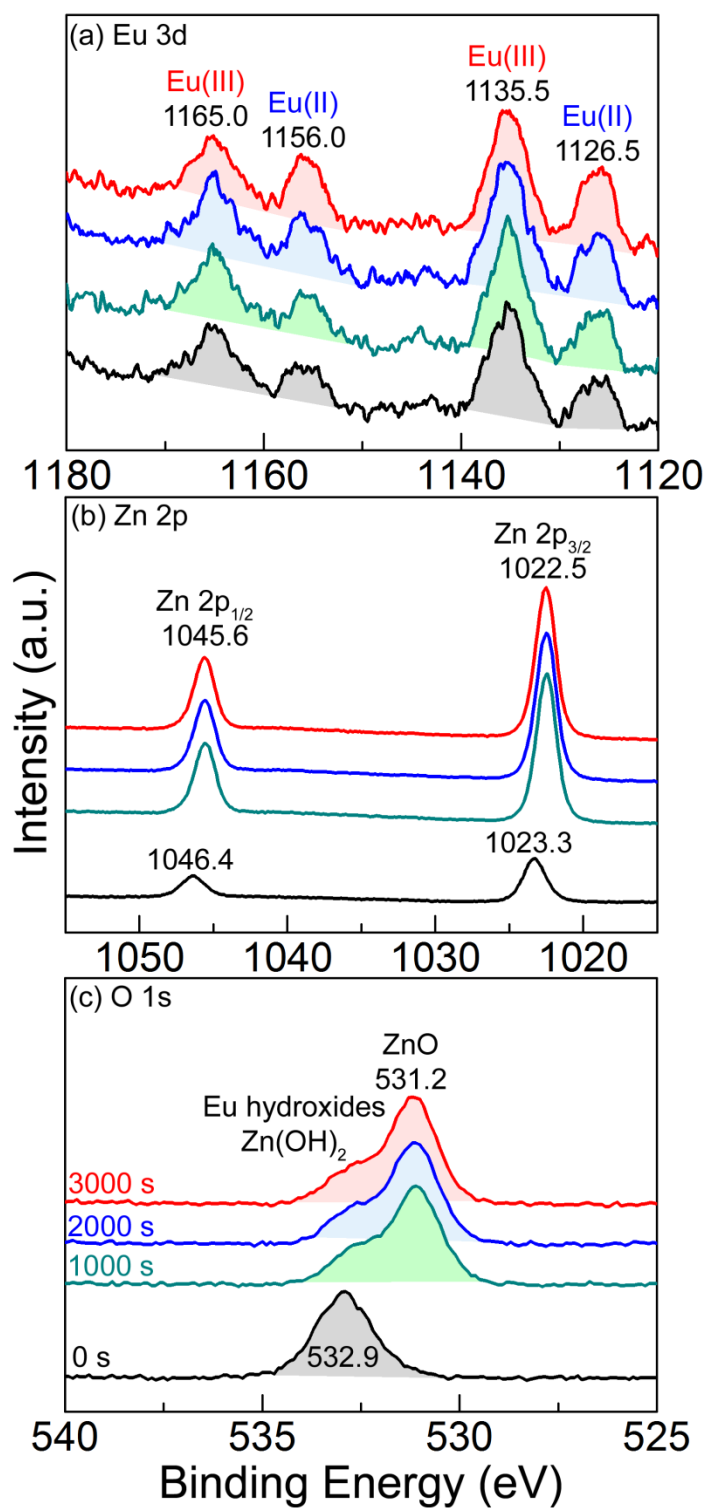


Figure 4.2 XPS spectra of (a) Eu 3d, (b) Zn 2p and (c) O 1s regions of as-deposited Eu-embedded ZnO nanowalls before sputtering and with a total sputtering time of 1000 s, 2000 s and 3000 s.

4.3.3 Photoluminescence Measurement of Eu-doped ZnO Nanowalls

The PL spectra of the ZnO nanowalls grown on ITO-glass from various concentrations of Eu(III) were also measured at room temperature. As shown in Figure 4.3, the spectral shape of the ZnO:Eu(III) nanowalls is almost independent of the Eu(III) concentration, i.e., there is virtually no difference in the spectral shapes between the undoped and the doped nanowall structures. Upon excitation by a He-Cd 325 nm line, both the undoped and doped nanowalls exhibit only one broad band in the 400–700 nm region (Figure 4.3a). The visible emission from ZnO generally originates from various intrinsic defects. For example, the green emission can be attributed to neutral and ionized oxygen vacancies, while the orange-red emission is associated with neutral and charged zinc interstitials or oxygen interstitial.^{31,208} Alternatively, the green and yellow emissions from ZnO could also correspond to the presence of OH⁻ and Zn(OH)₂ on the surface, respectively.^{211,212} The excitation spectrum of the deep-level emission illustrated in Figure 4.3a shows that the origin of the broad visible emission is the ZnO host and it confirms the electronic transitions from the valence band to the upper conduction band. The band-edge emission peak at 376 nm is therefore not likely to be produced by the as-prepared undoped and doped nanowalls upon excitation at 325 nm. These results indicate that for the nanowall structures on ITO-glass, the radiative transition from the conduction band is suppressed by the energy transfer to the upper states of the intrinsic defects. Furthermore, the sharp Eu(III) lines at 620 nm are not observed from the ZnO:Eu(III) nanowalls on ITO-glass. These results are very similar to those of ZnO:Eu(III) films grown by solution chemistry.¹⁹⁸

The formation of ionized vacancies and OH⁻ on the surface of the nanowalls from the aqueous solution is clearly seen from the XPS results (Figure 4.2). The red emission from Eu(III) would eventually be quenched by these defects. To investigate the effects of reducing the defects, we annealed the as-prepared nanowalls with 0.1 M Eu(III) concentration on ITO-glass at 300 °C for 1 h under oxygen flow. SEM study indicates that the morphology of the postannealed nanowalls on ITO-glass was not changed by the heat treatment (not shown). As shown in Figure 4.3b, the 325 nm excitation produces not only the deep-level emission band but also a strong, sharp band-edge emission band at 378 nm. Annealing also reduces the intensity of the deep-level emission by more than half, with the green emission being quenched more than the orange-red emission, which shifts the band maximum to 600 nm. This spectral change indicates that more OH⁻-related defects and the oxygen-related vacancies are removed than other intrinsic defects by thermal annealing. However, the sharp 620 nm line characteristic of Eu(III) remains absent, which suggests that the energy transfer from the ZnO host to the doped Eu(III) ion does not occur efficiently.

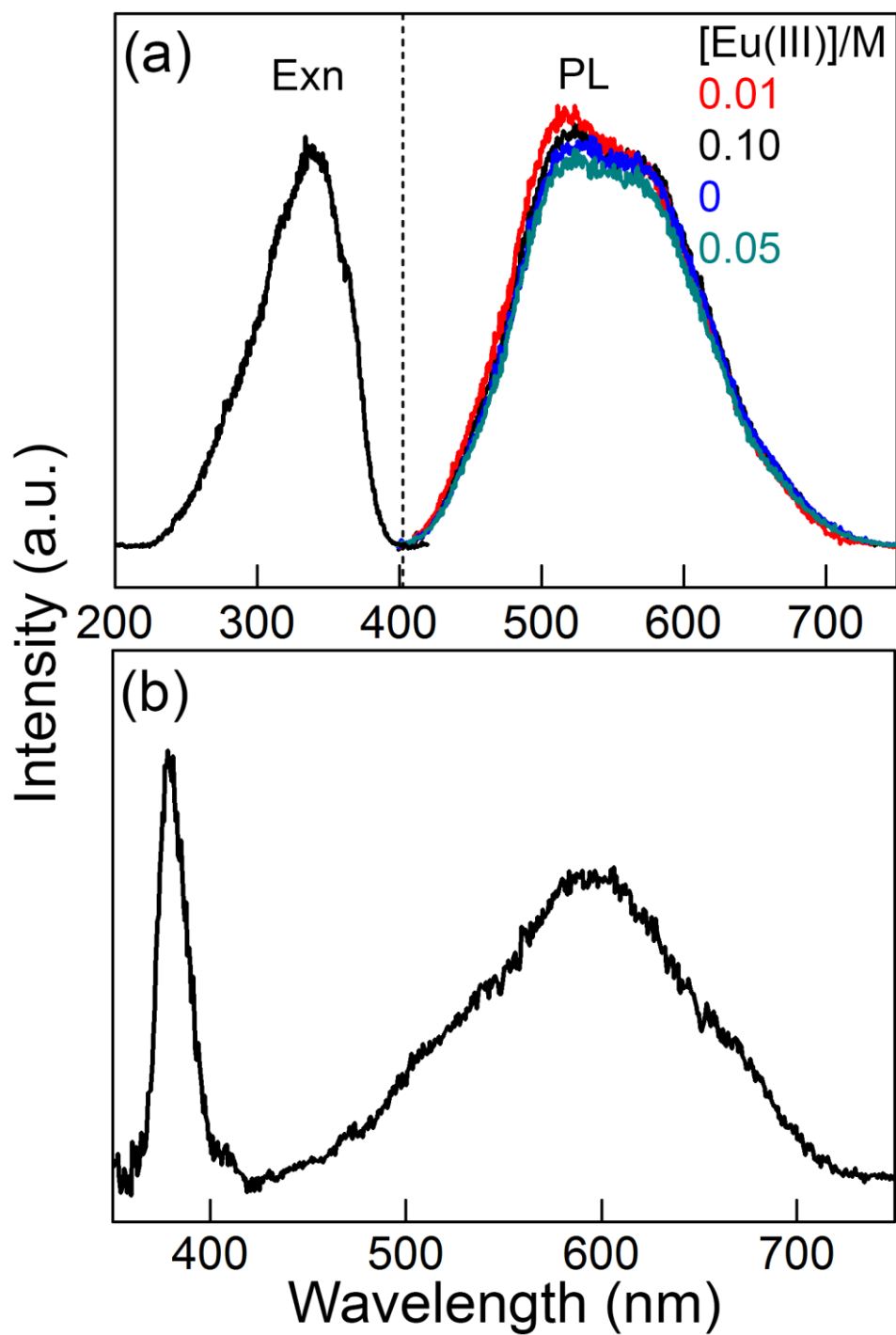


Figure 4.3 (a) PL (with $\lambda_{\text{exn}} = 325$ nm) and excitation (exn) spectra (with $\lambda_{\text{ems}} = 590$ nm) of ZnO:Eu(III) nanowalls obtained with various Eu(III) concentrations, and (b) PL (with $\lambda_{\text{exn}} = 325$ nm) spectrum of thermally treated ZnO:Eu(III) with 0.10 M Eu(III) concentration.

4.3.4 Surface Modification of Eu-doped ZnO nanowalls by 1,10-phenanthroline

As shown in XPS analysis, Eu(III) ions are also present at the surface layer, we attempted to induce the red emission from Eu(III) by modifying the ZnO:Eu(III) nanowall surface with phen. For a Eu(III) complex with phen, the sensitized emission from Eu(III) can be effectively generated by phen.^{215,216} First, the surfaces of the as-grown and the postannealed ZnO:Eu(III) nanowalls were modified by dipping them in phen with three different concentrations (0.010, 0.050 and 0.10 M) in CH₂Cl₂ for 30 s. then PL with excitation wavelength of 325 nm were then measured. Evidently, surface-functionalization with 0.010 M solution of phen has no effect on the PL spectrum for the as-grown ZnO:Eu(III) nanowalls (Figure 4.4a). In contrast, the same treatment for the postannealed ZnO:Eu(III) nanowalls results in a sharp red emission band from Eu(III) at 620 nm, as shown in Figure 4.4c. Except for the emergence of this sharp 620 nm red emission and the slight intensity reduction for the band-edge emission at 376 nm, the spectral shape of the phen-treated nanowalls (Figure 4.4c) is almost the same as the postannealed nanowalls without the phen treatment (Figure 4.4b). The appearance of the 620 nm peak indicates that the Eu(III) ions on the surface layer are coordinated to phen, and the coordinated phen molecules trigger an energy transfer process to Eu(III) ions, which produces the red emission. When treated with a higher phen concentration of 0.050 M (Figure 4.4d), the blue-green emission becomes discernibly more intense. For treatment with an even higher phen concentration of 0.10 M (Figure 4.4e), spectral intensity above 480 nm has been significantly reduced relative to that functionalized with 0.05 M phen, with the blue-green emission becoming stronger than the 600 nm emission. The band-edge emission at 376 nm has also been quenched significantly. For comparison, PL and excitation spectra of an Eu-phen complex, [Eu(phen)₂](NO₃)₃, were taken and are shown in Figure 4.5. Its excitation spectrum (Figure 4.5) clearly does not match with the excitation spectrum of the Eu-doped ZnO nanowalls (Figure 4.3).

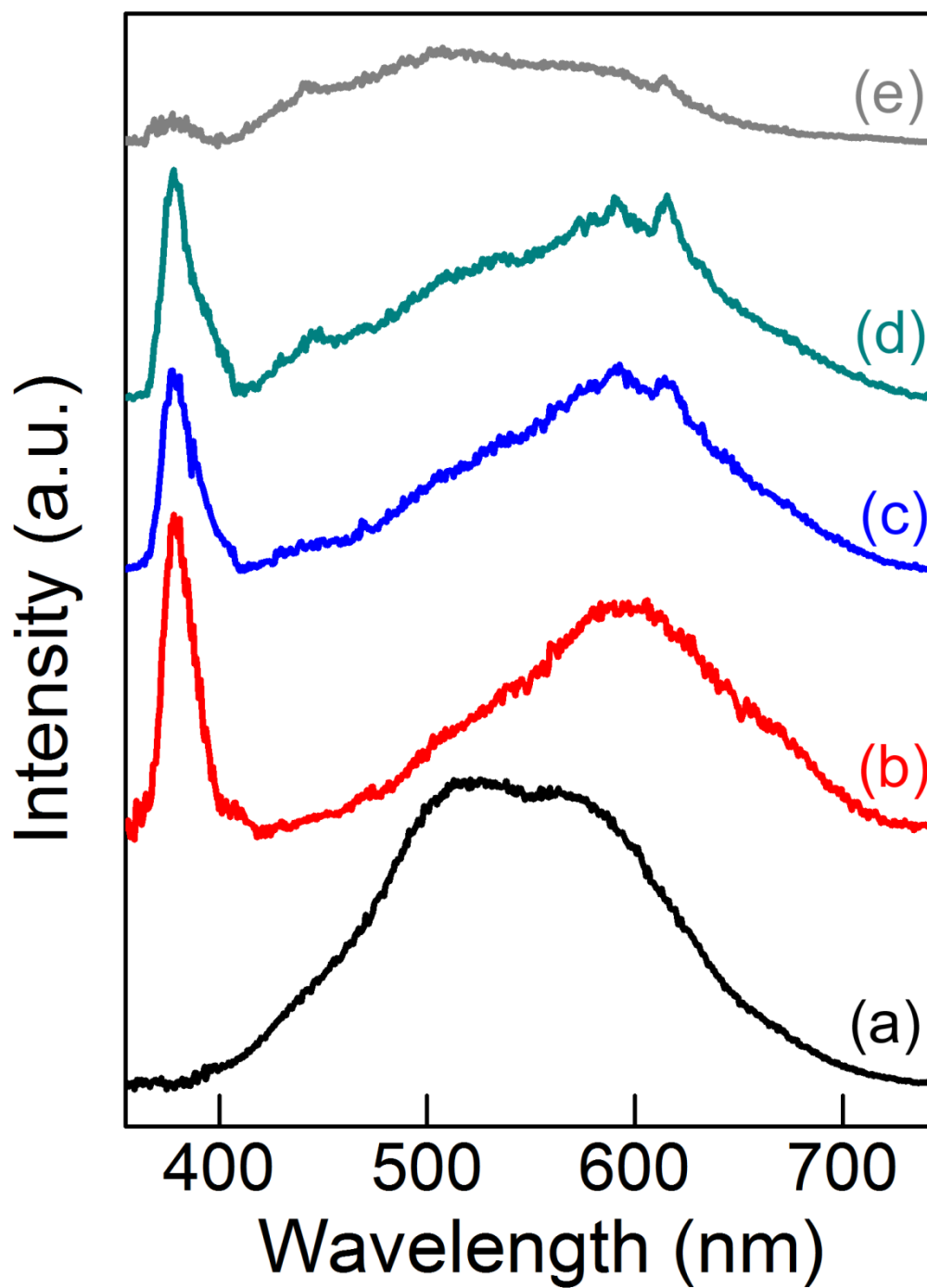


Figure 4.4 PL spectra ($\lambda_{\text{exn}} = 325$ nm) of (a) as-grown ZnO:Eu(III) nanowalls sample surface-functionalized with 0.010 M phen, and annealed samples surface-functionalized (b) without and with (c) 0.010 M, (d) 0.050 M and (e) 0.10 M of phen.

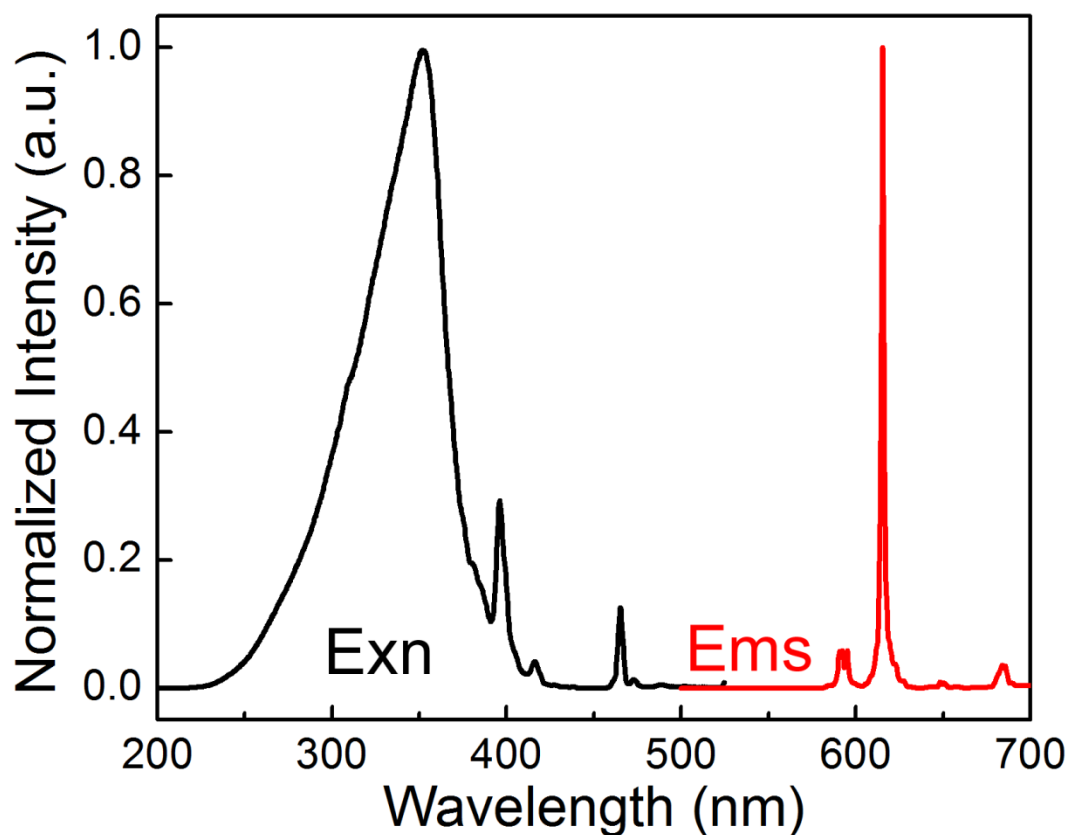


Figure 4.5 PL ($\lambda_{\text{exn}} = 325 \text{ nm}$) and excitation (exn) spectra ($\lambda_{\text{ems}} = 614 \text{ nm}$) of $[\text{Eu}(\text{phen})_2] \cdot (\text{NO}_3)_3$.

To investigate the energy transfer pathway and the origin of the blue-green emission enhancement, we also modified the surface of the annealed nanowalls by ethylenediamine (en), which has two nitrogen atoms similar to phen. En acts as a bidentate ligand to form a complex with Eu(III), but en is non-luminescent. Figure 4.6 shows the PL spectra of the postannealed ZnO:Eu(III) nanowalls on ITO-glass without and with en surface-functionalization. Evidently, the nanowalls treated with 0.01 M of en in CH_2Cl_2 do not exhibit the sharp feature at 620 nm, in marked contrast to the phen surface-functionalization. The blue-green emission between 450 nm and 550 nm becomes more intense, as similarly found for the case with the phen treatment at a higher concentration. Together with Figure 4.4, these results therefore suggest that the emission from Eu(III) could be strongly related to the energy-transfer process from a coordinated molecule, such as phen. In addition, the enhancement of the blue and green emissions could be attributed to newly formed defects, such as Zn^{2+} -N complex, on the surface of the nanowalls.

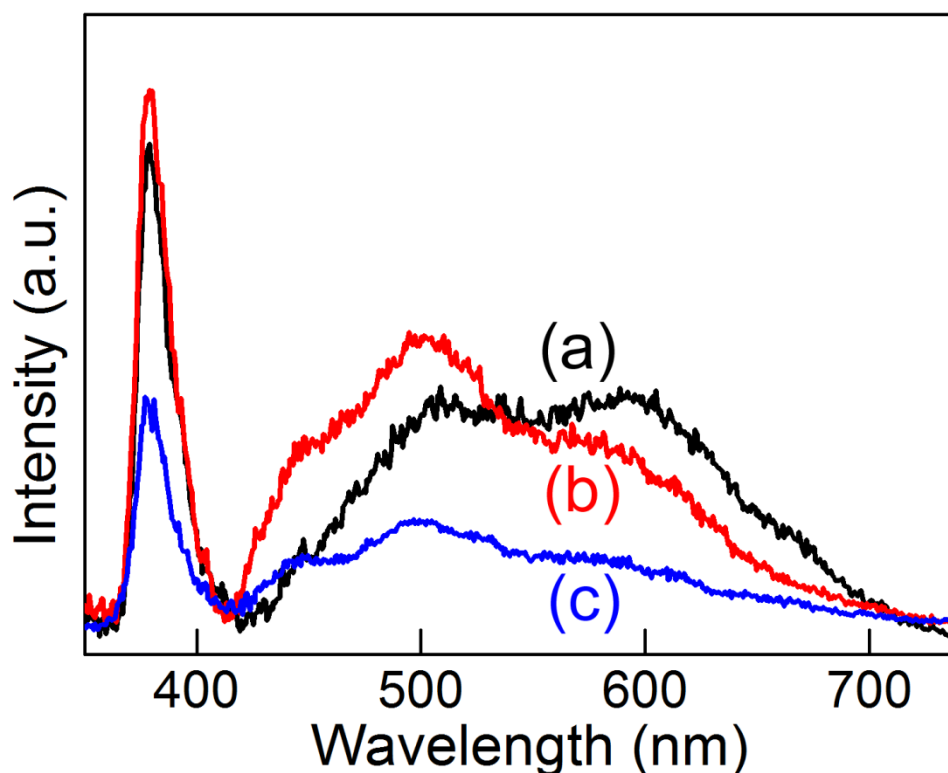


Figure 4.6 PL spectra (with $\lambda_{\text{exn}} = 325$ nm) of postannealed ZnO:Eu(III) nanowalls (a) without and with surface-functionalization of (b) 0.01 M and (c) 0.1 M of ethylenediamine.

4.3.5 Cascade Energy Transfer Mechanism

These observations suggest that phen adsorbed on the surface of the ZnO:Eu(III) nanowalls could play two important roles in the energy transfer mechanism from ZnO (as the energy donor) to Eu(III) (as the energy acceptor). Phen is potentially a good acceptor, because its absorption band overlaps well with the band-edge emission band. To account for our observation, we propose a model (shown schematically in Figure 4.7) for the red emission from Eu(III) involving two consecutive energy-transfer processes, i.e. from ZnO to Eu(III) via phen. As shown in Figure 4.8, the cascade energy transfer begins with excitation of ZnO from the valence band (VB) to the upper levels in the conduction band, and this is followed by the subsequent relaxation from the upper levels to the lowest level in the conduction band (LCB). Without surface modification of the ZnO:Eu(III) nanowalls by phen, the two possible processes originating from LCB are the radiative decay to VB and the energy transfer to upper levels of the intrinsic defects (such as OH^- , oxygen vacancy V_{O} , zinc vacancy V_{Zn} ,

and oxygen interstitials O_i), which result in the band-edge and deep-level (defect-related) emissions, respectively (Figure 4.8a). When the surface of the nanowalls is treated with phen of a sufficiently low concentration (Figure 4.8b), a competitive process involving energy transfer from LCB to the excited singlet state of phen also occurs. Furthermore, following the subsequent intersystem crossing from the singlet excited state ($^1S^*$) to its triplet state ($^3T^*$) in phen, the energy of the excited triplet state of phen is transferred to the near resonant states of Eu(III) (5D_2 , 5D_1), because the energy transfer directly from the singlet state of phen to the Eu(III) states is less efficient.

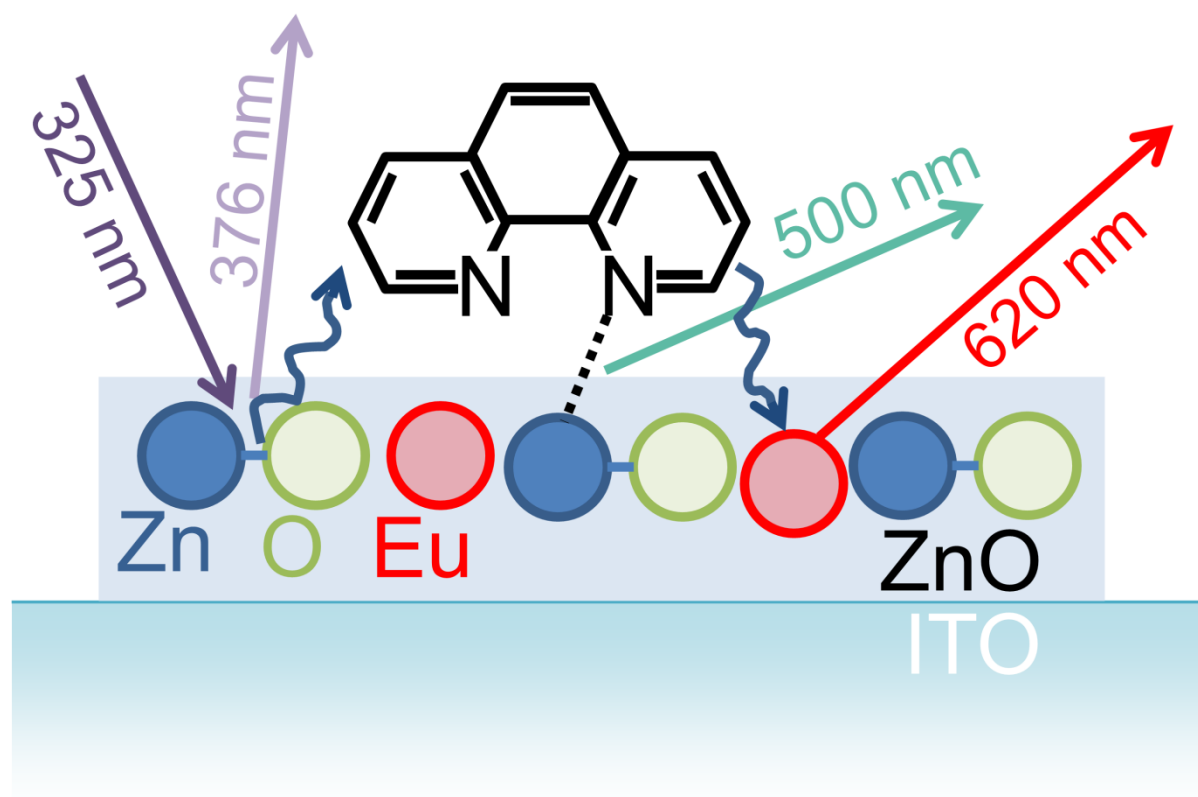


Figure 4.7 A schematic model for the cascade energy transfer of phen-modified ZnO:Eu(III) nanowalls.

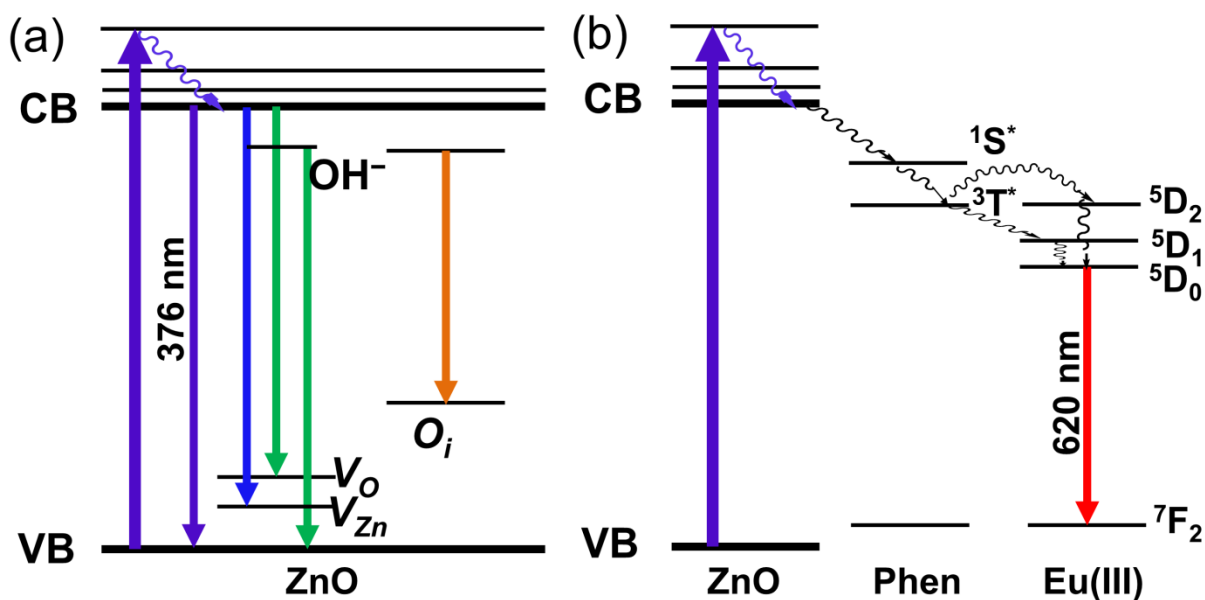


Figure 4.8 Energy level diagrams for (a) annealed ZnO:Eu(III) nanowalls and (b) the cascade energy transfer mechanism in the phen-modified ZnO:Eu(III) nanowalls.

The energy transfer processes from an excited state of a ligand to a rare earth ion in the solid state have been described in the exchange interaction theory by Dexter.¹⁰² In Dexter's model, the energy transfer rate is given by $\exp(-2R)$, where R is the separation between a donor phen and an acceptor Eu(III). When the proximate distance is very close to the Eu-to-N bond distance (2.60 \AA), energy transfer from phen to Eu(III) could take place very effectively.²¹⁵ If the Eu-to-N separation is increased by twice the proximate distance, the energy transfer probability would decrease by more than an order of magnitude. When ZnO:Eu(III) nanowalls are treated with a sufficiently low concentration of phen (below 0.050 M, Figure 4.4c), the phen molecules located within the proximate range of Eu(III) ions provide a preferred path in the optical de-excitation process of the nanowalls, and the cascade energy transfer process (from Eu(III) to phen to ZnO) would take place efficiently. When the concentration of phen is increased to 0.050 M (Figure 4.4d), some phen molecules would bind to Zn^{2+} at long distance, which would contribute to additional blue-green emission. However, the overall intensity except the blue-green region is greatly reduced for 0.1 M phen (Figure 4.4e). Since phen is saturated in the proximate distance range of Eu(III), the additional phen molecules are anticipated to bind to Zn^{2+} and are not able to enhance the probability of cascade energy transfer from

ZnO to Eu(III). Furthermore, the additional phen molecules appear to crunch the intensity of the overall spectrum.

4.4 Summary

We have successfully embedded Eu into ZnO nanowall structures by using a single-step electrochemical deposition method. Our SEM data show that ZnO nanowalls have become thicker and stacked upon doping with Eu. Our O 1s and Zn 2p XPS results further reveal a ZnO-Zn(OH)₂ core-shell structure for the Eu-embedded ZnO nanowalls, similar to that of the pristine ZnO nanowall structure. Eu is found to be uniformly embedded in the ZnO-Zn(OH)₂ core-shell nanostructure, as supported by the nearly uniform Eu 3d intensity with increasing Ar⁺ sputtering depth. The PL spectral features of the as-grown Eu-embedded ZnO nanowalls are observed to be independent of the Eu(III) concentration. Annealing the ZnO:Eu(III) nanowall samples yields band-edge emission, while surface modification of the samples by phen generates an additional sharp Eu(III) emission at 620 nm. These results show that the energy transfer from ZnO to Eu(III) appears to be extremely weak without phen, and they provide strong support for our proposed cascade energy transfer model. Our findings and the cascade energy transfer model could be extended to provide further insight into rare earth transition metal-doped ZnO systems prepared by other embedment process.

Chapter 5

Extraordinary Enhanced Emission of Terbium-doped ZnO Nanowalls and Rhodamine B Detection by Cascade Energy Transfer

5.1 Introduction

ZnO nanostructures have received great interest for applications in the fields of optoelectronics, piezotronics, spintronics and photocatalysis, because of its wide band gap (3.37 eV) and large exciton binding energy (~60 meV).^{158,217–221} ZnO nanostructures exhibit two emission bands: a sharp deep UV emission associated with the excitonic band edge, and a broad visible emission attributable to various intrinsic defects.^{31,208,210} These unique optical properties have made ZnO nanostructures one of the most promising materials for the next-generation optoelectronic devices operating in the UV or visible region.^{222,223}

Doping of trivalent rare earth (RE) transition metal ions into ZnO nanostructures has been conducted with the goal to improve their intrinsic physical properties, such as optical, electronic, and magnetic properties.^{224–227} They are particularly attractive for potential application in visible optoelectronics, because of their unique luminescence properties, such as hypersensitivity to the environment, narrow bandwidth, and long lifetime in the millisecond range.^{226,227} Among the RE(III) ions, europium and terbium are found to emit red and green luminescence, respectively. To date, most studies have focused on Eu(III)-doped ZnO nanostructures.^{177,227,228} Because the advantage in the optical application of RE³⁺-doped ZnO nanostructures originates from the energy transfer from ZnO to RE(III), Eu(III) is less effective than Tb(III) due to the larger difference between the conduction band minimum of ZnO and the emitting level for Eu(III) (⁵D₀) than that for Tb(III) (⁵D₄). Recently, nanostructured Tb(III)-doped ZnO (ZnO:Tb(III)) materials such as nanorods, nanoparticles, nanocrystals, and microspheres have been prepared by various methods including electrochemical deposition, sol-gel and hydrothermal syntheses.^{134,226,229,230} The resulting ZnO:Tb(III) nanostructures, however, produced very weak lines as no or only trace characteristic emission originated from Tb(III) was observed. The low emission intensities did not improve even with additional postannealing of the ZnO:Tb(III) nanostructures.

In this study, ZnO:Tb(III) nanowalls were electrochemically grown on indium-tin oxide (ITO) coated glass. Upon excited by UV light, the as-grown ZnO:Tb(III) nanowalls were found to produce a series of sharp lines superpositioned on the green emission from the intrinsic defects. The photophysical properties of these ZnO:Tb(III) nanowalls on an ITO-glass substrate were characterized in detail. We also investigated how the photoluminescence (PL) properties of these ZnO:Tb(III) nanowalls were affected by surface modification with noble metal nanoparticles (NPs) and organic chromophores. To date, the PL enhancement of ZnO due to localized surface plasmon resonances (LSPRs) of metal nanoparticles has been realized only from ZnO films treated with metal NPs involving elaborate, complex fabrication methods, such as electron-beam lithography, ion implantation and atomic layer deposition.^{231–233} In contrast, ZnO nanorods and nanocrystals treated with simple surface-modification by metal NPs have thus far not been found to exhibit LSPR in the UV and visible luminescence.^{234–236} Here, we deposited NPs of noble metals (Ag, Pt and Au) of a few nanometers in size by a simple dip-casting method, and demonstrated the remarkable enhancement of the Tb(III) green emission by Ag NPs. In addition, the feasibility of using the Tb-related green emission as a fluorescence probe was examined by surface modification using appropriate organic materials. Rhodamine B (RhB) was selected as a model chromophore that absorbs the green light. RhB produces moderate fluorescence intensity in ethanol or aqueous solutions, while its fluorescence intensity is very weak to none in the powder form or in thin film drop-casted on the substrate. In this work, the RhB/ZnO:Tb(III)-nanowall heterostructures exhibit substantial emission in the orange-red region, demonstrating its potential use as a fluorescence-based chemosensor for the first time.^{237–239}

5.2 Experimental Details

5.2.1 Chemicals

Zinc nitrate hexahydrate ($\geq 98\%$), potassium chloride ($\geq 99.0\%$), terbium nitrate pentahydrate (99.9%), rhodamine B ($\geq 95\%$), and dichloromethane ($\geq 99.9\%$) were purchased from Sigma-Aldrich and used without further purification.

5.2.2 Fabrication of Terbium-Doped ZnO Nanowalls

Undoped and Tb-doped ZnO nanowalls were synthesized using a method described in detail elsewhere.²²⁷ In a three-electrode electrochemical cell, potentiostatic amperometry at -1.4 V vs Ag/AgCl was used to deposit undoped and Tb-doped ZnO nanowalls on ITO-glass used as the working electrode, in an aqueous solution of 0.1 M $\text{Zn}(\text{NO}_3)_2 \cdot 6\text{H}_2\text{O}$ and 0.1 M KCl mixed with 1

mM to 10 mM terbium nitrate pentahydrate. Deposition was maintained at a constant temperature of 80 °C by using a water bath.

5.2.3 Use of Noble Metal Nanoparticles for Localized Surface Plasmon Resonances

Pt NPs (~3 nm dia.) dispersed in water and Au NPs (~5 nm dia.) stabilized by phosphate buffered solution (PBS) were purchased from Sigma-Aldrich. Ag NPs (~4.5 nm dia.) dispersed in cyclohexane were synthesized from a mixture of silver nitrate, hydrazine and 2-ethylhexyl hydrogen 2-ethylhexyl phosphonate (used as a stabilizer) according to a previous method.²⁴⁰ The final concentration of the dispersed NPs was adjusted to be 25 μ M by diluting with an appropriate solvent: cyclohexane for Ag NPs, and water for Pt and Au NPs. The NPs were then deposited by immersing the ZnO nanowall samples in the NP-dispersed solution for 10 s. After drying in air, the dip-casting treatment of the nanowalls with the diluted NP-dispersed solution could be repeated as required.

5.2.4 Surface Modification by Rhodamine B

A 10 mM solution of RhB was prepared by using CH_2Cl_2 . A small drop of the RhB solution was applied to the ZnO:Tb(III) nanowalls on ITO-glass, followed by drying in air. After each PL measurement, additional application of RhB drops was made, as required.

5.2.5 Sample Characterization and Spectroscopic Measurements

The morphologies of Tb-doped ZnO nanowalls were examined by field-emission scanning electron microscopy (SEM) in a Zeiss Merlin microscope. Structural and chemical-state composition analyses of the sample were performed by transmission electron microscopy (TEM) in a Zeiss Libra 200MC microscope and X-ray photoelectron spectroscopy (XPS) in a Thermo-VG Scientific ESCALab 250 microprobe, respectively. Scanning Auger microscopy (SAM) was conducted in a Thermo-VG Scientific Microlab 350 microprobe to provide surface elemental composition analysis.

PL spectrum was measured at 90° with an ARC 0.5 m Czerny–Turner monochromator equipped with a cooled Hamamatsu R-933-14 photomultiplier tube, using a 325 nm He-Cd laser as the excitation source. For low-temperature excitation spectral measurement, the sample was placed on the cold finger of a closed cycle liquid helium refrigerator (CCS-120). The sample was irradiated with the light from an Oriel 1000 W Xe lamp (with a working power of 600 W) passing through an Oriel MS257 monochromator to obtain the excitation spectrum.

5.3 Results and Discussion

5.3.1 Morphologies, Chemical Composition and Structural Analysis of Terbium-doped ZnO Nanowalls

The SEM images of pristine and Tb-doped ZnO nanowalls obtained with various Tb(III) concentrations are shown in Figure 5.1. Undoped ZnO nanowalls appear to be 100 to 200 nm thick (Figure 5.1a). Although the thickness of (Tb-doped) ZnO nanowalls has not changed upon introduction of Tb(III), the surface of the nanowalls has evidently become smoother (Figures 5.1b, 5.1c). As the concentration of Tb(III) reaches 10 mM, the nanowalls tend to stack together to form thicker nanowalls (with average thickness of 700-800 nm) and nanowalls with different thicknesses are observed (Figure 5.1d).

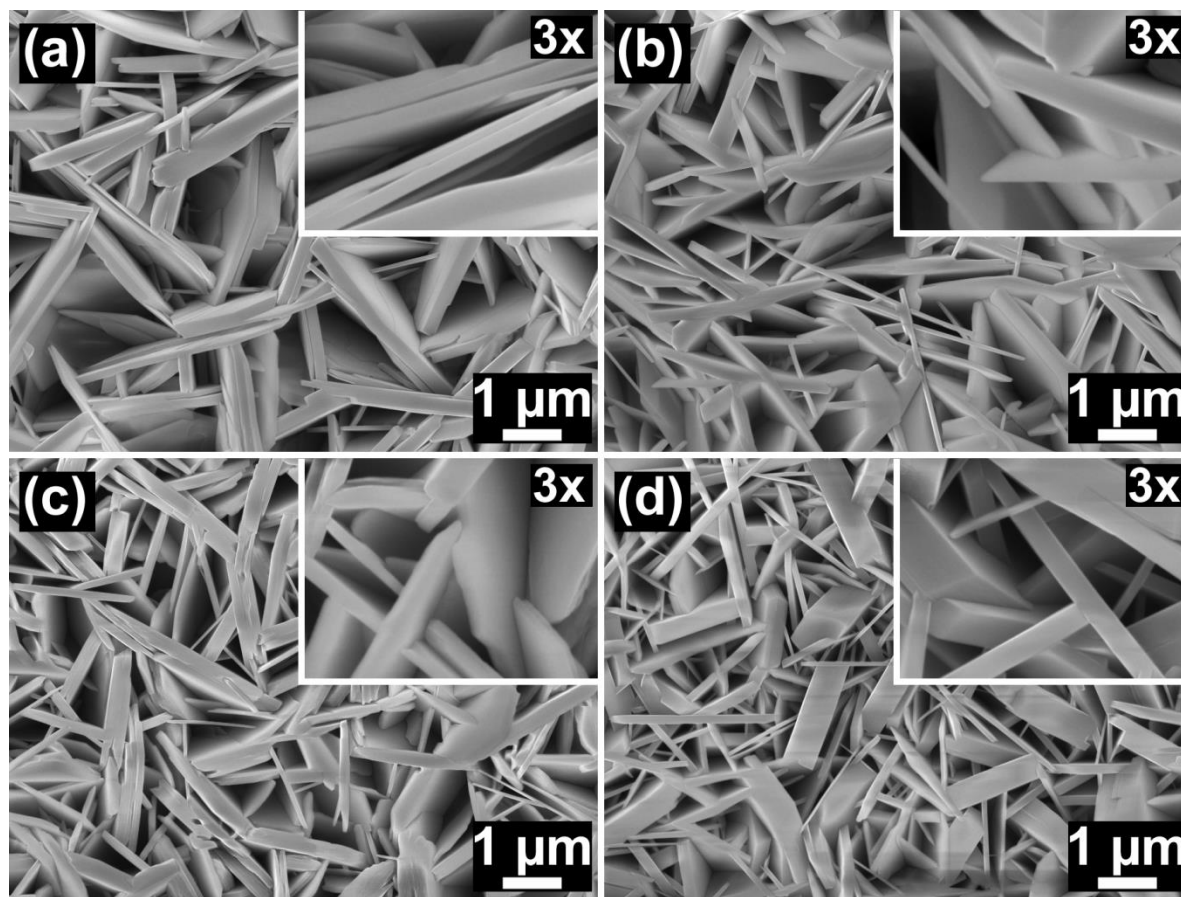


Figure 5.1 SEM image of (a) pristine ZnO nanowalls and Tb-doped ZnO nanowalls obtained with Tb(III) concentrations of (b) 1 mM, (c) 5 mM and (d) 10 mM.

To confirm the uniformity of Tb(III) ion distribution in the ZnO nanowalls, composition analysis by SAM and XPS as a function of Ar⁺ ion sputtering depth has been performed. Since the SAM system employs an electron beam with a small beam spot and is capable of a high spatial resolution of ~20 nm, we collect Auger electron spectra at three well-separated locations of the nanowall sample as marked on the SEM image (Figure 5.2a). Due to the small amount of trivalent Tb cation dopants, we have removed the spectral background to better expose the Tb peaks. Evidently, the near identical Tb MNN Auger intensities found at three different sites confirm that the Tb(III) dopant surface composition is independent of the size of the nanowalls and it appears uniform for the entire sample.²⁴¹ Figures 5.2c and 5.2d show the XPS spectra of the Tb 3d and O 1s regions, respectively. Both position and intensity of the Tb 3d_{5/2} (3d_{3/2}) peak found at 1242.4 eV (1277.5 eV) remain unchanged with Ar⁺ sputtering, which indicates excellent doping uniformity of Tb(III) throughout the ZnO nanowalls. The broad O 1s peak at 532.9 eV can be attributed to Zn(OH)₂ and/or Tb hydroxides on the surface of the nanowalls for the as-grown sample. Upon Ar⁺ sputtering, a new peak at 531.2 eV corresponding to ZnO emerges and it becomes more prominent. The spectral evolution of the observed O 1s spectra confirms that the ZnO:Tb(III) nanowalls follow the well-known growth mechanism of electrochemically deposited ZnO nanostructures.⁴³ Figure 5.3 shows the TEM image of a ZnO:Tb(III) nanowall sample obtained with Tb(III) concentration of 10 mM. The corresponding high-resolution TEM image (Figure 5.3, inset) reveals a lattice spacing of 2.8 Å, in good accord with the interplanar spacing of ZnO (100) planes.

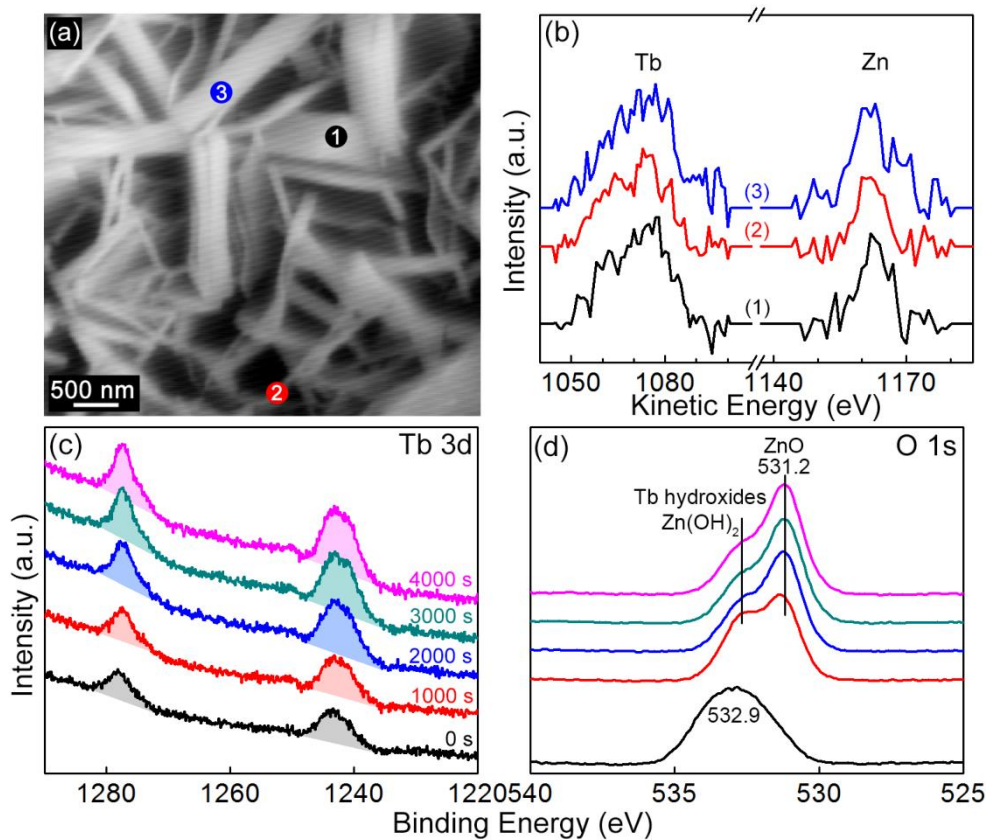


Figure 5.2 (a) SEM image and (b) background-subtracted Auger electron spectra of three different locations marked in (a) for as-deposited Tb-doped ZnO nanowalls obtained with Tb(III) concentration of 10 mM. XPS spectra of (c) Tb 3d and (d) O 1s regions for as-grown Tb-doped ZnO nanowalls and upon sputtering for 1000 s, 2000 s, 3000 s, and 4000 s.

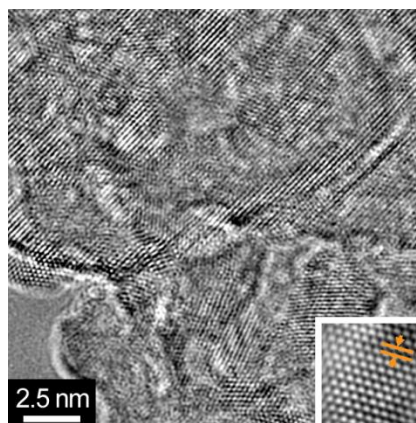


Figure 5.3 TEM and HRTEM (inset) images of Tb-doped ZnO nanowalls obtained with Tb(III) concentration of 10 mM.

5.3.2 Photophysical Properties of Terbium-Doped ZnO Nanowalls

Figure 5.4a shows the PL spectra of ZnO:Tb(III) nanowalls on ITO-glass obtained in electrolytes with three different Tb(III) molar concentrations. For nanowalls grown from the electrolyte with 1 mM Tb(III) solution, excitation at 325 nm produces the characteristic emission from the as-grown ZnO nanostructures, with the near-band-gap emission peak at 375 nm and the broad defect-related emission band spanning over the visible region. No additional bands arisen from the Tb(III) dopants are observed from these nanowalls. However, the PL spectrum for doped nanowalls grown with the electrolyte containing 5 mM Tb(III) solution exhibits additional well-defined sharp peaks in the green region superpositioned on the defect-related broad band. When the Tb(III) concentration reaches 10 mM, the sharp characteristic emission lines from Tb(III) evidently appear with the barycenters at 489, 545, 582 and 621 nm. These bands correspond to the transitions from the 5D_4 state to the $^7F_{6,5,4,3}$ states, respectively.

Among these emission lines, the $^5D_4 \rightarrow ^7F_5$ transition at 545 nm corresponds to the most intense luminescence and it exhibits a series of sharp features, as evidenced from the splitting arising from the $(2J+1)$ degeneracy. The excitation spectrum for the 545 nm emission has been measured at several temperatures. Figure 5.4b shows that, except for the intensity increasing inversely with the temperature, there is generally no significant difference in the band structure. The band maximum position for the room-temperature spectrum appears to be slightly red-shifted compared to those for the spectra measured at lower temperatures. The broad band with band maximum at 355 nm and no sharp feature spanning over the 300-380 nm region in these lower-temperature spectra is very similar to those of the near-band-gap emission from ZnO nanowalls (Figure 5.4a). In general, direct excitation for the 545 nm emission from Tb(III) is expected to produce a series of sharp lines with moderate intensities in the 300-400 nm region, corresponding to the transitions from the 5F_6 state to the $^5G_{6,5}$, and the $^5L_{10,9}$ states.⁸⁰ As these lines are evidently not observed in the broad excitation band, this indicates that the emission from Tb(III) can only be realized by energy transfer from ZnO.

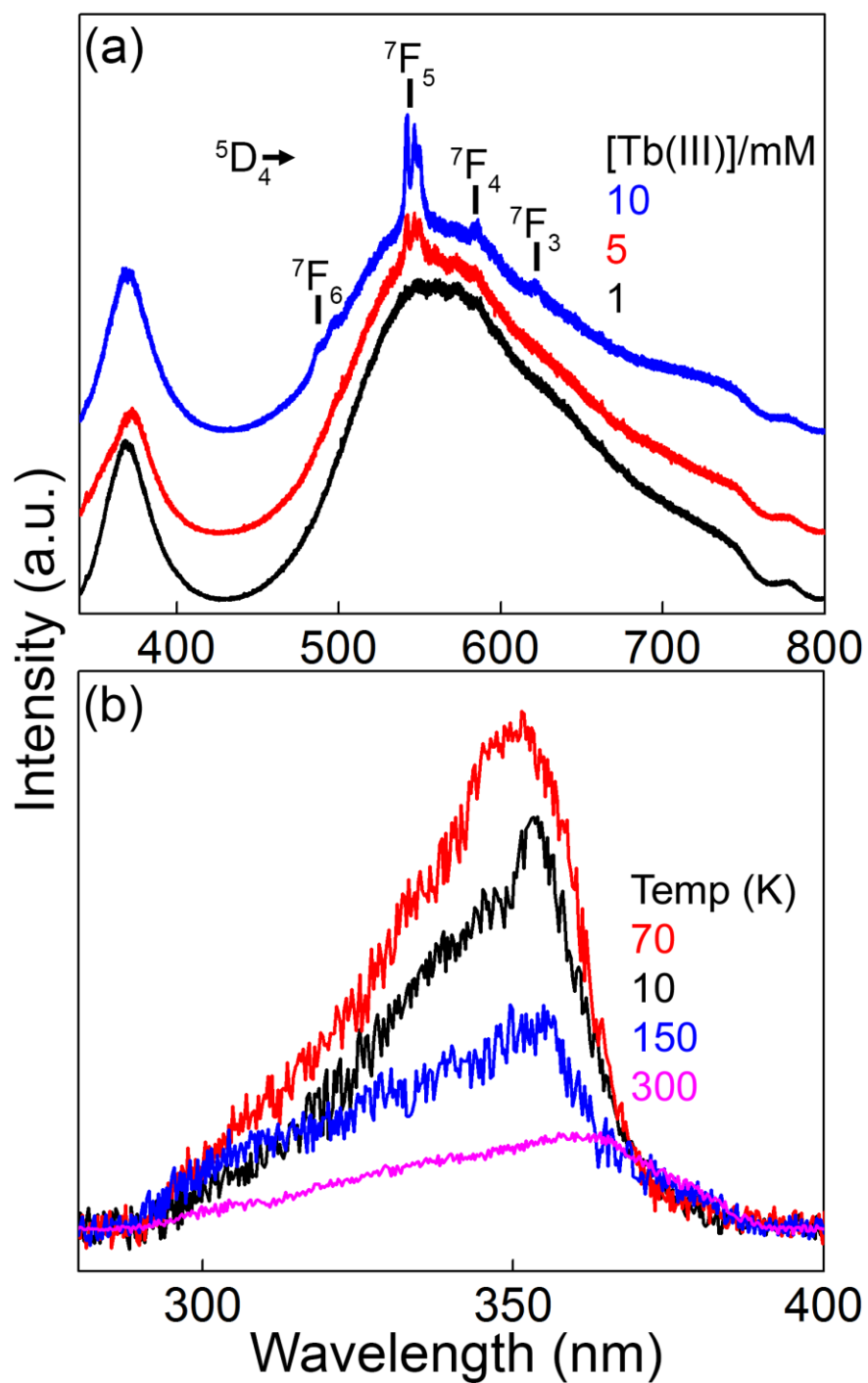


Figure 5.4 (a) PL spectra ($\lambda_{\text{exc}} = 325$ nm) of Tb-doped ZnO nanowalls obtained in electrolyte of Zn^{2+} concentration of 0.1 M and with 1 mM, 5 mM and 10 mM Tb(III) concentration, and (b) excitation spectra ($\lambda_{\text{ems}} = 545$ nm) of the Tb-doped ZnO nanowalls obtained with 10 mM Tb(III) concentration measured at 10, 70, 150 and 300 K.

The time profiles of the emission decay from ZnO:Tb(III) nanowalls obtained with 10 mM Tb(III) concentration have been measured in order to examine details of the energy-transfer dynamics. The lifetime (τ) of the ZnO band-edge emission has been found to be highly dependent on its morphology: $\tau = 112$ ps for the bulk single-crystal sample, $\tau = 37$ ps for the nanosphere, and $\tau = 8$ ps for the nanowire.²⁴² The lifetime of the observed visible emission ($\tau \approx 4.5$ ps) is much shorter than any of the reported band-edge emissions of ZnO nanostructures. Figure 5.5a shows the time profiles of the PL intensities of the visible emission at $\lambda_{\text{ems}} = 535, 545, 560$ and 600 nm from the ZnO:Tb(III) nanowalls pumped by a 337 nm N₂ laser with a 0.03 ms pulse-width. The time profile of the 545 nm emission is discernibly different from those of the other emissions, with the decay of the 545 nm emission being notably slower (i.e. larger τ) than those of the others. Assuming that the lifetime of the visible emission from the defects is in the picosecond range, the wavelength-independent time profiles (i.e. those obtained with $\lambda_{\text{ems}} = 535, 560$ and 600 nm) should be originated from the scattered light of the excitation laser, the decay lifetime of which has been estimated to be $\tau_{\text{scatt}} = 67.4$ μs . The observed time evolution intensity of the 545 nm emission can therefore be considered to consist of two decay components: one for the scattered light and one for the emission from Tb(III). As shown in Figure 5.5b, the time profile can indeed be fitted with two exponential components of $\tau_{\text{scatt}} = 67.4$ μs (87%) and $\tau_{\text{Tb}} = 150$ μs (11%), with excellent $R^2 > 0.999$. The quantum yield of the sensitized luminescence of Tb(III) can be estimated by using the relationship between the observed lifetime of Tb(III) (τ_{Tb}) and its natural lifetime (τ_0).²⁴³ Using the reported value of τ_0 of 4.75 ms for Tb(III), we obtain a quantum yield for the sensitized emission from Tb(III) to be $\Phi_{\text{sens}}^{\text{Tb}} = 0.032$.²⁴³

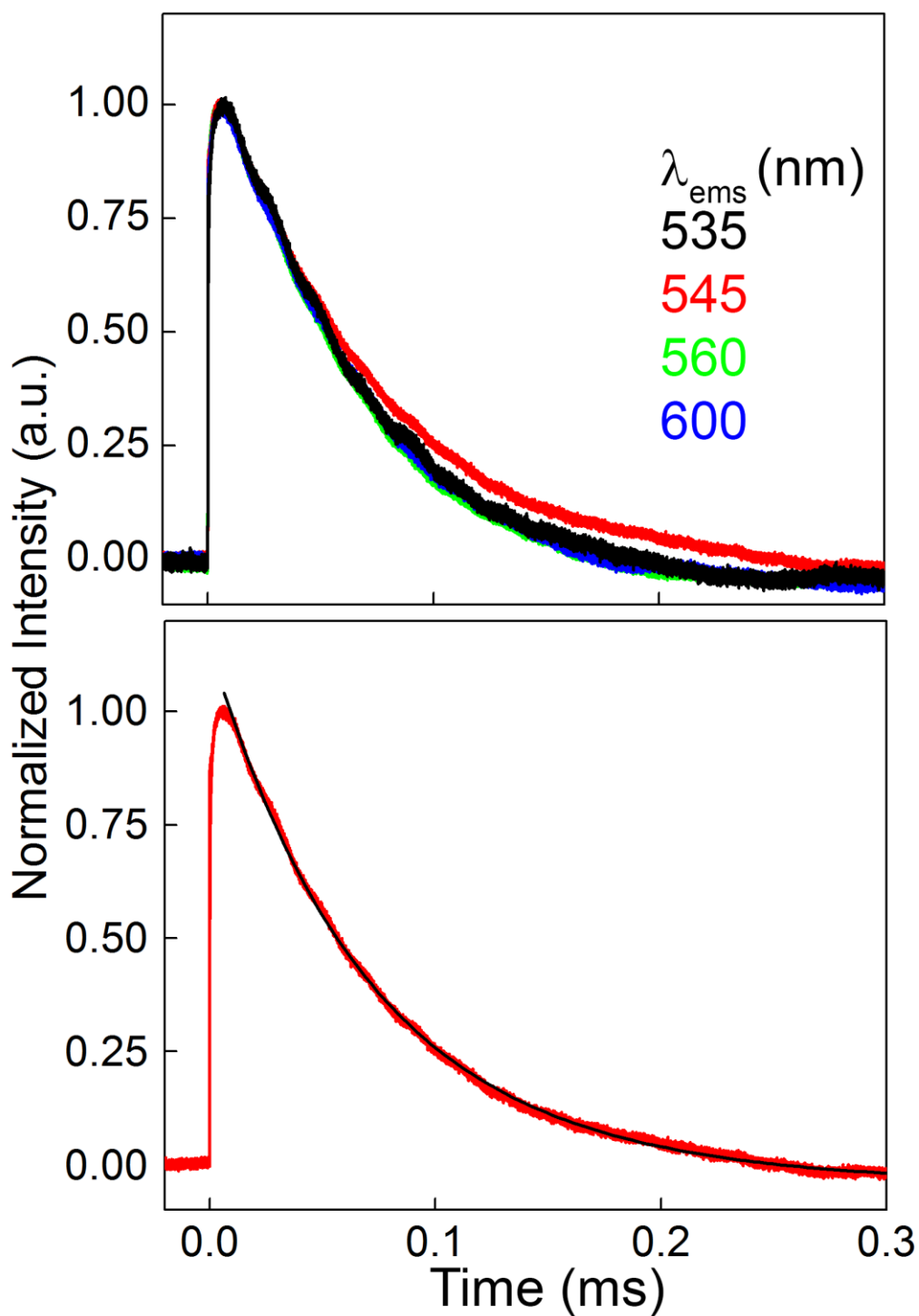


Figure 5.5 (a) Time profiles of the visible emissions ($\lambda_{\text{exn}} = 337.1$ nm) at 535, 545, 560, and 600 nm from Tb-doped ZnO nanowalls obtained with 10 mM Tb(III) concentration, and (b) curve-fitting of the time profile measured with $\lambda_{\text{ems}} = 545$ nm.

We also investigate LSPR on the luminescence of the ZnO:Tb(III) nanowalls (supported on ITO-glass) that are decorated with NPs of three different noble metals: Ag, Pt and Au. The deposition of the NPs has been performed by simple dip-casting. The amount of the deposited NPs could be increased by increasing the number of dip-casting cycles. The PL spectra so obtained are resolved into two emission parts: sharp Tb(III)-related emission features and broad ZnO-related emission bands. Figure 5.6 shows the plasmonic effects of Ag, Pt and Au NPs on the emission spectra of the ZnO:Tb(III) nanowalls obtained with 10 mM Tb(III) concentration. (The emission spectra are obtained with excitation wavelength set at 325 nm.) For Ag NPs, the relative intensities of the broad ZnO near-band-edge emission band at 369 nm and the sharp Tb(III) $^5D_4 \rightarrow ^7F_5$ peak at 545 nm are not affected by the first three dip-casting cycles, after which the relative band intensities of the two emission features increase with increasing number of dip-casting cycles. After eight dip-casting cycles, the enhancement of the two emission features has reached a maximum. Relative to the undecorated ZnO:Tb(III) nanowalls, the Tb(III) $^5D_4 \rightarrow ^7F_5$ emission peak and the ZnO band-edge emission band of the NP-decorated ZnO:Tb(III) nanowalls are found to increase by approximately ten-fold and six-fold, respectively. Since the energy transfer from ZnO band-edge emission (donor) to intrinsic defects and that to Tb(III) are competing with each other, this suggests that as acceptors in the energy-transfer processes the Tb(III) dopants could be significantly more effective than the intrinsic defects of ZnO. The LSPR enhancement introduced by the Pt NPs is evidently less than that by the Ag NPs (Figure 5.6b). For the Pt NPs, five dip-casting cycles produce the maximum LSPR on both emission bands, with more than six-fold and three-fold enhancements for the respective Tb(III) and ZnO-related emission bands. Surprisingly, the Au NPs (Figure 5.6c) do not appear to enhance the emission from the Tb-doped ZnO nanowalls. Insets of Figure 5.6 compare the PL emission lines of the untreated sample and the NP-decorated ZnO:Tb(III) nanowall sample that give the maximal intensities, after removing the underlying broad band intensities.

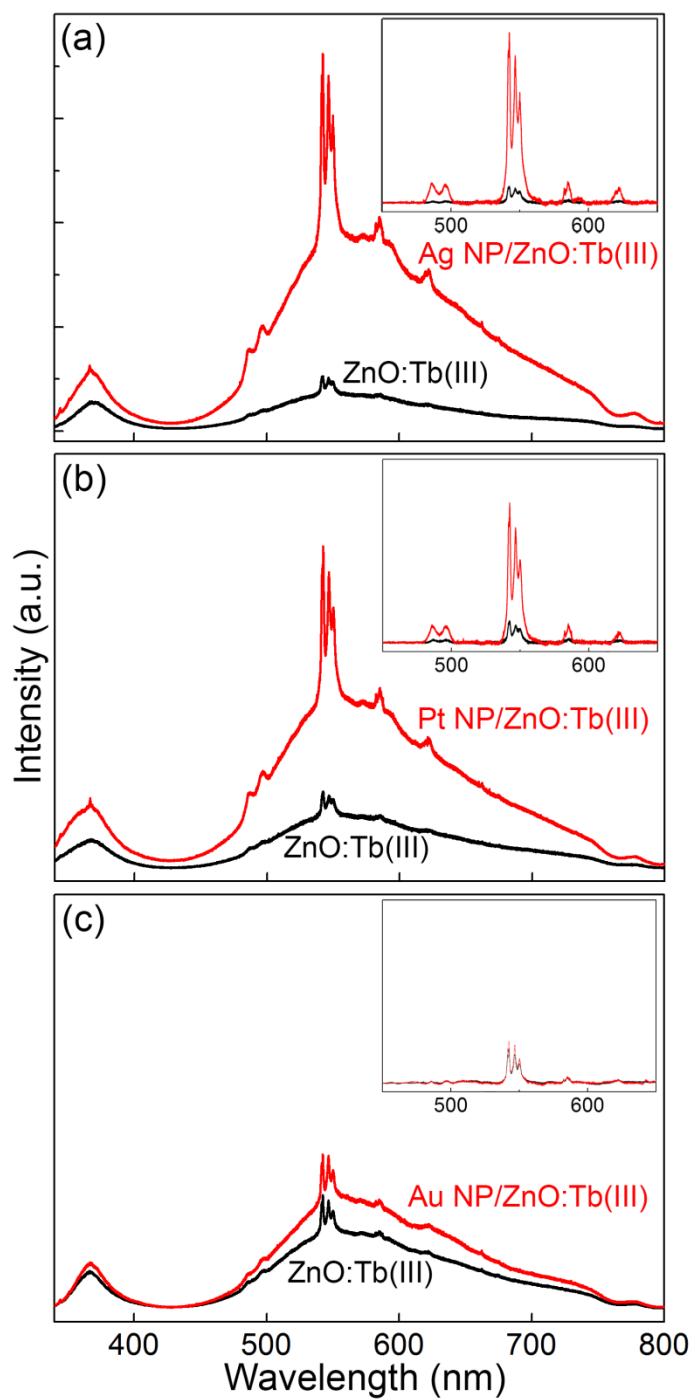


Figure 5.6 PL spectra ($\lambda_{\text{exn}} = 325$ nm) of Tb-doped ZnO nanowalls decorated with the appropriate amounts of (a) Ag NPs, (b) Pt NPs, and (c) Au NPs to exhibit the maximal LSPR effect (with the same Y-scale) compared with untreated Tb-doped ZnO nanowalls. Insets show the corresponding PL spectra after subtracting the broad backgrounds.

5.3.3 Surface Modification by Rhodamine B

To evaluate the potential use of ZnO:Tb(III) nanowalls as a fluorescence-based chemosensor, we measured the PL spectra of the ZnO:Tb(III) nanowalls treated with sequential applications of 1 and 3 drops of 10 mM RhB solution in CH₂Cl₂. Figure 5.7 compares the PL spectra of these RhB/ZnO:Tb(III) nanowall heterostructures with that of untreated ZnO:Tb(III) nanowalls, all obtained with excitation wavelength set at 325 nm. For the one-drop RhB treatment, the visible emission band maximum is evidently shifted from 550 nm to 643 nm and results in reduction in the intensity of the Tb(III) green emission at 545 nm. This red-shift is more apparent for the ZnO:Tb(III) nanowalls treated with three drops of RhB, with the band maximum now located at 693 nm along with a weak shoulder at 600 nm and the Tb(III) lines totally quenched. In a separate experiment, a RhB thin film was deposited on a quartz substrate and excitation at 325 nm does not produce any emission from the RhB film.

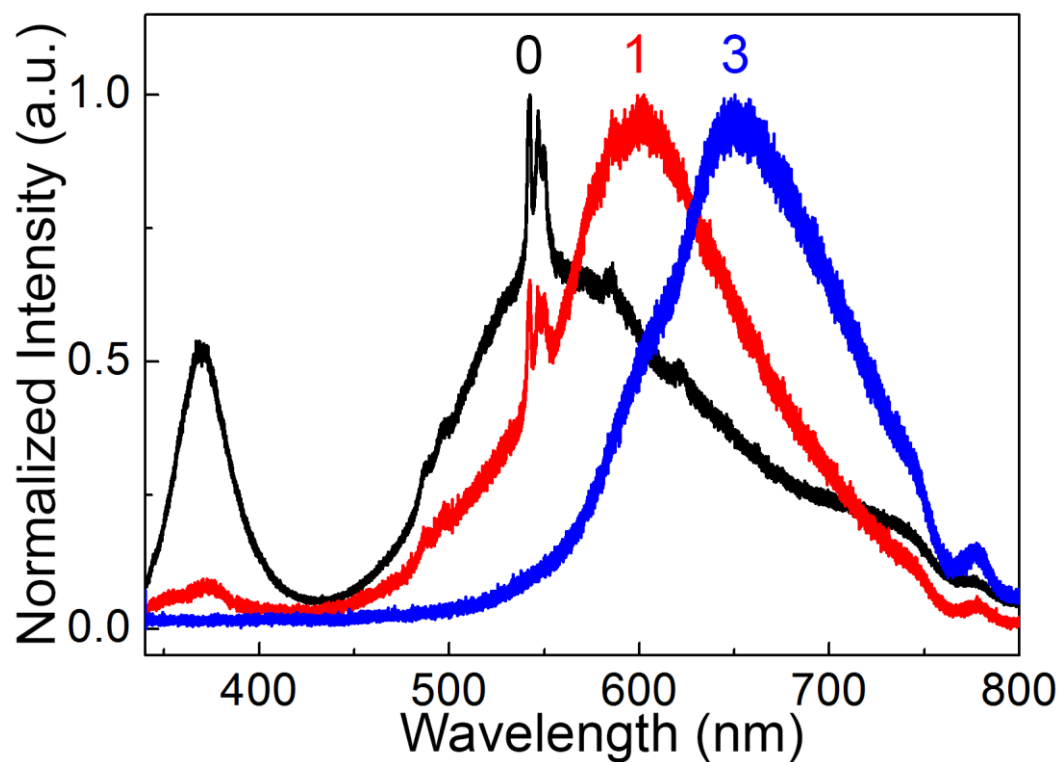


Figure 5.7 Emission spectra ($\lambda_{\text{exn}} = 325$ nm) of Tb-doped ZnO nanowalls without and with 1 and 3 drops of Rhodamine B (RhB) treatment. These spectra have been normalized at their respective maximum band intensities.

5.3.4 Energy Transfer Mechanism of Terbium-Doped ZnO Nanowalls and Hybrid Structure With Rhodamine B

To account for the observed spectral changes on Tb-doped ZnO nanowalls induced by RhB, we propose a new energy transfer mechanism. Figure 5.8a illustrates the energy-level scheme responsible for the sensitized emission from Tb(III) via an energy transfer mechanism. Taking into account the resonance energy transfer, the $^5L_{10}$ (27100 cm^{-1} , 3.36 eV) and 5G_6 (26500 cm^{-1} , 3.29 eV) states of Tb(III) play a key role in receiving the energy from the ZnO nanostructures, because these two states lie just below the conduction band (CB) of ZnO.⁸⁰ The energy transfer is initialized by the excitation of ZnO from the valence band (VB) to upper levels in the CB, followed by the subsequent relaxation from the upper levels to the lowest level in CB. Two optical de-excitation processes could take place competitively from the lowest CB level: (a) direct radiative transition to VB with $\lambda_{\text{ems}} \approx 376\text{ nm}$ (i.e. the ZnO band-edge emission), and (b) energy transfers to the dopant Tb(III) via the $^5L_{10}$ and 5G_6 states (Figure 5.8a) and to the intrinsic defects localized near CB (not shown). In the ZnO:Tb(III) nanowalls, the energy transfers are evidently more effective than the radiative transition, because the visible Tb(III) emissions and the ZnO defect-related emissions are much stronger than the 376 nm emission. The subsequent relaxation from the receiving $^5L_{10}$ and 5G_6 states to the emitting 5D_4 state at 20500 cm^{-1} (2.04 eV) then results in a series of sharp emission lines from the Tb(III) 5D_4 state to the 7F_J ($J=6, 5, 4, 3$) states that span over the 480-640 nm region.

For the RhB/ZnO:Tb(III) hybrid heterostructure (Figure 5.8b), the red emission from RhB is generated by efficient energy transfer from the ZnO:Tb(III) nanowalls. In the Förster theory, the energy-transfer efficiency is governed by not only the spectral overlap between the donor emission spectrum and the acceptor excitation spectrum but also the separation between the donor and the acceptor. The maximum separation over which the Förster energy-transfer can take place is typically 30-50 Å. For the hybrid structure, there is essentially no gap between the donor layer and the acceptor layer so that the energy transfer could take place very efficiently. A cascading energy-transfer model is proposed for the red emission from the hybrid structure. As shown in Figure 5.8a, the population of the 5D_4 state of Tb(III) is enhanced via the energy transfer from ZnO CB to Tb(III). The 545 nm emission (from the 5D_4 state to the 7F_5 state, one of the 7F_J states) of Tb(III) coincides with the excitation peak from the $^1\pi$ ground state to the $^1\pi^*$ excited state of RhB. For the hybrid structure, the cascade energy transfer originated from the CB of ZnO to the $^1\pi^*$ excited state of RhB through the interface between the nanowall surface and the RhB layer via the 5D_4 state of Tb(III) dopant (acting

as the intermediate “cascade” state) by non-radiative energy transfer. Subsequent relaxation from one of the $^1\pi^*$ vibronic states to one of the $^1\pi$ vibronic states then leads to the red emission.

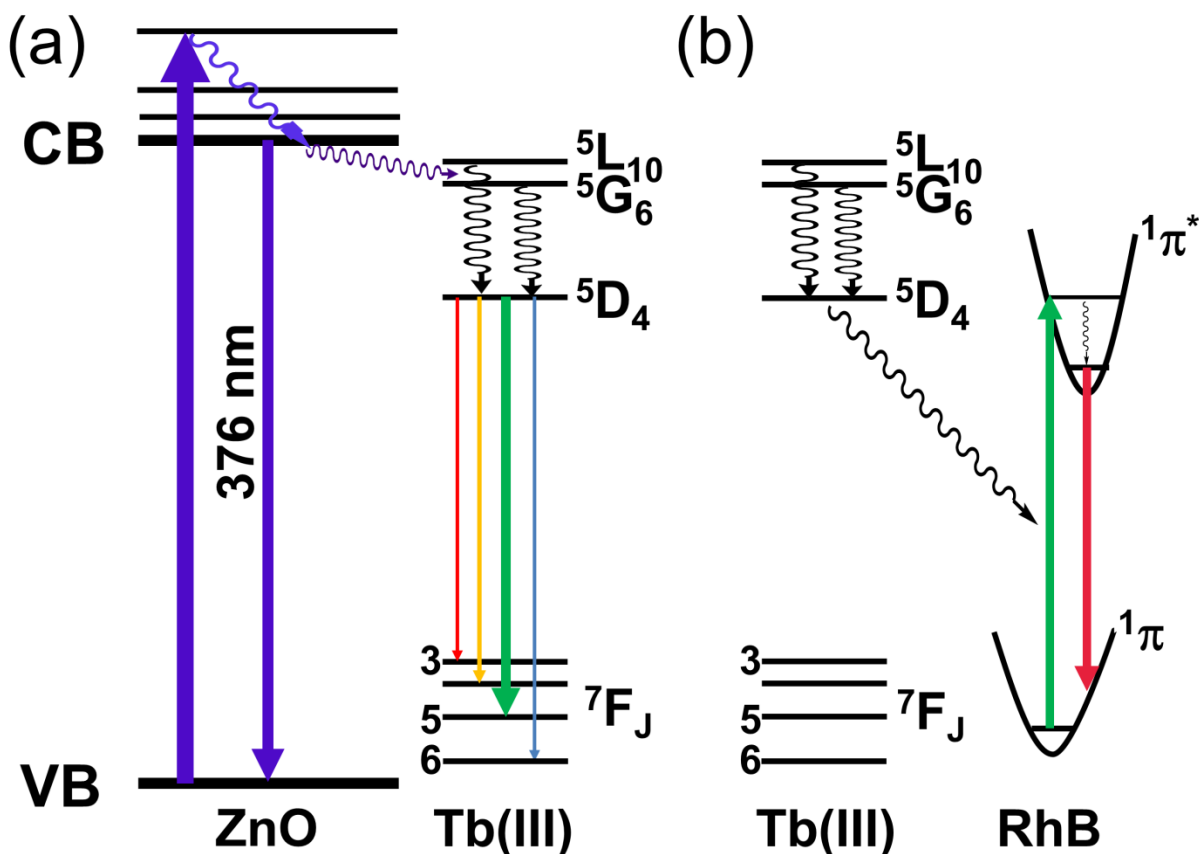


Figure 5.8 Energy-level diagrams illustrating the energy transfer mechanisms between (a) ZnO nanowalls and dopant Tb(III), resulting in the ZnO near band gap emission (at 376 nm) and several characteristic Tb(III) emissions in the visible range, and (b) ZnO:Tb(III) nanowalls and Rhodamine B (RhB) producing the red emission from the RhB/ZnO:Tb(III) nanowall hybrid structure.

5.4 Summary

We have successfully synthesized Tb-doped ZnO nanowalls using a facile electrochemical deposition method. The SEM data show that the concentration of Tb(III) ions could affect the thickness of the as-grown ZnO nanowalls. Depth-profiling O 1s and Tb 3d XPS spectra confirm that Tb is uniformly distributed throughout the ZnO nanowalls. PL measurement shows that the strong and sharp Tb(III)

green emission lines are superposed on the ZnO defect-related emission band via energy transfer from ZnO to Tb(III). The sensitized emission from Tb(III) is remarkably responsive to the LSPRs of Ag and Pt nanoparticles (but surprisingly not to Au nanoparticles), compared with the band-edge and the defect-related emission from the ZnO nanostructures. Furthermore, it is found that the enhanced green emission is very effective in sensitizing the fluorescence via the cascade energy transfer from the ZnO:Tb(III) nanowalls to the RhB dye through Tb(III) serving as the cascade/interface between the nanowall and the dye layer in the hybrid dye/doped-nanowall structure. The hybrid structure promises potential applications in the fluorescence-based probes and chemosensors.

Chapter 6

Photophysical and Interfacial Properties of Rare Earth Transition Metal Complex/ZnO Nanowall Hybrid Structures: Energy Transfer from ZnO to Rare Earth Transition Metal

6.1 Introduction

Surface-functionalized ZnO nanomaterials with organic molecules have attracted a great deal of interest due to their potential applications in optoelectronics, biological fluorescence labeling and imaging, and photocatalysis.^{244–253} ZnO nanomaterials excited by deep UV light produce UV and visible emissions, the intensities of which are greatly dependent on the dimension and morphology of the nanostructure due to quantum confinement effect. The UV emission results from the recombination of an electron from the conduction band (CB) with a hole in the valence band (VB), while the visible emission generally originates from various intrinsic defects localized near the CB or VB. Recently, the energy levels arising from defects near the CB have been recognized as energy states for excitation of organic fluorophores such as Nile Red and AlexaFluor 594.^{254–256} The energy transfer from the donor (ZnO) to the acceptor state (fluorophores) leads to intensity increase in the fluorophore emission at the expense (with intensity reduction) of the ZnO defect-related emission. On the other hand, some organic dyes have also been found to play the important role of a donor to the ZnO nanostructures. For example, the ZnO/anthracene system produces significantly enhanced UV emission via energy transfer from anthracene to ZnO.^{257,258} Polydopamine on the surface of ZnO nanorods enhances both the UV and visible emissions from ZnO upon photoexcitation of the dye.²³⁷ The characteristic emissions of the ZnO nanomaterials associated with the near band edge transitions can be applicable as an energy donor to a hybrid system.

Among the trivalent rare earth transition metal cations, europium and terbium cations, with their respective characteristic red and green luminescence emissions, show unique photophysical properties, such as hypersensitivity to the environment, narrow bandwidth, and long lifetime in the millisecond range.^{97,100} However, the absorption coefficients of these ions are very small because of partially allowed $f \rightarrow f$ transitions. Generally, this weak absorption characteristic could be overcome by introducing an organic ligand to sensitize Ln(III) (Ln = Eu and Tb).¹⁰⁰ Unfortunately, the generation of new color by doping rare earth ions to ZnO nanostructures has been found generally not to be an easy task. The appearance of the red emission was dependent on the excitation energy and on

the morphology of ZnO nanostructure and whether thermal annealing has been performed or not.²²⁷ In Chapter 4, we fabricated ZnO nanowalls embedded with Eu on an ITO-glass substrate by a facile electrochemical method in order to improve their luminescence properties in the visible region.²²⁷ Although embedment of the trivalent Eu ions was definitively confirmed, both as-grown and thermally annealed Eu-doped ZnO nanowalls excited by a 325 nm He-Cd laser did not produce the expected 620 nm red emission from Eu(III), as presented in Chapter 4. Surprisingly, surface modification of the samples by 1,10-phenanthroline generated a sharp Eu(III) emission line at 620 nm. The observed photophysical properties led us to propose a cascade energy transfer model. Our results suggested that fabrication of ZnO nanowalls hybrid structures by surface functionalization with rare earth transition metal complexes could open new pathways for color tunability via energy transfer from the ZnO nanostructures (hosts) to the rare earth ions (guests). The present study seeks to implement and characterize the sensitized luminescence of ZnO nanostructures introduced by surface functionalization with the rare earth complexes. Both non-cascade and cascade energy transfer mechanisms have been used to account for the sensitized luminescence. In the present work, oxydiacetic acid (ODA) and 1,10-phenanthroline (phen) are chosen as the complexing agents. Due to its unique chemical structure of two terminal carboxylic acid functional groups connected to an ether group, ODA is a versatile complexing agent with five potential oxygen-donor atoms.²⁵⁹ In addition, ODA shows no absorption in the near UV region, and it is generally believed that ODA involves non-cascade energy transfer.^{215,260} On the other hand, upon surface-functionalized Eu-doped ZnO nanowalls with phen, phen has been shown to act not just as a chelating ligand but also as an intermediary (between an acceptor and a donor) in the energy transfer from ZnO to Eu(III).^{227,261} We extend this recent study to the synthesis of Ln(III) complexes based on ODA and phen and use these complexes for surface functionalization of ZnO nanowalls for the first time. The photoluminescence, emission and excitation spectra, and quantum yields of the intrinsic and the sensitized luminescence of the ZnO nanowalls are characterized in detail. The photophysical properties of hybrid ZnO nanowall structures with ODA and phen Ln(III) complexes can then be compared with those of the Ln-doped ZnO nanowalls.

6.2 Experimental Details

6.2.1 Chemicals

Zn(NO₃)₂•6H₂O (98%, Sigma-Aldrich), and KCl (≥99.0%, Sigma-Aldrich), as a supporting electrolyte, were employed to prepare the ZnO nanowalls. EuCl₃•6H₂O (99.9%), Eu(NO₃)₃•5H₂O (99.9%), TbCl₃•6H₂O (99.9%), Tb(NO₃)₃•5H₂O (99.9%), 2,2'-oxydiacetic acid (or ODAH₂) (98%), 1,10-phenanthroline (98%), sodium hydroxide (≥98%) and methanol (≥99.9%) were purchased from Sigma-Aldrich and were used without further purification.

6.2.2 Fabrication of ZnO Nanowalls

A conventional three-electrode electrochemical deposition system (CH Instruments 660A) was used to deposit ZnO nanowalls on a glass substrate coated with ITO (150-200 nm thick with a sheet resistance of 4–8 ohm), used as the working electrode. An Ag/AgCl reference electrode and a Pt wire counter electrode were used. During the deposition, a constant voltage of –1.4 V vs Ag/AgCl was applied, with the deposition temperature of the sample kept constant at 80 °C using a temperature-controlled water bath. An aqueous electrolyte solution of 0.1M Zn(NO₃)₂•6H₂O and 0.1M KCl (used as a supporting electrolyte) was employed to prepare the ZnO nanowalls.

6.2.3 Synthesis of Lanthanoid Complexes

For ODA-based Ln(III) complexes, a molar ratio of 1:3 between the corresponding lanthanoid chloride salts and ODAH₂ were used, with the pH level adjusted to 6 using a dilute NaOH solution. More details about the synthesis procedures are given elsewhere.^{262,263} For phen-based Ln complexes, the corresponding lanthanoid nitrate salts were dissolved in 25 mL methanol. Phen/methanol solution with 8 times higher molar concentration of lanthanoid salt was slowly added to the lanthanoid salt/methanol solution and stirred for 12 hours. The resulting phen-based Ln complexes were then obtained by filtering the solution, followed by rinsing with methanol and dried under vacuum until further characterization.

6.2.4 Characterization

X-ray photoelectron spectroscopy was performed by using a Thermo-VG Scientific ESCALab 250 Microprobe equipped with an Al K α (1486.6 eV) and a Mg K α (1253.6 eV) sources, capable of an energy resolution of 0.8 eV full width at half-maximum. Photoluminescence and emission spectra of Ln(III) complexes, pristine ZnO nanowalls and ZnO nanowalls surface-functionalized with Ln(III)

complexes were collected by using a custom optical setup. This setup employed an ARC 0.5 m Czerny-Turner monochromator and a cooled Hamamatsu R-933-14 photomultiplier tube as the exit optics, with the excitation source optics consisting of either a He-Cd 325 nm laser line (used for photoluminescence spectra) or an Oriel 1000 W lamp (operated at 600 W, used for emission spectra) coupled with an Oriel MS257 monochromator.^{215,227}

6.3 Results and Discussion

6.3.1 Photoluminescence Measurement of Lanthanoid Complexes

Figures 6.1a and 6.1b show the emission and excitation spectra of the $\text{Eu}(\text{phen})_2(\text{NO}_3)_3$ (hereafter, referred to as EuPhen) and $\text{Na}_3[\text{Eu}(\text{ODA})_3]$ complexes (hereafter referred to as EuODA), respectively, in powder form at room temperature. The respective schematic molecular structures of the EuPhen and EuODA, based on the single-crystal diffraction data from literatures,^{215,264} are shown in Figures 6.1c and 6.1d. Upon irradiation by a UV-lamp (at 365 nm), EuPhen powder (Figure 6.1d) and EuODA powder (Figure 6.1f) both produce their characteristic red emissions, with stronger luminescence from the EuPhen powder. For EuPhen, trivalent europium cations are coordinated to six oxygen atoms from three nitrate groups and to four nitrogen atoms from two phen molecules to establish a monoclinic structure.²⁶⁴ Upon excitation at 350 nm, the EuPhen powder produces a series of sharp lines, corresponding to the $^5\text{D}_0 \rightarrow ^7\text{F}_J$ ($J = 1, 2, 3$ and 4) transitions of Eu(III). Unlike other $^5\text{D}_0 \rightarrow ^7\text{F}_J$ ($J = 2, 3$ and 4) transitions, the $^5\text{D}_0 \rightarrow ^7\text{F}_1$ triplet with peaks at 589.6, 591.4 and 594.2 nm (Figure 6.1a, inset) is magnetic dipole allowed. This transition reflects the site symmetry of the Eu(III) cation in the number of peaks, and its moderate intensity is essentially independent of the local bonding environment. The $^5\text{D}_0 \rightarrow ^7\text{F}_2$ singlet transition at 614.4 nm is the most prominent feature in the emission spectrum. The intensity of this transition is more than 15-fold stronger than that of the $^5\text{D}_0 \rightarrow ^7\text{F}_1$ transition. The $^5\text{D}_0 \rightarrow ^7\text{F}_3$ transition at 648.2 nm is the weakest. The $^5\text{D}_0 \rightarrow ^7\text{F}_4$ pentaplet with component peaks at 680.8, 683.0, 684.8, 686.8 and 699.4 nm is almost as intense as the $^5\text{D}_0 \rightarrow ^7\text{F}_1$ transition. In addition, the excitation spectrum of the EuPhen complex has been measured at room temperature by monitoring the emission intensity of the $^5\text{D}_0 \rightarrow ^7\text{F}_2$ singlet transition at 614.4 nm. The broad band over the 250-400 nm range with maximum at 355 nm (marked as ET in Figure 6.1) is attributed to an energy transfer from phen to Eu(III). A series of sharp excitation lines appearing in the low-energy side of the energy transfer band corresponds to the direct excitation of Eu(III) from the $^7\text{F}_0$ ground state.⁷⁷

The corresponding emission and the excitation spectra of EuODA powder, a non-sensitized Eu(III) complex, are shown in Figure 6.1b. In the emission spectrum, the $^5D_0 \rightarrow ^7F_1$ transition at 595 nm is the most prominent transition and it is considerably stronger than the $^5D_0 \rightarrow ^7F_2$ doublet with component maxima at 613.6 nm and 617.8 nm. For EuODA, the Eu(III) ion formed a tricapped trigonal prismatic geometry by coordinating to six equivalent oxygen atoms from the terminal carboxylates and to three equivalent oxygen atoms from the center (Figure 6.1e).²¹⁵ The high-order symmetry of the Eu(III) nucleus in EuODA might cause less hypersensitivity, when compared with EuPhen. The excitation spectrum shows that the red emission at 595 nm could only be generated by direct excitation of Eu(III) in EuODA.

The emission and excitation spectra, schematic molecular structures and photographs exposed to 365 nm UV lamp of Tb(phen)₂(NO₃)₃ (referred to as TbPhen) and Na₃[Tb(ODA)₃] (referred to as TbODA) are shown in Figure 6.2.^{215,264} Similar to the Eu(III) complexes, TbPhen (Figure 6.2c) produces stronger green luminescence than TbODA (Figure 6.2e). As shown in Figure 6.2a, the broad peak at 250-400 nm shows that the ligand phen plays an important role as a sensitizer toward the Tb(III) ion in TbPhen, as similarly found for that in EuPhen. The Tb(III) cation excited by a 325 nm He-Cd line produces the characteristic $^5D_4 \rightarrow ^7F_J$ (J = 6, 5, 4, 3) emission lines at 489.0, 540.6, 582.4 and 620.2 nm, respectively, with the $^5D_4 \rightarrow ^7F_5$ transition providing the most intense luminescence. For the other ($^5D_4 \rightarrow ^7F_{6,4,3}$) transitions, moderate sensitivity to the ligand environment has been observed. The excitation spectrum of the $^5D_4 \rightarrow ^7F_5$ transition at 540.6 nm consists of a broad band (over the 250-450 nm range) with maximum at 358 nm and a sharp peak at 489 nm (Figure 6.2a). The broad excitation band indicates that the emission from Tb(III) is effectively produced via the energy transfer from the ligand phen. The discernible weak peak at 381 nm superposing on the energy transfer band is attributed to the direct $^7F_6 \rightarrow ^5G_6$ excitation of Tb(III). For TbODA, the emission spectrum (Figure 6.2b) is similar to that of TbPhen (Figure 6.2a), with the hypersensitive emission arising from the $^5D_4 \rightarrow ^7F_5$ transition at 541.6 nm. Other emission lines corresponding to $^5D_4 \rightarrow ^7F_{6,4,3}$ transitions are located at 486.9, 584.8 and 620.4 nm, respectively.⁸⁰ The excitation spectrum of the 541.6 nm emission consists of a series of sharp lines in the 250-390 nm range and a sharp line at 489 nm (Figure 6.2b). This therefore confirms that the green emission from Tb(III) at 541.6 nm is produced only by direct excitation and not by any energy transfer mechanism as found for TbPhen.

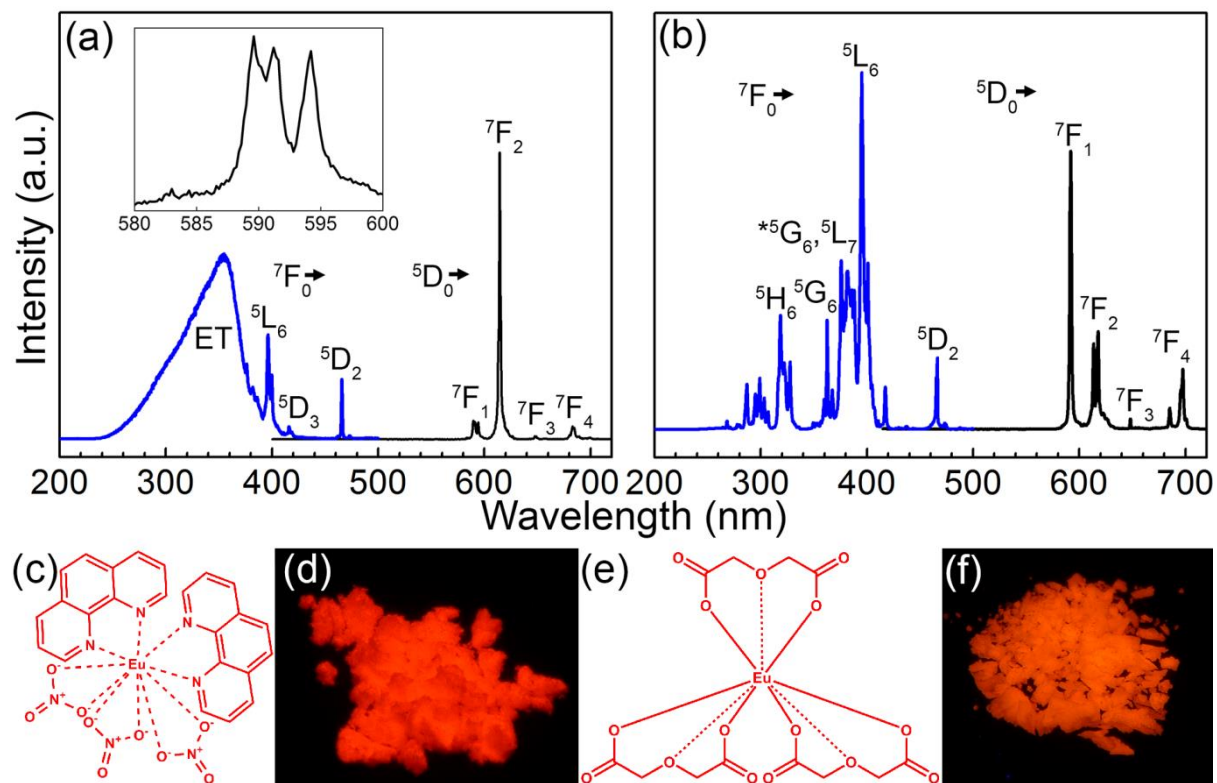


Figure 6.1 Excitation spectra (blue lines, 200-500 nm) with (a) $\lambda_{\text{ems}} = 614.4$ nm for EuPhen and (b) $\lambda_{\text{ems}} = 595$ nm for EuODA powders and emission spectra (black lines, 400-700 nm) with (a) $\lambda_{\text{exn}} = 350$ nm for EuPhen and (b) $\lambda_{\text{exn}} = 396$ nm for EuODA powders. Magnetic dipole transition (${}^5\text{D}_0 \rightarrow {}^7\text{F}_1$) of Eu is shown in inset of (a). (c, e) Schematic molecular structures and (d, f) photographs under UV illumination at 365 nm of (c, d) EuPhen and (e, f) EuODA.

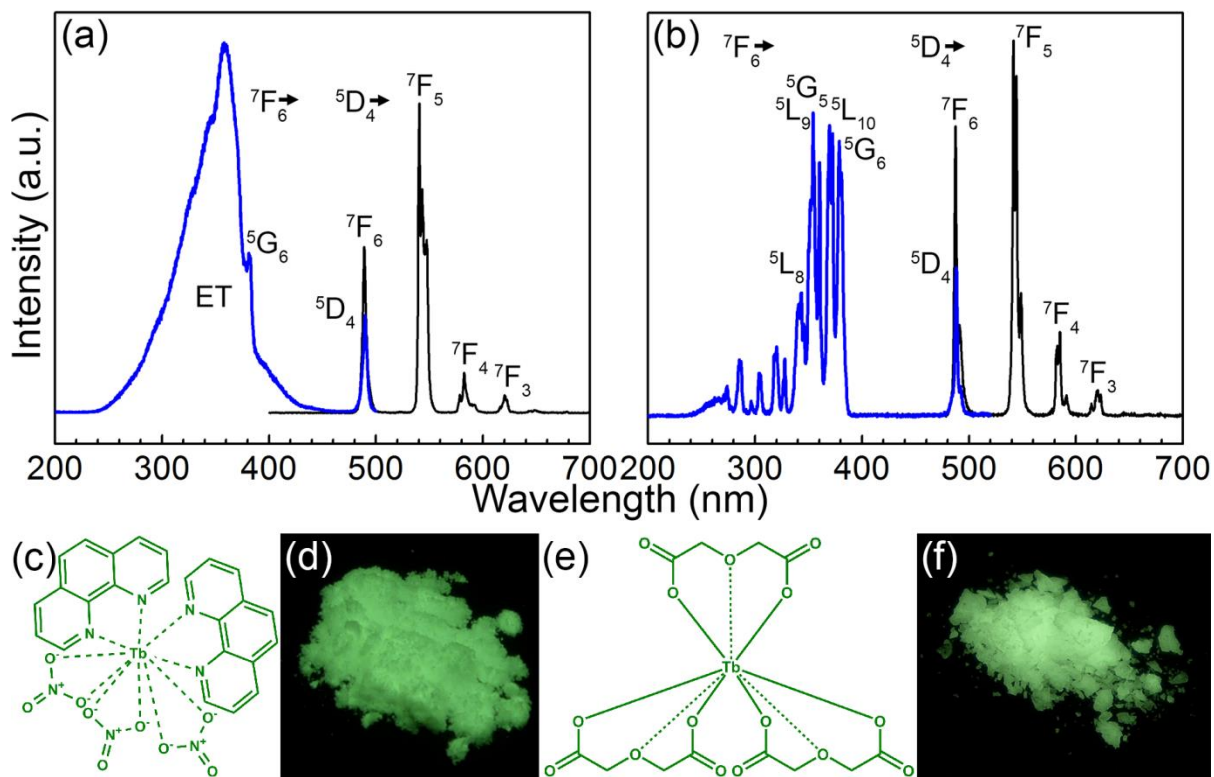


Figure 6.2 Excitation (blue, 200-500 nm) with (a) $\lambda_{\text{ems}} = 540.6$ nm for TbPhen and (b) $\lambda_{\text{ems}} = 541.6$ nm for TbODA, and emission spectra (black, 400-700 nm) with (a) $\lambda_{\text{exn}} = 350$ nm for TbPhen and (b) $\lambda_{\text{exn}} = 354$ nm for TbODA. (c, e) Schematic molecular structures and (d, f) photographs under UV illumination at 365 nm of (c, d) TbPhen and (e, f) TbODA.

6.3.2 PL and Excitation Spectra of Lanthanoid Complex/ZnO Nanowall Hybrid Structures

After the surface of the ZnO nanowalls was drop-casted separately with different amounts of each of the EuPhen and EuDOA solutions, we collected the PL spectra of the resulting ZnO nanowall hybrid sample. As shown in Figure 6.3a, the pristine ZnO nanowalls, i.e. without any EuPhen (C0), produce characteristic emissions from the nanowalls: a deep-blue band at 375 nm corresponding to band-edge emission from bound excitons and a broad visible band at 550 nm attributed to defect-related emission. When the amount of EuPhen on ZnO nanowall surface reaches 12 μg (C1), the $^5D_0 \rightarrow ^7F_2$ emission from Eu(III) at 614.4 nm becomes discernibly visible, and its intensity increases with increasing amount of EuPhen drop-casted on the nanowalls to 24 μg (C2). The Eu(III) emission at

614.4 nm for EuPhen has become predominant at 36 μg (C3). The excitation spectrum of the 615 nm emission measured for C3 (Figure 6.3a, inset) shows a broad band over the 300-360 nm range. There is only minor difference in the emission band shapes of the EuPhen complexes between the powder and the C3 drop-cast sample on ZnO nanowalls. In particular, the peak with maximum at 350.5 nm appears slightly blue-shifted by ~ 5 nm and with narrower band width for the powder sample than the hybrid sample. These results lead us to propose that the observed broad excitation band at 300-350 nm for the hybrid sample corresponds to the indirect excitation by band-edge emission of ZnO nanowalls. Similarly, the surface of ZnO nanowalls was functionalized by drop-casting different amounts of EuODA dissolved in ethanol. Figure 6.3b shows the PL spectra of the EuODA-functionalized ZnO nanowalls measured with increasing amounts of drop-casted EuODA (C0 – C4, from 0 to 120 μg in steps of 30 μg). For pristine ZnO nanowalls (i.e. C0), only the band-edge and the defect-related ZnO emission are observed, while the $^5\text{D}_0 \rightarrow ^7\text{F}_1$ emission at 595 nm begins to emerge for the C1 drop-casted sample. With increasing drop-cast amount of EuODA, the intensity of the Eu(III) emission increases and becomes the most prominent at C4 (120 μg). The excitation spectrum for the C4 sample is also obtained by monitoring the 595 nm emission (Figure 6.3b, inset). The corresponding spectral profile is nearly identical to that of EuPhen-functionalized ZnO nanowalls (Figure 6.3a, inset). This therefore indicates that the emission from the ZnO nanowalls functionalized with EuODA and that with EuPhen could be produced by a similar energy transfer mechanism involving the ZnO nanowalls.

We extend the surface-functionalization of the ZnO nanowalls to that by Tb(III) complexes. Figure 6.3c shows the PL spectra of the TbPhen surface-functionalized ZnO nanowalls with increasing amounts of TbPhen (C0-C3, from 0 to 36 μg in steps of 12 μg). For C1-C3, the band-edge and the defect-related emissions from the ZnO nanowalls are accompanied by sharp emission lines originated from Tb(III). As the emission features from Tb(III) increase in intensities, the broad emission bands from the nanowalls in the 450-700 nm region appear to reduce in intensity concomitantly. The excitation spectrum of the 540.6 nm emission (Figure 6.3c, inset) shows a broad band in the 250-360 nm region with maximum at 348.5 nm. The general spectral shape is somewhat distorted and found to be different from that for the TbPhen powder (Figure 6.2a). These results suggest that the observed emission from Tb(III) is produced via energy transfer from the ZnO nanowalls to Tb(III), and that the energy transfer is less effective than the case for the EuPhen-functionalized ZnO nanowalls (Figure 6.3a, inset). Figure 6.3d shows the corresponding PL spectra for the TbODA-functionalized ZnO nanowalls with increasing amounts of TbODA (C0-C4, from 0 to 120 μg in steps of 30 μg).

Evidently, the TbODA-functionalized ZnO nanowalls excited at 325 nm effectively produce the characteristic emission from Tb(III) with the hypersensitive $^5D_4 \rightarrow ^7F_5$ emission at 541.6 nm. The intensities and spectral evolution of the ZnO and Tb(III) related emission features follow those of TbPhen features (Figure 6.3c). The excitation spectrum measured for the 541.6 nm emission (Figure 6.3d, inset) shows similar spectral evolution as that of the EuODA/ZnO-nanowall hybrid samples (Figure 6.3b, inset). This demonstrates that the energy transfer from ZnO nanowalls generates the sensitized emission, which follows a similar trend as EuODA-functionalized ZnO nanowalls (Figure 6.3b, inset).

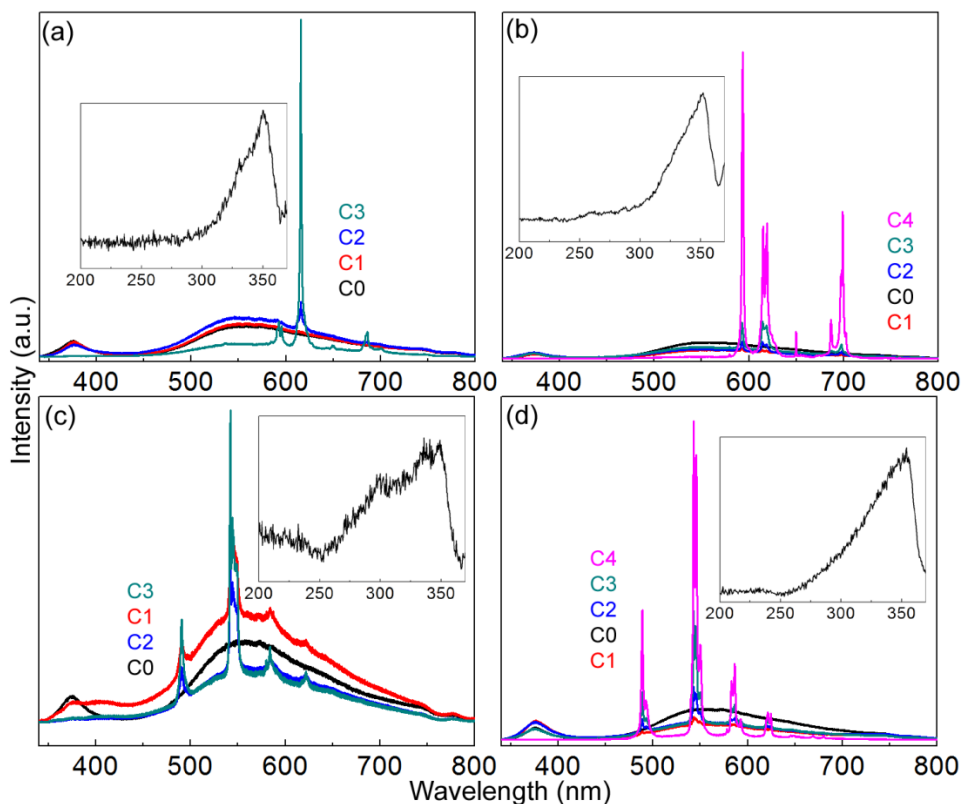


Figure 6.3 PL spectra ($\lambda_{\text{exn}} = 325$ nm) of ZnO nanowalls surface-functionalized with increasing amounts of (a) EuPhen, (b) EuODA, (c) TbPhen and (d) TbODA, with the corresponding excitation spectra ($\lambda_{\text{ems}} = 614.4, 595, 540.6,$ and 541.6 nm) for the respective samples shown as insets.

6.3.3 Energy Transfer Mechanisms

Recently, we propose a cascade energy transfer mechanism to account for the observed spectral evolution for phen-functionalized Eu-doped ZnO nanowalls, in which phen plays an important dual role as an acceptor from ZnO and as a donor to Eu(III).²²⁷ Figure 6.4a compares the excitation spectra of pristine phen, EuPhen and TbPhen powders, and band edge emission of pristine ZnO nanowalls and an emission (phosphorescence) spectrum of pristine Phen. Figure 6.4b and 6.4c show schematic models for the optical processes involved in the sensitized luminescence of EuPhen- and TbPhen-functionalized ZnO nanowalls via the cascade energy transfer mechanism, respectively. First, Phen is excited by the band-edge emission of ZnO nanowalls and it undergoes phosphorescence in the 400-600 nm range. The excitation bands of Eu and Tb trivalent cations appear to overlap with the phosphorescence signal. Three peaks from Eu(III) (${}^7F_0 \rightarrow {}^5D_2$ at 466.5 nm and two ${}^7F_1 \rightarrow {}^5D_1$ excitations at 528.6 and 537.0 nm) and one peak from Tb(III) (${}^7F_6 \rightarrow {}^5D_4$ at 489.0 nm) receive energy and generate characteristic Eu(III) and Tb(III) emissions. Taking into account the peak positions of the excitation spectra of ZnO nanowalls (350.5 nm) and phen (355 nm), the singlet excited state ${}^1S^*$ of phen lies just below the conduction band (CB) of ZnO. Initially, resonance energy transfer from the lower-energy levels of the CB of ZnO nanowalls to the singlet excited state ${}^1S^*$ of phen occurs. This is then followed by migration to the triplet state ${}^3T^*$ via an intersystem crossing. For the phen-incorporated Eu(III) complex, the 5D_2 and 5D_1 states act as the energy-receiving levels. For TbPhen, only the 5D_4 state is sufficiently close to the triplet state ${}^3T^*$ to act as the energy-receiving level. Finally, the intermolecular energy transfer takes place from the triplet state of phen to the respective resonance levels [5D_0 for Eu(III) and 5D_4 for Tb(III)], which gives rise to the characteristic emissions.

Figure 6.5a compares the band-edge emission of ZnO with the excitation spectra of EuODA powder and those of TbODA powder. For LnODA-functionalized ZnO nanowalls, the 5L_7 , 5G_5 and 5L_6 states of Eu(III) and the 5G_5 , ${}^5L_{10}$ and 5G_6 states of Tb(III) act as the energy-receiving levels, because these states lie just below the lower-energy CB levels of ZnO (Figure 6.5b and 6.5c). The non-radiative relaxation from the CB of ZnO to the energy-receiving levels of EuODA and TbODA competes with the case to ZnO defects. Figures 6.5b and 6.5c show the respective process of the sensitized luminescence for EuODA and TbODA complexes via energy transfer from the lower-level of the CB of the ZnO nanowalls.

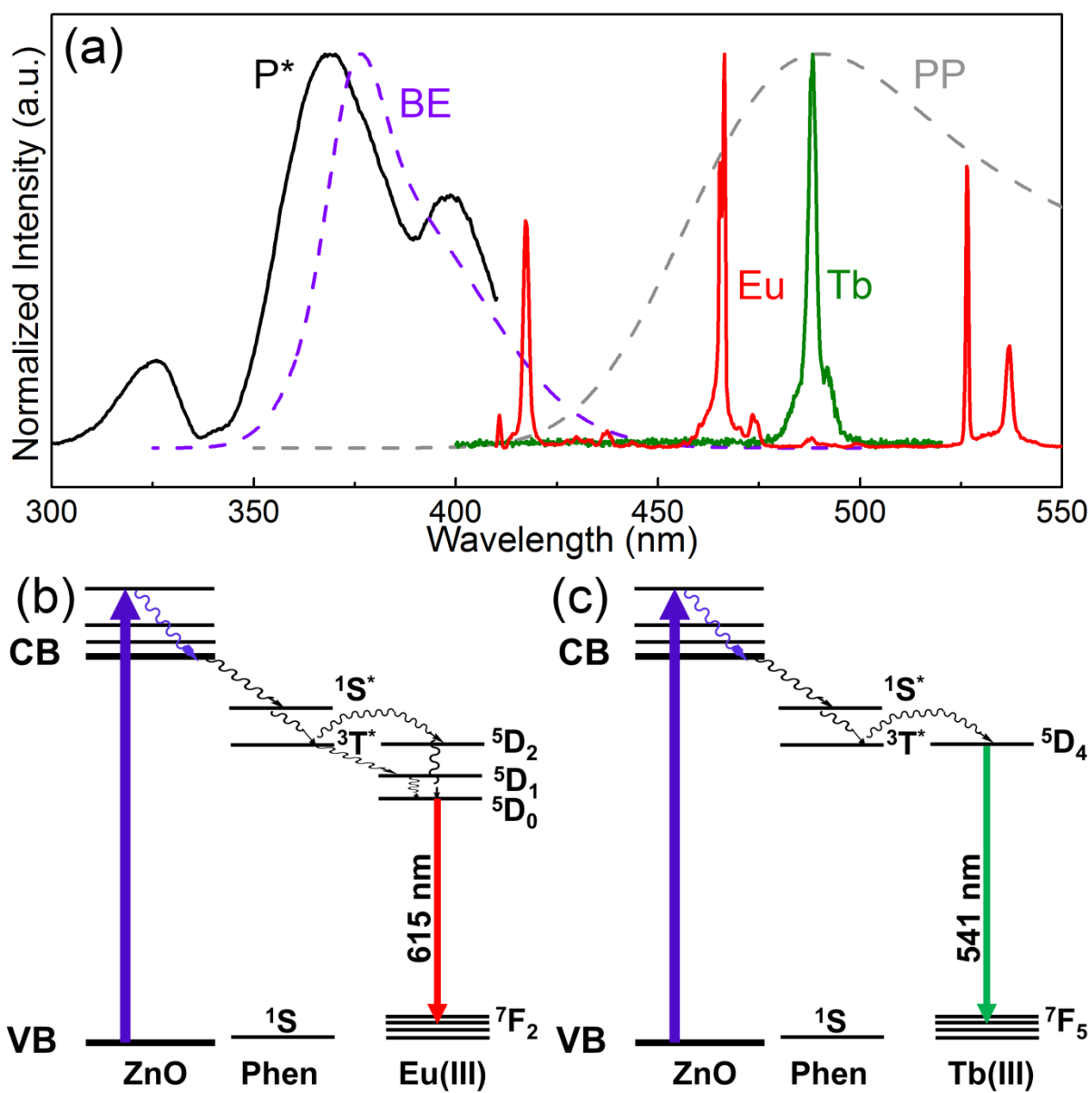


Figure 6.4 (a) A spectroscopic representation of processes involved in the cascade energy transfer from ZnO to EuPhen or TbPhen complex. The band-edge emission of ZnO nanowalls and excitation and phosphorescence spectra of phen are marked as BE, P* and PP, respectively. Schematic energy level diagrams for sensitized luminescence of ZnO nanowalls surface-functionalized by (b) EuPhen and (c) TbPhen.

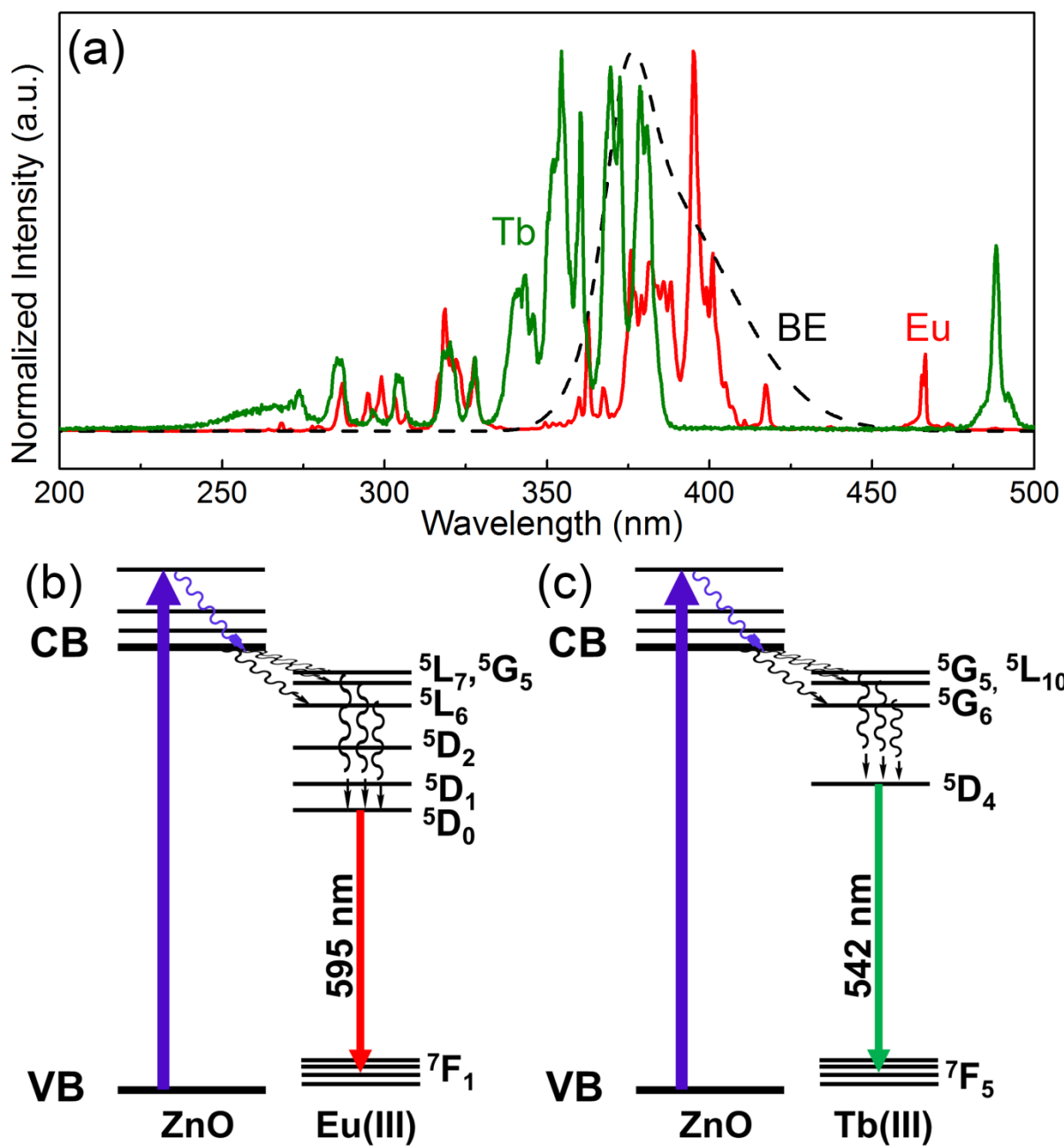


Figure 6.5 (a) A spectroscopic representation of processes involved in the non-cascade energy transfer from ZnO to EuODA or TbODA complexes. The band-edge (BE) emission of ZnO are shown along with the excitation spectra of Eu and Tb cations. Schematic energy diagrams of sensitized luminescence of ZnO nanowalls surface-functionalized by (b) EuODA and (c) TbODA.

6.3.4 Energy Transfer Efficiency and Absolute Quantum Yield

The efficiency of the energy transfer from ZnO nanowalls to the lanthanoid cation (Ln) can be written as:

$$\eta_{ET} = \frac{\int I_{Ln} d\lambda}{\int I_{total} d\lambda} \quad (6.1)$$

where I_{Ln} and I_{total} denote emission intensities generated by Ln and the hybrid sample, respectively.²⁶⁵ We calculate η_{ET} by first resolving the spectrum into the ZnO and Ln components and then evaluating the intensity of the Ln component and the total spectral intensity over the appropriate wavelength range. The resulting values of η_{ET} are found to be 30% for EuPhen, 90% for EuODA, 20% for TbPhen and 70% for TbODA. The higher η_{ET} values for LnODA complexes than those for LnPhen complexes indicate that the energy transfer for the ODA complexes is more efficient than that for the phen complexes. Furthermore, we also measure, in separate experiments, the absolute quantum yield of the Ln(III) complex powders and of ZnO nanowalls functionalized by Ln(III) complexes by using an integrating sphere with a diameter of 10 inch. Table 6.1 shows that the quantum yield of the LnPhen powder is higher than that of the LnODA powder. This result indicates that sensitization by Phen results in more efficient luminescence than direct excitation. Except the case of EuPhen-hybridized ZnO nanowalls, however, the emission intensities of the hybrid samples are too weak to produce reliable results, due to the very small amounts of the lanthanoid complexes on ZnO nanowalls. The quantum yield of the sensitized luminescence of EuPhen drop-casted on ZnO nanowalls is 0.0082%. The quantum yield (Q_{sens}) for the LnPhen/ZnO-nanowalls hybrid sample can be expressed as:

$$Q_{sens} = Q_{ZnO} \eta_{ET} Q_{Ln}^{phen} \quad (6.2a)$$

where Q_{ZnO} corresponds to the quantum yield of the ZnO luminescence and Q_{Ln}^{phen} represents the luminescence efficiency from phen to the final state of Ln(III). On the other hand, the quantum yield (Q_{sens}) for the LnODA/ZnO nanowalls hybrid sample is given by:

$$Q_{sens} = Q_{ZnO} \eta_{ET} Q_{Ln}^{Ln} \quad (6.2b)$$

where Q_{Ln}^{Ln} corresponds to the luminescence efficiency from the receiving excited states to the final state of Ln(III). Assuming that Q_{Ln}^{phen} and Q_{Ln}^{Ln} are nearly equal to the corresponding quantum yields of the powder, we obtain Q_{ZnO} to be 0.37%. Using this value, we determine Q_{sens} by using Eqs (6.2a) and (6.2b), and these values are shown in Table 6.1.

Table 6.1 Absolute PL quantum yields (%) of LnPhen and LnODA in powder state, and as surface-functionalized ZnO nanowalls ($\lambda_{\text{exn}} = 325 \text{ nm}$).

Ln(III) Complexes	Powder of Ln(III) complex Q_{sens} (%)	ZnO nanowalls drop-casted with Ln(III) complex	
		η_{ET} (%)	Q_{sens} (%)
EuPhen	7.2	30	0.0082
TbPhen	2.2	20	0.002
EuODA	0.55	90	0.002
TbODA	0.31	70	0.0008

6.3.5 Investigation of the Interfacial area of Lanthanoid Complex/ZnO Nanowall Hybrid Structures

Comparison between the PL spectra of LnPhen complex powders and those of ZnO nanowalls surface-functionalized by the LnPhen complexes reveals that there is no significant change in the emission band profile caused by surface-functionalization of the ZnO nanowalls and that the coordination environment of the Ln(III) ions is not affected by the adsorption of the complex on the ZnO nanowall. XPS spectra of the ligand phen, the $\text{Ln}(\text{phen})_2(\text{NO}_3)_3$ complex, and ZnO nanowalls surface-functionalized by LnPhen have been measured to verify the adsorption nature of the complex on the surface of ZnO nanowall. As shown in Figure 6.6a, the positions for the C 1s peaks for aromatic C–C bond at 285.8 eV and C–N bond at 286.5 eV remain essentially the same for isolated EuPhen and TbPhen and for the LnPhen/ZnO-nanowall hybrid sample. The N 1s peak at 400.1 eV corresponds to the C–N bond in isolated phen (Figure 6.6b), while the additional N 1s peak at 407.6 eV in LnPhen complex can be attributed to NO_3^- . Evidently, the adsorption of the LnPhen complexes on the ZnO nanowall surfaces does not affect the C–N N 1s peak position for the phen molecules. However, surface functionalization of ZnO nanowalls by LnPhen complexes causes the nitrate N 1s peak to shift from 407.6 eV to 406.9 eV. This shows that the partially positive-charged nitrogen atoms of the nitrate anions tend to bind to the unsaturated oxygen atoms of ZnO.

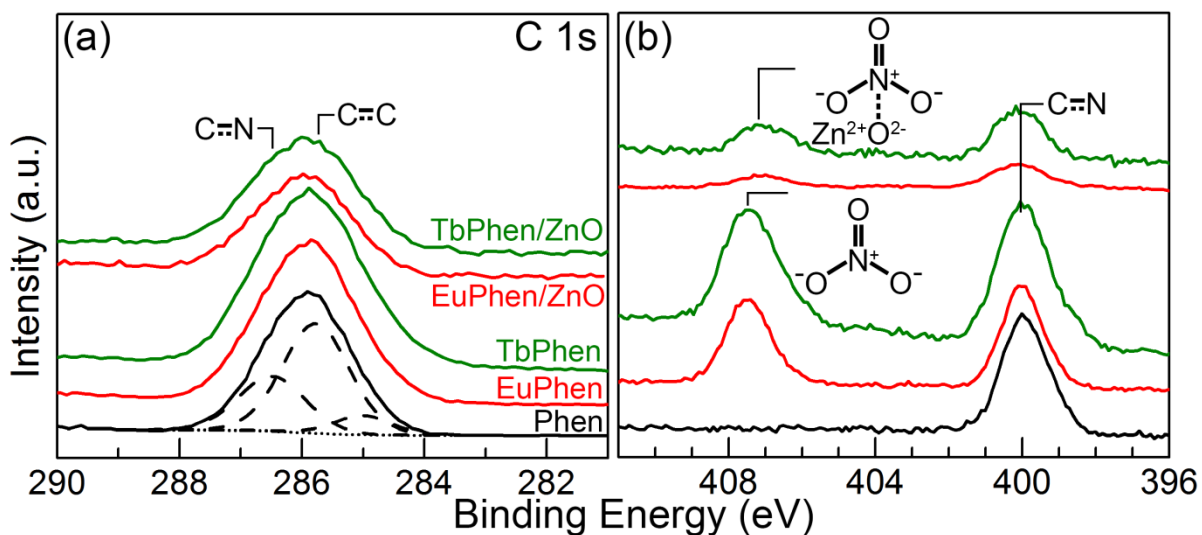


Figure 6.6 XPS spectra of (a) C 1s and (b) N 1s regions of Phen powder, EuPhen and TbPhen complexes, and ZnO nanowalls drop-casted with EuPhen and TbPhen complexes.

An early study of the X-ray crystal structure of $\text{Na}_3[\text{Ln}(\text{ODA})_3]$ showed that the Ln atom is completely encapsulated by coordination to the nine carboxylate oxygen atoms.²¹⁵ The highly efficient energy transfer from the ZnO nanowall to the LnODA drop-casted on its surface (Table 6.1) suggests that the interaction between the ZnO nanowall surface and the adsorbate (LnODA complex) is very strong. Figure 6.7a shows the C 1s spectra of ODA, LnODA and ZnO nanowalls surface-functionalized by LnODA. The well-resolved C 1s features at 286.8 eV and 289.3 eV can be assigned to ether and carboxylic acid functional groups, respectively. Upon ODA complex formation with Eu or Tb, the carboxylic acid group has evidently evolved to the carboxylate group (COO^-) with the higher-lying peak shifted to a lower binding energy by 0.6 eV to 288.7 eV. Both C 1s peaks of LnODA complexes appear unchanged upon adsorption on the surface of ZnO nanowalls. On the other hand, there are three different O 1s features in isolated ODA: C=O at 532.6 eV and C–O–H at 533.7 eV in the carboxylic acid groups, and the C–O–C ether group at 533.4 eV. The O 1s peaks for the C=O and C–O–H groups have shifted to lower binding energy by 0.3 eV and 1.4 eV, respectively, and they appear to form one large broad peak. For the ZnO nanowalls surface-functionalized with LnODA complexes, the carboxylate (COO^-) O 1s feature has shifted further by 0.4 eV to a higher binding energy in comparison to the position for LnODA. Since the coordination of the Ln atom has already fully satisfied with three ODA ligands, direct interaction between the O atom of the nanowall surface and the Ln atom could be ruled out. In addition, the near-identical PL spectral features in

Ln(III) complexes between the drop-casted and the powder samples further support that the local chemical bonding environment of Ln in the complexes remains unchanged upon adsorption on ZnO nanowalls. No change is also observed between PL spectra of LnODA powder and LnODA/ZnO-nanowall hybrid samples, which indicates that the nature of chemical bonding between the lanthanoid cations and ODA in the LnODA powder is the same as that in the hybrid structures. The O 1s spectra suggest that LnODA complexes likely adsorb by connecting C=O to Zn²⁺ on the surface of ZnO nanowalls in a unidentate arrangement. The Zn atoms exposed on the surface of the nanowall are generally less coordinated and provide the possible adsorption sites. In particular, the oxygen atom of the carbonyl group of ODA, with partial negative-charge towards the outside of the complex polyhedron, could bind to the Zn atom as an electron acceptor-donor pair on the nanowall surface. Taking into account that the O–Ln separation of O=C–O–Ln is ~ 5 Å, the Zn²⁺...O=C–O–Ln complexation upon functionalization may result in the proximate distance between the Zn and Ln atoms shorter than the limit distance (10 Å) in the Dexter’s energy transfer theory. The limit of the proximate distance so obtained is therefore consistent with our proposed cascade energy transfer mechanism.

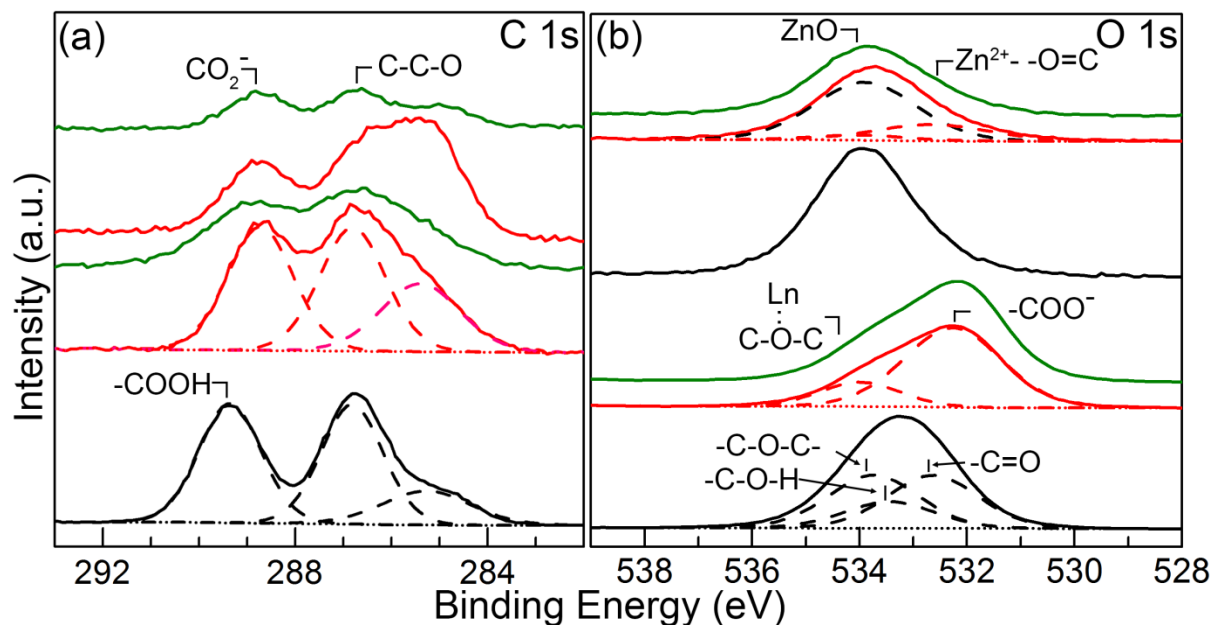


Figure 6.7 XPS spectra of (a) C 1s and (b) O 1s of ODA powder, EuODA and TbODA complexes, and ZnO nanowalls drop-casted with EuODA and TbODA complexes.

6.3.6 Comparison between Doping and Surface-Functionalization

Doping trivalent europium and terbium cations into ZnO nanowalls has been performed and the results are reported in Chapters 4 and 5. As-grown Eu-doped ZnO nanowalls generated one broad peak at 400-700 nm without any ZnO band-edge emission and characteristic Eu(III) emission. Thermal annealing and surface modification by phen were found to generate only relatively weak hypersensitive emission ($^5D_0 \rightarrow ^7F_2$) at 620 nm. On the other hand, ZnO nanowalls surface-functionalized with EuPhen and EuODA complexes exhibited significantly stronger characteristic emissions than europium-doped ZnO nanowalls. Surface functionalization of Eu(III) complexes, specifically EuPhen, could significantly modify ZnO emissions and enhance characteristic europium emission as a result of energy transfer from ZnO band-edge emission. Hence, surface functionalization method has more advantages than doping in case of europium-related emissions.

For terbium-related emissions, as-grown terbium-doped ZnO nanowalls showed intense characteristic terbium emission peaks with the strongest emission ($^5D_4 \rightarrow ^7F_5$) at 545 nm. The terbium emissions for terbium-doped ZnO nanowalls came from the energy transfer from ZnO band-edge emission to trivalent terbium cations, as supported by the excitation spectra ($\lambda_{\text{ems}} = 545$ nm). Surface functionalization of ZnO nanowalls by TbPhen and TbODA complexes successfully produced characteristic emissions in a similar manner as ZnO nanowalls hybridized by EuPhen and EuODA complexes. The quantum yield of terbium-doped ZnO nanowalls was measured to be 3.2%, which is of the same magnitude as that of TbPhen powder. Terbium doping of ZnO by electrochemical deposition is therefore more effective than surface functionalization for modification of ZnO emissions.

6.4 Summary

Rare-earth transition metal (Eu, Tb) complexes based on phen and ODA have been synthesized and their photophysical properties are studied in detail. Comparison of the emission spectra of phen-based and ODA-based Ln(III) complexes reveals the presence of hypersensitive $^5D_0 \rightarrow ^7F_2$ emission from Eu(III) and $^5D_4 \rightarrow ^7F_5$ emission from Tb(III) in phen-based Ln(III) complexes. The greater intensities found for these emissions are due to phen providing a conduit for energy transfer. Phen-based and ODA-based Ln(III) complexes have also been functionalized on the surface of ZnO nanowalls. Although the amount of complexes drop-casted on the nanowalls is less than a few hundred micrograms, significant changes in the emission spectra of the nanowalls and in the excitation spectra of Ln(III) complexes are observed. The overlap of excitation features of the Ln(III) complexes with

the band-edge emission of ZnO nanowalls suggests the viability of energy transfer between the Ln(III) complexes and ZnO. The energy transfer phenomena between the ZnO nanowalls and the Ln(III) complexes are confirmed by excitation spectra of the corresponding hybrid Ln(III) complex/ZnO nanowall samples. Schematic energy level diagrams of Ln(III) complex/ZnO nanowall hybrid samples are constructed. Phen-based and ODA-based Ln(III) complexes are found to exhibit maximum energy transfer efficiencies of 30% and 90%, respectively (Table 6.1). XPS studies of Ln(III) complexes and Ln(III) complex/ZnO nanowalls are in good accord with previously reported structures, and they reveal electrostatic interactions between O^- from ZnO and N^+ in NO_3^- of phen-based complexes and between Zn^{2+} from ZnO and $C=O$ of ODA. In comparison with Ln(III) doping of ZnO nanowalls (Chapter 4 and 5), surface modification by Ln(III) complexes is the preferred method for introducing europium to ZnO nanowalls while Ln(III) doping is the preferred method for introducing terbium to ZnO nanowalls.

Chapter 7

Concluding Remarks and Outlook

7.1 Conclusions

The objective of this thesis is to investigate quantum confinement effect of ultrathin 2-D ZnO nanostructures and energy transfer mechanisms between ZnO nanowalls and lanthanoid cations. A single-unit-cell thick ZnO quantum sheets, europium and terbium-doped ZnO nanowalls and surface functionalized ZnO nanowalls with europium and terbium complexes were studied in this thesis. Electrochemical deposition was employed for the nanomaterials synthesis to take its many advantages, including wet chemistry based in aqueous solutions, low deposition temperature and relatively short deposition time. Lanthanoid cations (europium and terbium) dopants and their phen and ODA complex surface-functionalizing agents were introduced into ZnO nanowalls because of the characteristic red and green emissions of Eu(III) and Tb(III), respectively.

The growth mechanism, optoelectronic and photophysical properties of single-unit-cell thick quantum sheets were investigated in Chapter 3. By lowering the deposition temperature and adopting a p-type Si wafer as a substrate, the single-unit-cell thick ZnO quantum sheets were obtained without any pre- or post-growth treatment for the first time. In addition to widening of the energy band gap by more than 1.1 eV than the ZnO bulk value, emission spectra of quantum-confined ZnO nanosheets were successfully measured for the first time, and the results showed blue-shifts by 91 nm and 124 nm for the band-edge emission and defect emission respectively. Schematic diagram of the basic energy bands of quantum-confined ZnO quantum sheets was constructed by using XPS valence band spectra. Increasing the deposition time resulted in thicker stacks of ZnO quantum sheets, and the corresponding UV absorption spectra of these nanosheet stacks showed reduction in the widened band gap. We expect that these novel properties of single-unit-cell thick ZnO quantum sheets can be further explored, given the present facile fabrication technique of direct deposition on Si substrates (and thereby enabling the quantum sheet on Si architecture to be used as is), its ease of harvesting from the substrate, and its thickness uniformity, all of which enable individual quantum sheets to be used as the “perfect” building block for quantum sheet stacks.

In addition, trivalent europium (Chapter 4) and trivalent terbium (Chapter 5) cations were doped electrochemically into ZnO nanowalls supported on ITO-coated glass substrates. Upon embedment of lanthanoid cations, the nanowalls became thicker and their edges appeared dull. Depth-profiling XPS

results suggested that the common growth mechanism of 2-D ZnO nanostructures was not affected by doping and the dopants were distributed evenly in ZnO nanowalls. Excitation of the as-grown europium-doped ZnO nanowalls produced only emissions originating from the defects of ZnO. After extended studies of the photophysical properties of europium-doped ZnO nanowalls upon thermal annealing and surface functionalization by phen, we proposed a new cascade energy transfer mechanism from ZnO to trivalent europium cations mediated by phen. This new proposed energy transfer mechanism has provided better understanding of the photophysical properties of europium-doped wide band gap semiconducting materials previously based traditional energy transfer mechanism.

For terbium doping, electrochemically synthesized terbium-doped ZnO nanowalls showed characteristic terbium and ZnO emissions without any pre and post-growth adjustments for the first time. An energy transfer mechanism from the conducting band of ZnO to trivalent terbium cations was revealed by excitation spectra of terbium-doped ZnO nanowalls, which allowed us to construct a schematic energy level diagram. Terbium-doped ZnO nanowalls were also surface functionalized by RhB. These RhB/terbium-doped ZnO-nanowall hybrid structures were examined for potential chemosensing application based on the green emission of terbium-doped ZnO nanowalls. Intensity enhancement of RhB emission of the hybrid structure compared to the thin film of RhB was observed and the corresponding energy level diagram of the hybrid structure was obtained. This study provided new insights to the energy transfer mechanism of terbium-doped ZnO and its RhB hybrid structure.

Furthermore, europium and terbium ODA and phen complexes were synthesized and they were used for surface functionalization of ZnO nanowalls to build hybrid materials of lanthanoid complexes/ZnO (Chapter 6). The chemical bonding nature, particularly that at interfacial region, of the hybrid structures was investigated by XPS for the first time, and the results are consistent with chemisorption between lanthanoid complexes and ZnO nanowalls. Energy transfer mechanisms of these hybrid materials were similar to that of trivalent lanthanoid cation doped ZnO nanowalls. However, these hybrid materials showed substantial energy transfer efficiency of up to 90%. By comparing emission spectra and quantum yields, we conclude that hybrid materials of europium complex/ZnO nanowalls exhibited better luminescence properties than doping with trivalent europium cations. For terbium, it showed the opposite trend.

7.2 Proposed Future Work

In Chapter 3, we showed that ZnO quantum sheets have defect emission ranging from 350 nm to 500 nm and this opens new door for LED applications. With the ZnO nanosheets acting as the energy donor for trivalent europium and terbium cations, this defect emission has strong potential for developing blue LED. Blue LED based on ZnO quantum sheets is expected to have improved lifetime and stability than organic LED and more economically feasible than that based on GaN materials. In addition, excitation spectra of EuODA (Figure 6.1b) and TbODA (Figure 6.2b) have bigger overlaps with the defect emission of ZnO quantum sheets (Figure 3.5) than band-edge emission of ZnO nanowalls. Surface functionalization of ZnO quantum sheets by trivalent europium and terbium organic complexes will produce higher energy transfer efficiency and potentially yield better quantum yield than ZnO nanowalls. Exploring the use of other unique properties of ZnO quantum sheets such as electrical resistivity and diode properties for fabrication of ultrathin devices will also be potentially rewarding. Due to the large amount of defect and the single-unit-cell thickness, ZnO quantum sheets are expected to show similar electrical resistivity as graphene and graphene-like materials. Computational simulations on the electronic structure of these ultrathin ZnO nanostructures will be used to first provide initial estimates of magnitudes of these properties. Preliminary calculations based on Gaussian simulation package have been performed to determine the electronic band structure of bulk ZnO. The standard functions have thus far not been able to correctly determine the band gap, likely because of strongly localized d and f electrons.²⁶⁶ Adopting hybrid density functions with the Vienna ab-initio Simulation Package (VASP) is one of alternative methods to determine the electronic band structure of quantum-confined ZnO nanostructures. Combining optoelectronic and photophysical measurements of ZnO quantum sheets with these calculations will provide new insight to understand the properties of pristine ZnO quantum sheets and to estimate the properties of doped quantum sheets in an effort to design and develop the appropriate electronic structures for blue LED application.

In case of europium-doped ZnO nanowalls, reducing the amount of defect and increasing the concentration of europium cations will allow us to improve photophysical behavior of europium-doped ZnO nanowalls. Comparing the emission spectra of as-grown and thermally treated samples indirectly showed that the defects in the ZnO nanowalls could act as an obstacle to radiative relaxation and prevent generation of band-edge emission from the as-deposited nanowalls. By manipulating such deposition conditions as temperature, different combination and concentration of

electrolytes, and the applied voltage, the growth rate and mechanism could be precisely manipulated to produce nanowalls with different crystalline and structural quality and the resulting photophysical properties. For terbium-doped ZnO nanowalls, optimizing the electrochemical technique for deposition on a p-type Si wafer will also be of interest because p-type Si substrates, instead of the currently used ITO-glass substrates, will significantly reduce the steps in building a p-n junction for LED application.

In Chapter 6, this thesis performed complete investigation of chemical bonding of lanthanoid complexes and adsorption nature of hybrid structures. Computational studies involving geometrical optimization of lanthanoid complexes and of the interfacial region of the lanthanoid complex/ZnO hybrid nanostructures by VASP will be helpful in confirming chemical nature of hybrid structures obtained by XPS and PL. Moreover, introducing quasi hierarchical 3-D nanostructures (e.g. nanotrees) by combining hydrothermal and electrochemical deposition method will dramatically increase the specific surface area and the loading capacity for lanthanoid complexes. This will result in significant emission enhancement. Since the amount of lanthanoid complexes on ZnO nanowalls was only a few tenth of micrograms (Chapter 6) and lanthanoid cations have inherently excellent visible color representations, these heavily loaded hybrid nanostructures could potentially be commercially viable for use in the production of intense monochromatic red and green LEDs.

References

- (1) Badeker, K. Über Die Elektrische Leitfähigkeit Und Die Thermoelektrische Kraft Einiger Schwermetallverbindungen. *Ann. Phys.* **1907**, 327, 749–766.
- (2) Liu, H.; Avrutin, V.; Izyumskaya, N.; Özgür, Ü.; Morkoç, H.; Özgr, Ü.; Morkoç, H. Transparent Conducting Oxides for Electrode Applications in Light Emitting and Absorbing Devices. *Superlattices Microstruct.* **2010**, 48 (5), 458–484.
- (3) Moss, T. S. The Interpretation of the Properties of Indium Antimonide. *Proc. Phys. Soc. London B* **1954**, 67, 775–782.
- (4) Burstein, E. Anomalous Optical Absorption Limit in InSb. *Phys. Rev.* **1954**, 93 (3), 632–633.
- (5) Groth, R.; Kauer, E. Thermal Insulation of Sodium Lamps. *Phillips Tech. Rev.* **1965**, 26, 105.
- (6) Groth, R. Untersuchungen an Halbleitenden Indiumoxydschichten. *Phys. status solidi* **1966**, 14 (1), 69–75.
- (7) Maruyama, T.; Nakai, T. Fluorine-Doped Indium Oxide Thin Films Prepared by Chemical Vapor Deposition. *J. Appl. Phys.* **1992**, 71 (6), 2915–2917.
- (8) Pan, H.-C.; Shiao, M.-H.; Su, C.-Y.; Hsiao, C.-N. Influence of Sputtering Parameter on the Optical and Electrical Properties of Zinc-Doped Indium Oxide Thin Films. *J. Vac. Sci. Technol. A Vacuum, Surfaces, Film.* **2005**, 23 (4), 1187.
- (9) Meng, Y.; Yang, X.; Chen, H.; Shen, J.; Jiang, Y.; Zhang, Z.; Hua, Z. Molybdenum-Doped Indium Oxide Transparent Conductive Thin Films. *J. Vac. Sci. {&} Technol. A Vacuum, Surfaces, Film.* **2002**, 20 (1), 288.
- (10) Parthiban, S.; Gokulakrishnan, V.; Elangovan, E.; Gonçalves, G.; Ramamurthi, K.; Fortunato, E.; Martins, R. High Mobility and Visible-near Infrared Transparent Titanium Doped Indium Oxide Thin Films Produced by Spray Pyrolysis. *Thin Solid Films* **2012**, 524, 268–271.
- (11) Tuna, O.; Selamet, Y.; Aygun, G.; Ozyuzer, L. High Quality ITO Thin Films Grown by Dc and RF Sputtering without Oxygen. *J. Phys. D. Appl. Phys.* **2010**, 43 (5), 55402.
- (12) Ohta, H.; Orita, M.; Hirano, M.; Tanji, H.; Kawazoe, H.; Hosono, H. Highly Electrically Conductive Indium-Tin-Oxide Thin Films Epitaxially Grown on Ytria-Stabilized Zirconia

- (100) by Pulsed-Laser Deposition. *Appl. Phys. Lett.* **2000**, 76 (19), 2740–2742.
- (13) Kawashima, T.; Ezure, T.; Okada, K.; Matsui, H.; Goto, K.; Tanabe, N. FTO/ITO Double-Layered Transparent Conductive Oxide for Dye-Sensitized Solar Cells. *J. Photochem. Photobiol. A Chem.* **2004**, 164 (1-3), 199–202.
- (14) Dong, B.-Z.; Hu, H.; Fang, G.-J.; Zhao, X.-Z.; Zheng, D.-Y.; Sun, Y.-P. Comprehensive Investigation of Structural, Electrical, and Optical Properties for ZnO:Al Films Deposited at Different Substrate Temperature and Oxygen Ambient. *J. Appl. Phys.* **2008**, 103 (7), 73711.
- (15) Sheu, J.-K.; Lee, M.-L.; Lu, Y. S.; Shu, K. W. Ga-Doped ZnO Transparent Conductive Oxide Films Applied to GaN-Based Light-Emitting Diodes for Improving Light Extraction Efficiency. *IEEE J. Quantum Electron.* **2008**, 44 (12), 1211–1218.
- (16) Agura, H.; Suzuki, A.; Matsushita, T.; Aoki, T.; Okuda, M. Low Resistivity Transparent Conducting Al-Doped ZnO Films Prepared by Pulsed Laser Deposition. *Thin Solid Films* **2003**, 445 (2), 263–267.
- (17) Park, S.-M.; Ikegami, T.; Ebihara, K. Effects of Substrate Temperature on the Properties of Ga-Doped ZnO by Pulsed Laser Deposition. *Thin Solid Films* **2006**, 513 (1-2), 90–94.
- (18) Lv, M.; Xiu, X.; Pang, Z.; Dai, Y.; Ye, L.; Cheng, C.; Han, S. Structural, Electrical and Optical Properties of Zirconium-Doped Zinc Oxide Films Prepared by Radio Frequency Magnetron Sputtering. *Thin Solid Films* **2008**, 516 (8), 2017–2021.
- (19) Kumar, V.; Singh, R. G.; Purohit, L. P.; Mehra, R. M. Structural, Transport and Optical Properties of Boron-Doped Zinc Oxide Nanocrystalline. *J. Mater. Sci. Technol.* **2011**, 27 (6), 481–488.
- (20) Chung, J.-L.; Chen, J.-C.; Tseng, C.-J. Electrical and Optical Properties of TiO₂-Doped ZnO Films Prepared by Radio-Frequency Magnetron Sputtering. *J. Phys. Chem. Solids* **2008**, 69 (2-3), 535–539.
- (21) Survey, U. S. G. *Mineral Commodity Summaries 2015*; 2015.
- (22) U.S. Food and Drug Administration. *Database of Select Committee on GRAS Substances (SCOGS) Reviews*.
- (23) Cho, J.-S.; Koh, S.-K.; Yoon, K. H. Microstructure and Electrical Properties of Indium Oxide

Thin Films Prepared by Direct Oxygen Ion-Assisted Deposition. *J. Electrochem. Soc.* **2000**, *147* (3), 1065.

- (24) Ellmer, K. Resistivity of Polycrystalline Zinc Oxide Films: Current Status and Physical Limit. *J. Phys. D. Appl. Phys.* **2001**, *34* (21), 3097–3108.
- (25) Shamala, K. S.; Murthy, L. C. S.; Narasimha Rao, K. Studies on Tin Oxide Films Prepared by Electron Beam Evaporation and Spray Pyrolysis Methods. *Bull. Mater. Sci.* **2004**, *27* (3), 295–301.
- (26) Rakhshani, A. E.; Makdisi, Y.; Ramazaniyan, H. A. Electronic and Optical Properties of Fluorine-Doped Tin Oxide Films. *J. Appl. Phys.* **1998**, *83* (2), 1049.
- (27) Shanthi, S.; Subramanian, C.; Ramasamy, P. Growth and Characterization of Antimony Doped Tin Oxide Thin Films. *J. Cryst. Growth* **1999**, *197* (4), 858–864.
- (28) Luka, G.; Krajewski, T.; Wachnicki, L.; Witkowski, B.; Lusakowska, E.; Paszkowicz, W.; Guziewicz, E.; Godlewski, M. Transparent and Conductive Undoped Zinc Oxide Thin Films Grown by Atomic Layer Deposition. *Phys. Status Solidi* **2010**, *207* (7), 1568–1571.
- (29) Desgreniers, S. High-Density Phases of ZnO: Structural and Compressive Parameters. *Phys. Rev. B* **1998**, *58* (21), 14102–14105.
- (30) Kohan, A. F.; Ceder, G.; Morgan, D.; Van de Walle, C. G. First-Principles Study of Native Point Defects in ZnO. *Phys. Rev. B* **2000**, *61* (22), 15019–15027.
- (31) Tam, K. H.; Cheung, C. K.; Leung, Y. H.; Djurišić, A. B.; Ling, C. C.; Beling, C. D.; Fung, S.; Kwok, W. M.; Chan, W. K.; Phillips, D. L.; Ding, L.; Ge, W. K. Defects in ZnO Nanorods Prepared by a Hydrothermal Method. *J. Phys. Chem. B* **2006**, *110* (42), 20865–20871.
- (32) San, X.; Wang, G.; Liang, B.; Song, Y.; Gao, S.; Zhang, J.; Meng, F. Catalyst-Free Growth of One-Dimensional ZnO Nanostructures on SiO₂ Substrate and in Situ Investigation of Their H₂ Sensing Properties. *J. Alloys Compd.* **2015**, *622*, 73–78.
- (33) Carcia, P. F.; McLean, R. S.; Reilly, M. H.; Nunes, G. Transparent ZnO Thin-Film Transistor Fabricated by Rf Magnetron Sputtering. *Appl. Phys. Lett.* **2003**, *82* (7), 1117–1119.
- (34) Jia, C. H. H.; Wang, S.; Wu, Y. H. H.; Chen, Y. H. H.; Sun, X. W. W.; Zhang, W. F. F. Epitaxial Properties of ZnO Thin Films on LaAlO₃ Substrates by Pulsed Laser Deposition. *J.*

Cryst. Growth **2015**, *421*, 19–22.

- (35) Biroju, R. K.; Tilak, N.; Rajender, G.; Dhara, S.; Giri, P. K. Catalyst Free Growth of ZnO Nanowires on Graphene and Graphene Oxide and Its Enhanced Photoluminescence and Photoresponse. *Nanotechnology* **2015**, *26* (14), 145601.
- (36) Jabri, S.; Souissi, H.; Souissi, A.; Meftah, A.; Sallet, V.; Lusson, A.; Galtier, P.; Oueslati, M. Investigation of the Vibrational Modes of ZnO Grown by MOCVD on Different Orientation Planes. *J. Raman Spectrosc.* **2015**, *46* (2), 251–255.
- (37) Li, B. S.; Liu, Y. C.; Chu, Z. S.; Shen, D. Z.; Lu, Y. M.; Zhang, J. Y.; Fan, X. W. High Quality ZnO Thin Films Grown by Plasma Enhanced Chemical Vapor Deposition. *J. Appl. Phys.* **2002**, *91* (1), 501–505.
- (38) Pal, U.; Santiago, P. Controlling the Morphology of ZnO Nanostructures in a Low-Temperature Hydrothermal Process. *J. Phys. Chem. B* **2005**, *109* (32), 15317–15321.
- (39) Zheng, Y.; Zheng, L.; Zhan, Y.; Lin, X.; Zheng, Q.; Wei, K. Ag/ZnO Heterostructure Nanocrystals: Synthesis, Characterization, and Photocatalysis. *Inorg. Chem.* **2007**, *46* (17), 6980–6986.
- (40) Liu, B.; Zeng, H. C. Hydrothermal Synthesis of ZnO Nanorods in the Diameter Regime of 50 Nm. *J. Am. Chem. Soc.* **2003**, *125* (15), 4430–4431.
- (41) Lee, J.-H.; Ko, K.-H.; Park, B.-O. Electrical and Optical Properties of ZnO Transparent Conducting Films by the Sol–gel Method. *J. Cryst. Growth* **2003**, *247* (1-2), 119–125.
- (42) Zheng, M. J.; Zhang, L. D.; Li, G. H.; Shen, W. Z. Fabrication and Optical Properties of Large-Scale Uniform Zinc Oxide Nanowire Arrays by One-Step Electrochemical Deposition Technique. *Chem. Phys. Lett.* **2002**, *363*, 123–128.
- (43) Pradhan, D.; Leung, K. T. Controlled Growth of Two-Dimensional and One-Dimensional ZnO Nanostructures on Indium Tin Oxide Coated Glass by Direct Electrodeposition. *Langmuir* **2008**, *24* (17), 9707–9716.
- (44) Shen, Y.; Yan, X.; Bai, Z.; Zheng, X.; Sun, Y.; Liu, Y.; Lin, P.; Chen, X.; Zhang, Y. A Self-Powered Ultraviolet Photodetector Based on Solution-Processed P-NiO/n-ZnO Nanorod Array Heterojunction. *RSC Adv.* **2015**, *5* (8), 5976–5981.

- (45) Shi, Z.-F.; Zhang, Y.-T.; Cui, X.-J.; Zhuang, S.-W.; Wu, B.; Jiang, J.-Y.; Chu, X.-W.; Dong, X.; Zhang, B.-L.; Du, G.-T. Epitaxial Growth of Vertically Aligned ZnO Nanowires for Bidirectional Direct-Current Driven Light-Emitting Diodes Applications. *CrystEngComm* **2015**, *17* (1), 40–49.
- (46) Wang, D.; Wang, F.; Wang, Y.; Fan, Y.; Zhao, B.; Zhao, D. Interfacial Emission Adjustment in ZnO Quantum Dots/p-GaN Heterojunction Light-Emitting Diodes. *J. Phys. Chem. C* **2015**, *119* (5), 150126085805005.
- (47) Fu, Q. M.; Cao, W.; Li, G. W.; Lin, Z. D.; Chen, Z.; Xu, C. B.; Tu, Y. F.; Ma, Z. Bin. Blue/green Electroluminescence from a ZnO Nanorods/p-GaN Heterojunction Light Emitting Diode under Different Reverse Bias. *Appl. Surf. Sci.* **2014**, *293*, 225–228.
- (48) Park, C.; Lee, J.; So, H.-M.; Chang, W. S. An Ultrafast Response Grating Structural ZnO Photodetector with Back-to-Back Schottky Barriers Produced by Hydrothermal Growth. *J. Mater. Chem. C* **2015**, *3* (12), 2737–2743.
- (49) Alvi, N. H.; Usman Ali, S. M.; Hussain, S.; Nur, O.; Willander, M. Fabrication and Comparative Optical Characterization of n-ZnO Nanostructures (Nanowalls, Nanorods, Nanoflowers and Nanotubes)/p-GaN White-Light-Emitting Diodes. *Scr. Mater.* **2011**, *64* (8), 697–700.
- (50) Ko, S. H.; Lee, D.; Kang, H. W.; Nam, K. H.; Yeo, J. Y.; Hong, S. J.; Grigoropoulos, C. P.; Sung, H. J. Nanoforest of Hydrothermally Grown Hierarchical ZnO Nanowires for a High Efficiency Dye-Sensitized Solar Cell. *Nano Lett.* **2011**, *11* (2), 666–671.
- (51) Law, M.; Greene, L. E.; Johnson, J. C.; Saykally, R.; Yang, P. Nanowire Dye-Sensitized Solar Cells. *Nat. Mater.* **2005**, *4* (6), 455–459.
- (52) Maeda, K.; Takata, T.; Hara, M.; Saito, N.; Inoue, Y.; Kobayashi, H.; Domen, K. GaN:ZnO Solid Solution as a Photocatalyst for Visible-Light-Driven Overall Water Splitting. *J. Am. Chem. Soc.* **2005**, *127* (23), 8286–8287.
- (53) Ahmad, M.; Ahmed, E.; Hong, Z. L. L.; Xu, J. F. F.; Khalid, N. R. R.; Elhissi, A.; Ahmed, W. A Facile One-Step Approach to Synthesizing ZnO/graphene Composites for Enhanced Degradation of Methylene Blue under Visible Light. *Appl. Surf. Sci.* **2013**, *274*, 273–281.
- (54) Sakthivel, S.; Neppolian, B.; Shankar, M. V; Arabindoo, B.; Palanichamy, M.; Murugesan, V. Solar Photocatalytic Degradation of Azo Dye: Comparison of Photocatalytic Efficiency of ZnO and TiO₂. *Sol. Energy Mater. Sol. Cells* **2003**, *77* (1), 65–82.

- (55) Daneshvar, N.; Salari, D.; Khataee, a. R. Photocatalytic Degradation of Azo Dye Acid Red 14 in Water on ZnO as an Alternative Catalyst to TiO₂. *J. Photochem. Photobiol. A Chem.* **2004**, *162* (2-3), 317–322.
- (56) Fan, Z.; Wang, D.; Chang, P.-C. C.; Tseng, W.-Y. Y.; Lu, J. G. ZnO Nanowire Field-Effect Transistor and Oxygen Sensing Property. *Appl. Phys. Lett.* **2004**, *85* (24), 5923–5925.
- (57) Jing, Z.; Zhan, J. Fabrication and Gas-Sensing Properties of Porous ZnO Nanoplates. *Adv. Mater.* **2008**, *20* (23), 4547–4551.
- (58) Liao, L.; Lu, H. B.; Li, J. C.; He, H.; Wang, D. F.; Fu, D. J.; Liu, C.; Zhang, W. F. Size Dependence of Gas Sensitivity of ZnO Nanorods. *J. Phys. Chem. C* **2007**, *111* (5), 1900–1903.
- (59) Wang, J. X.; Sun, X. W.; Yang, Y.; Huang, H.; Lee, Y. C.; Tan, O. K.; Vayssieres, L. Hydrothermally Grown Oriented ZnO Nanorod Arrays for Gas Sensing Applications. *Nanotechnology* **2006**, *17* (19), 4995–4998.
- (60) Parks, G. A. The Isoelectric Points of Solid Oxides, Solid Hydroxides, And Aqueous Hydroxo Complex Systems. *Chem. Rev.* **1965**, *65* (2), 177–198.
- (61) Kong, T.; Chen, Y.; Ye, Y.; Zhang, K.; Wang, Z.; Wang, X. An Amperometric Glucose Biosensor Based on the Immobilization of Glucose Oxidase on the ZnO Nanotubes. *Sensors Actuators, B Chem.* **2009**, *138* (1), 344–350.
- (62) Xiang, C.; Zou, Y.; Sun, L. X.; Xu, F. Direct Electrochemistry and Enhanced Electrocatalysis of Horseradish Peroxidase Based on Flowerlike ZnO-Gold Nanoparticle-Nafion Nanocomposite. *Sensors Actuators, B Chem.* **2009**, *136* (1), 158–162.
- (63) Khan, R.; Kaushik, A.; Solanki, P. R.; Ansari, A. a.; Pandey, M. K.; Malhotra, B. D. Zinc Oxide Nanoparticles-Chitosan Composite Film for Cholesterol Biosensor. *Anal. Chim. Acta* **2008**, *616* (2), 207–213.
- (64) Li, Y. F.; Liu, Z. M.; Liu, Y. L.; Yang, Y. H.; Shen, G. L.; Yu, R. Q. A Mediator-Free Phenol Biosensor Based on Immobilizing Tyrosinase to ZnO Nanoparticles. *Anal. Biochem.* **2006**, *349* (1), 33–40.
- (65) International Union of Pure and Applied Chemistry. *Nomenclature of Inorganic Chemistry – IUPAC Recommendations 2005*; 2005; Vol. 27.

- (66) Urbain, G. Cathodic Phosphorescence of Europium. *C. R. Hebd. Seances Acad. Sci.* **1906**, *142*, 205–207.
- (67) Geusic, J. E.; Marcos, H. M.; Uiter, L. G. Van; Van Uiter, L. G. Laser Oscillations in Nd-Doped Yttrium Aluminum, Yttrium Gallium and Gadolinium Garnets. *Appl. Phys. Lett.* **1964**, *4* (10), 182–184.
- (68) Mears, R. J.; Reekie, L.; Jauncey, I. M.; Payne, D. N. Low-Noise Erbium-Doped Fibre Amplifier Operating at 1.54 μ m. *Electron. Lett.* **1987**, *23* (19), 1026.
- (69) Chan, E. M. Combinatorial Approaches for Developing Upconverting Nanomaterials: High-Throughput Screening, Modeling, and Applications. *Chem. Soc. Rev.* **2015**, *44* (6), 1653–1679.
- (70) Van Vleck, J. H. The Puzzle of Rare-earth Spectra in Solids. *J. Phys. Chem.* **1937**, *41*, 67–80.
- (71) Broer, L. J. F. J. F.; Gorter, C. J. J.; Hoogschagen, J. On the Intensities and the Multipole Character in the Spectra of the Rare Earth Ions. *Physica* **1945**, *11* (4), 231–250.
- (72) Sayre, E. V.; Freed, S. Spectra and Quantum States of the Europic Ion in Crystals. II. Fluorescence and Absorption Spectra of Single Crystals of Europic Ethylsulfate Nonahydrate. *J. Chem. Phys.* **1956**, *24* (6), 1213.
- (73) Peacock, R. D. The Intensities of Lanthanide f \leftrightarrow f Transitions. In *Structure and Bonding*; 1975; Vol. 22, pp 83–122.
- (74) Judd, B. R. Optical Absorption Intensities of Rare-Earth Ions. *Phys. Rev.* **1962**, *127* (3), 750–761.
- (75) Ofelt, G. S. Intensities of Crystal Spectra of Rare-Earth Ions. *J. Chem. Phys.* **1962**, *37* (3), 511–520.
- (76) Bu, J. G.; Bünzli, J.-C. G.; Piguet, C. Taking Advantage of Luminescent Lanthanide Ions. *Chem. Soc. Rev.* **2005**, *34* (12), 1048–1077.
- (77) Carnall, W. T. Electronic Energy Levels of the Trivalent Lanthanide Aquo Ions. IV. Eu³⁺. *J. Chem. Phys.* **1968**, *49* (10), 4450.
- (78) Carnall, W. T.; Fields, P. R.; Rajnak, K. Electronic Energy Levels in the Trivalent Lanthanide

- Aquo Ions. I. Pr^{3+} , Nd^{3+} , Pm^{3+} , Sm^{3+} , Dy^{3+} , Ho^{3+} , Er^{3+} , and Tm^{3+} . *J. Chem. Phys.* **1968**, *49* (10), 4424.
- (79) Carnall, W. T. Electronic Energy Levels of the Trivalent Lanthanide Aquo Ions. II. Gd^{3+} . *J. Chem. Phys.* **1968**, *49* (10), 4443.
- (80) Carnall, W. T. Electronic Energy Levels of the Trivalent Lanthanide Aquo Ions. III. Tb^{3+} . *J. Chem. Phys.* **1968**, *49* (10), 4447.
- (81) Bethe, H. Termaufspaltung in Kristallen. *Ann. Phys.* **1929**, *395* (2), 133–208.
- (82) Van Vleck, J. H. Theory of the Variations in Paramagnetic Anisotropy among Different Salts of the Iron Group. *Phys. Rev.* **1932**, *41* (1927), 208–215.
- (83) Görller-Walrand, C.; Binnemans, K. Chapter 167 Spectral Intensities of F-F Transitions. In *Handbook on the Physics and Chemistry of Rare Earths*, Vol. 25; 1998; pp 101–264.
- (84) Wybourne, B. G. *Spectroscopic Properties of Rare Earths*; John Wiley and Sons, Inc., 1965.
- (85) Freed, S. Spectra of Ions in Fields of Various Symmetry in Crystals and Solutions. *Rev. Mod. Phys.* **1942**, *14* (2-3), 105–111.
- (86) Moeller, T.; Brantley, J. C. Observations on the Rare Earths. LVIII. Reaction between Neodymium and Ethylenediaminetetraacetate Ions in Aqueous Solution. *J. Am. Chem. Soc.* **1950**, *72* (12), 5447–5451.
- (87) Jørgensen, C. K.; Judd, B. R. Hypersensitive Pseudoquadrupole Transitions in Lanthanides. *Mol. Phys.* **1964**, *8* (3), 281–290.
- (88) Judd, B. R. Ionic Transitions Hypersensitive to Environment. *J. Chem. Phys.* **1979**, *70* (1979), 4830–4833.
- (89) Reid, M. F.; Richardson, F. S. Electric Dipole Intensity Parameters for Lanthanide $4f \rightarrow 4f$ Transitions. *J. Chem. Phys.* **1983**, *79* (12), 5735.
- (90) Tanaka, M.; Nishimura, G.; Kushida, T. Contribution of J Mixing to the $^5\text{D}_0\text{-}^7\text{F}_0$ Transition of Eu^{3+} Ions in Several Host Matrices. *Phys. Rev. B* **1994**, *49* (24), 16917–16925.

- (91) Lowther, J. E.; Search, H.; Journals, C.; Contact, A.; Iopscience, M.; Phys, S. S.; Address, I. P. Spectroscopic Transition Probabilities of Rare Earth Ions. *J. Phys. C Solid State Phys.* **1974**, *7* (23), 4393–4402.
- (92) Xia, S.; Chen, Y. Effect of J-Mixing on the Intensities of F-F Transitions of Rare Earth Ions. *J. Lumin.* **1985**, *33* (2), 228–230.
- (93) Georges, J. Lanthanide-Sensitized Luminescence and Applications to the Determination of Organic Analytes. A Review. *Analyst* **1993**, *118* (12), 1481–1486.
- (94) Reisfeld, R.; Jørgensen, C. K. *Lasers and Excited States of Rare Earths*; Inorganic Chemistry Concepts; Springer Berlin Heidelberg: Berlin, Heidelberg, 1977; Vol. 1.
- (95) Richardson, F. S. Terbium(III) and Europium(III) Ions as Luminescent Probes and Stains for Biomolecular Systems. *Chem. Rev.* **1982**, *82* (5), 541–552.
- (96) Richardson, F. S.; Saxe, J. D.; Davis, S. A.; Faulkner, T. R. Intensity Calculations on Hypersensitive F-F Transitions in Nine-Coordinate Lanthanide Systems of Trigonal Symmetry. *Mol. Phys.* **1981**, *42* (6), 1401–1429.
- (97) Bünzli, J. C. G. Lanthanide Luminescence for Biomedical Analyses and Imaging. *Chem. Rev.* **2010**, *110* (5), 2729–2755.
- (98) Carnall, W. T. The Absorption and Fluorescence Spectra of Rare Earth Ions in Solution. In *Handbook on the Physics and Chemistry of Rare Earths*; 1979; pp 171–208.
- (99) Weissman, S. I. Intramolecular Energy Transfer. The Fluorescence of Complexes of Europium. *J. Chem. Phys.* **1942**, *10* (1942), 214–217.
- (100) Binnemans, K. Lanthanide-Based Luminescent Hybrid Materials. *Chem. Rev.* **2009**, *109* (9), 4283–4374.
- (101) Lakowicz, J. R. *Principles of Fluorescence Spectroscopy*, 3rd ed.; Lakowicz, J. R., Ed.; Springer US: Boston, MA, 2006.
- (102) Dexter, D. L. A Theory of Sensitized Luminescence in Solids. *J. Chem. Phys.* **1953**, *21* (5), 836.
- (103) Eliseeva, S. V.; Bünzli, J.-C. G. Lanthanide Luminescence for Functional Materials and Bio-

- Sciences. *Chem. Soc. Rev.* **2010**, 39 (1), 189–227.
- (104) Fields, R. A.; Birnbaum, M.; Fincher, C. L. Highly Efficient Nd:YVO₄ Diode-Laser End-Pumped Laser. *Appl. Phys. Lett.* **1987**, 51 (23), 1885–1886.
- (105) Li, Z. F.; Zhou, L.; Yu, J. B.; Zhang, H. J.; Deng, R. P.; Peng, Z. P.; Guo, Z. Y. Synthesis, Structure, Photoluminescence, and Electroluminescence Properties of a New Dysprosium Complex. *J. Phys. Chem. C* **2007**, 111 (5), 2295–2300.
- (106) Yu, J.; Zhang, H.; Zhou, L.; Deng, R.; Peng, Z.; Li, Z.; Fu, L.; Guo, Z. Efficient Organic Electroluminescent Devices Based on an Organosamarium Complex. *J. Lumin.* **2007**, 122-123 (1-2), 678–682.
- (107) Chen, Z.; Deng, Z.; Shi, Y.; Xu, Y.; Xiao, J.; Zhang, Y.; Wang, R. Electroluminescent Devices Based on Rare-Earth Complex TbY(p-MBA)₆(phen)₂. *J. Lumin.* **2007**, 122-123 (1-2), 671–673.
- (108) Zheng, X. L.; Liu, Y.; Pan, M.; Lü, X. Q.; Zhang, J. Y.; Zhao, C. Y.; Tong, Y. X.; Su, C. Y. Bright Blue-Emitting Ce³⁺ Complexes with Encapsulating Polybenzimidazole Tripodal Ligands as Potential Electroluminescent Devices. *Angew. Chemie - Int. Ed.* **2007**, 46 (39), 7399–7403.
- (109) Xu, H.; Yin, K.; Huang, W. Comparison of the Electrochemical and Luminescence Properties of Two Carbazole-Based Phosphine Oxide EuIII Complexes: Effect of Different Bipolar Ligand Structures. *ChemPhysChem* **2008**, 9 (12), 1752–1760.
- (110) Setlur, A. a; Heward, W. J.; Hannah, M. E.; Happek, U. Incorporation of Si⁴⁺–N³⁻ into Ce³⁺-Doped Garnets for Warm White LED Phosphors. *Chem. Mater.* **2008**, 20 (19), 6277–6283.
- (111) Gouveia-Neto, a. S.; Da Silva, a. F.; Bueno, L. a.; Da Costa, E. B. Luminescent Features of Solgel Derived Rare-Earth Multi-Doped Oxyfluoride Nano-Structured Phosphors for White LED Application. *J. Lumin.* **2012**, 132 (2), 299–304.
- (112) Selvalakshmi, T.; Bose, A. C.; Velmathi, S. Influence of Al³⁺ on the Cross Relaxation Process and Electrical Properties of Dy³⁺ Activated Gd₂O₃ Phosphor for White LED Application. *Ceram. Int.* **2015**, 41 (7), 8801–8808.
- (113) Kuriki, K.; Koike, Y.; Okamoto, Y. Plastic Optical Fiber Lasers and Amplifiers Containing Lanthanide Complexes. *Chem. Rev.* **2002**, 102 (6), 2347–2356.

- (114) Elliott, R. J. *Magnetic Properties of Rare Earth Metals*; Plenum Press: London, 1972.
- (115) Li, Y.; Beija, M.; Laurent, S.; Elst, L. Vander; Muller, R. N.; Duong, H. T. T.; Lowe, A. B.; Davis, T. P.; Boyer, C. Macromolecular Ligands for Gadolinium MRI Contrast Agents. *Macromolecules* **2012**, *45* (10), 4196–4204.
- (116) Rinehart, J. D.; Fang, M.; Evans, W. J.; Long, J. R. Strong Exchange and Magnetic Blocking in N_2^{3-} -Radical-Bridged Lanthanide Complexes. *Nat. Chem.* **2011**, *3* (7), 538–542.
- (117) Bogani, L.; Wernsdorfer, W. Molecular Spintronics Using Single-Molecule Magnets. *Nat. Mater.* **2008**, *7* (3), 179–186.
- (118) Kim, T.-Y.; Hong, N. H.; Sugawara, T.; Raghavender, A. T.; Kurisu, M. Room Temperature Ferromagnetism with Large Magnetic Moment at Low Field in Rare-Earth-Doped $BiFeO_3$ Thin Films. *J. Phys. Condens. Matter* **2013**, *25* (20), 206003.
- (119) Xu, C. X.; Sun, X. W.; Zhang, X. H.; Ke, L.; Chua, S. J. Photoluminescent Properties of Copper-Doped Zinc Oxide Nanowires. *Nanotechnology* **2004**, *15* (7), 856–861.
- (120) Yan, X.; Hu, D.; Li, H.; Li, L.; Chong, X.; Wang, Y. Nanostructure and Optical Properties of M Doped ZnO (M=Ni, Mn) Thin Films Prepared by Solgel Process. *Phys. B Condens. Matter* **2011**, *406* (20), 3956–3962.
- (121) Li, J.; Fan, H.; Jia, X.; Yang, W.; Fang, P. Enhanced Blue-Green Emission and Ethanol Sensing of Co-Doped ZnO Nanocrystals Prepared by a Solvothermal Route. *Appl. Phys. A Mater. Sci. Process.* **2010**, *98* (3), 537–542.
- (122) Farag, A. A. M.; Cavaş, M.; Yakuphanoglu, F.; Amanullah, F. M. Photoluminescence and Optical Properties of Nanostructure Ni Doped ZnO Thin Films Prepared by Sol-gel Spin Coating Technique. *J. Alloys Compd.* **2011**, *509* (30), 7900–7908.
- (123) Terai, Y.; Yamaoka, K.; Yoshida, K.; Tsuji, T.; Fujiwara, Y. Photoluminescence Properties of Eu-Doped ZnO Films Grown by Sputtering-Assisted Metalorganic Chemical Vapor Deposition. *Phys. E Low-Dimensional Syst. Nanostructures* **2010**, *42* (10), 2834–2836.
- (124) Liu, Y.; Luo, W.; Li, R.; Liu, G.; Antonio, M. R.; Chen, X. Optical Spectroscopy of Eu^{3+} Doped ZnO Nanocrystals. *J. Phys. Chem. C* **2009**, *113* (13), 5340.
- (125) Du, Y. P.; Zhang, Y. W.; Sun, L. D.; Yan, C. H. Efficient Energy Transfer in Monodisperse

Eu-Doped ZnO Nanocrystals Synthesized from Metal Acetylacetonates in High-Boiling Solvents. *J. Phys. Chem. C* **2008**, *112* (32), 12234–12241.

- (126) Zeng, X.; Yuan, J.; Wang, Z.; Zhang, L. Nanosheet-Based Microspheres of Eu³⁺-Doped ZnO with Efficient Energy Transfer from ZnO to Eu³⁺ at Room Temperature. *Adv. Mater.* **2007**, *19* (24), 4510–4514.
- (127) Kabongo, G. L.; Mhlongo, G. H.; Malwela, T.; Mothudi, B. M.; Hillie, K. T.; Dhlamini, M. S. Microstructural and Photoluminescence Properties of Sol–gel Derived Tb³⁺ Doped ZnO Nanocrystals. *J. Alloys Compd.* **2014**, *591*, 156–163.
- (128) Pal, P. P.; Manam, J. Photoluminescence and Thermoluminescence Studies of Tb³⁺ Doped ZnO Nanorods. *Mater. Sci. Eng. B Solid-State Mater. Adv. Technol.* **2013**, *178* (7), 400–408.
- (129) Bayan, S.; Das, U.; Mohanta, D. Development of Tb-Doped ZnO Nanorods: Effect of Nitrogen Ion Irradiation on Luminescence and Structural Evolution. *Phys. Status Solidi* **2010**, *207* (8), 1859–1863.
- (130) Zhao, S.; Wang, L.; Yang, L.; Wang, Z. Synthesis and Luminescence Properties of ZnO:Tb³⁺ Nanotube Arrays via Electrodeposited Method. *Phys. B Condens. Matter* **2010**, *405* (15), 3200–3204.
- (131) Li, F. M. M.; Li, X. B. B.; Ma, S. Y. Y.; Chen, L.; Li, W. Q. Q.; Zhu, C. T. T.; Xu, X. L. L.; Chen, Y.; Li, Y. F. F.; Lawson, G. Influence of Ce Doping on Microstructure of ZnO Nanoparticles and Their Acetone Sensing Properties. *J. Alloys Compd.* **2015**, *649*, 1136–1144.
- (132) Jayachandriah, C.; Siva Kumar, K.; Krishnaiah, G.; Madhusudhana Rao, N. Influence of Dy Dopant on Structural and Photoluminescence of Dy-Doped ZnO Nanoparticles. *J. Alloys Compd.* **2015**, *623*, 248–254.
- (133) Sin, J. C.; Lam, S. M.; Lee, K. T.; Mohamed, A. R. Photocatalytic Performance of Novel Samarium-Doped Spherical-like ZnO Hierarchical Nanostructures under Visible Light Irradiation for 2,4-Dichlorophenol Degradation. *J. Colloid Interface Sci.* **2013**, *401*, 40–49.
- (134) Zeng, X.; Yuan, J.; Zhang, L. Synthesis and Photoluminescent Properties of Rare Earth Doped ZnO Hierarchical Microspheres. *J. Phys. Chem. C* **2008**, *112*, 3503–3508.
- (135) Cheng, B. C.; Xiao, Y. H.; Wu, G. S.; Zhang, L. D. Controlled Growth and Properties of One-Dimensional ZnO Nanostructures with Ce as Activator/Dopant. *Adv. Funct. Mater.* **2004**, *14* (9), 913–919.

- (136) Lin, K.-F.; Cheng, H.-M.; Hsu, H.-C.; Lin, L.-J.; Hsieh, W.-F. Band Gap Variation of Size-Controlled ZnO Quantum Dots Synthesized by Sol-gel Method. *Chem. Phys. Lett.* **2005**, *409* (4-6), 208–211.
- (137) Yanhong, L.; Dejun, W.; Qidong, Z.; Min, Y.; Qinglin, Z. A Study of Quantum Confinement Properties of Photogenerated Charges in ZnO Nanoparticles by Surface Photovoltage Spectroscopy. *J. Phys. Chem. B* **2004**, *108* (10), 3202–3206.
- (138) Kim, K.-K.; Koguchi, N.; Ok, Y.-W.; Seong, T.-Y.; Park, S.-J. Fabrication of ZnO Quantum Dots Embedded in an Amorphous Oxide Layer. *Appl. Phys. Lett.* **2004**, *84* (19), 3810.
- (139) Fang, Y.; Pang, Q.; Wen, X.; Wang, J.; Yang, S. Synthesis of Ultrathin ZnO Nanofibers Aligned on a Zinc Substrate. *Small* **2006**, *2* (5), 612–615.
- (140) Pan, A.; Yu, R.; Xie, S.; Zhang, Z.; Jin, C.; Zou, B. ZnO Flowers Made up of Thin Nanosheets and Their Optical Properties. *J. Cryst. Growth* **2005**, *282* (1-2), 165–172.
- (141) Bard, A. J.; Faulkner, L. R. *Electrochemical Methods: Fundamentals and Applications*, 2nd ed.; John Wiley and Sons, Inc.: New York, 2001.
- (142) Standard Hydrogen Electrode. In *IUPAC Compendium of Chemical Terminology*; McNaught, A. D., Wilkinson, A., Eds.; Blackwell Scientific Publications: Oxford, 1997; Vol. 955, p 5917.
- (143) Trasatti, S. The Absolute Electrode Potential: An Explanatory Note (Recommendations 1986). *Pure Appl. Chem.* **1986**, *58* (7), 955–966.
- (144) Brandon, D.; Kaplan, W. D. *Microstructural Characterization of Materials*, 2nd ed.; John Wiley and Sons, Inc.: Chichester, 2008.
- (145) *Surface Analysis– The Principal Techniques*, 2nd ed.; Vickerman, J. C., Gilmore, I. S., Eds.; John Wiley and Sons, Inc.: Chichester, UK, 2009.
- (146) Watts, J. F.; Wolstenholme, J. *An Introduction to Surface Analysis by XPS and AES*; John Wiley and Sons, Inc.: Chichester, UK, 2003.
- (147) Auger, P. Sur L'effet Photoélectrique Composé. *J. Phys. le Radium* **1925**, *6* (6), 205–208.

- (148) Kubelka, P.; Munk, F. Ein Beitrag Zur Optik Der Farbanstriche. *Z. Tehc. Phys.* **1931**, *12*, 593–601.
- (149) Hecht, H. G. The Interpretation of Diffuse Reflectance Spectra. *J. Res. NBS A Phys. Ch.* **1976**, *80* (4), 567–583.
- (150) Molenaar, R.; ten Bosch, J. J.; Zijp, J. R. Determination of Kubelka-Munk Scattering and Absorption Coefficients by Diffuse Illumination. *Appl. Opt.* **1999**, *38* (10), 2068–2077.
- (151) Mello, J. C. de; Wittmann, H. F.; Friend, R. H. An Improved Experimental Determination of External Photoluminescence Quantum Efficiency. *Adv. Mater.* **1997**, *9* (3), 230–232.
- (152) Bawendi, M. G.; Steigerwald, M. L.; Brus, L. E. The Quantum Mechanics Of Larger Semiconductor Clusters (“Quantum Dots”). *Annu. Rev. Phys. Chem.* **1990**, *41* (1), 477–496.
- (153) Cui, Y.-T.; Moore, R. G.; Zhang, A.-M.; Tian, Y.; Lee, J. J.; Schmitt, F. T.; Zhang, W.-H.; Li, W.; Yi, M.; Liu, Z.-K.; Hashimoto, M.; Zhang, Y.; Lu, D.-H.; Devereaux, T. P.; Wang, L.-L.; Ma, X.-C.; Zhang, Q.-M.; Xue, Q.-K.; Lee, D.-H.; Shen, Z.-X. Interface Ferroelectric Transition near the Gap-Opening Temperature in a Single-Unit-Cell FeSe Film Grown on Nb-Doped SrTiO₃ Substrate. *Phys. Rev. Lett.* **2015**, *114* (3), 37002.
- (154) Yu, T.; Joo, J.; Park, Y. Il; Hyeon, T. Single Unit Cell Thick Samaria Nanowires and Nanoplates. *J. Am. Chem. Soc.* **2006**, *128* (6), 1786–1787.
- (155) Huang, H.; Yu, Q.; Peng, X.; Ye, Z. Single-Unit-Cell Thick Mn₃O₄ Nanosheets. *Chem. Commun.* **2011**, *47* (48), 12831.
- (156) Patra, P.; Mitra, S.; Das Gupta, A.; Pradhan, S.; Bhattacharya, S.; Ahir, M.; Mukherjee, S.; Sarkar, S.; Roy, S.; Chattopadhyay, S.; Adhikary, A.; Goswami, A.; Chattopadhyay, D. Simple Synthesis of Biocompatible Biotinylated Porous Hexagonal ZnO Nanodisc for Targeted Doxorubicin Delivery against Breast Cancer Cell: In Vitro and in Vivo Cytotoxic Potential. *Colloids Surfaces B Biointerfaces* **2015**, *133*, 88–98.
- (157) Djurišić, A. B.; Chen, X.; Leung, Y. H.; Man Ching Ng, A. ZnO Nanostructures: Growth, Properties and Applications. *J. Mater. Chem.* **2012**, *22* (14), 6526.
- (158) Article, R.; Klingshirn, C. ZnO: From Basics towards Applications. *Phys. Status Solidi* **2007**, *244* (9), 3027–3073.

- (159) Huang, C.; Shi, R.; Amini, A.; Wu, Z.; Xu, S.; Zhang, L.; Cao, W.; Feng, J.; Song, H.; Shi, Y.; Wang, N.; Cheng, C. Hierarchical ZnO Nanostructures with Blooming Flowers Driven by Screw Dislocations. *Sci. Rep.* **2015**, *5*, 8226.
- (160) Choi, J. H.; Garay, A. A.; Hwang, S. M.; Chung, C. W. Influence of Oxygen on Characteristics of Zn(O,S) Thin Films Deposited by RF Magnetron Sputtering. *J. Vac. Sci. Technol. A Vacuum, Surfaces, Film.* **2015**, *33* (4), 040603.
- (161) Sun, Y.; Fuge, G. M.; Ashfold, M. N. R. Growth of Aligned ZnO Nanorod Arrays by Catalyst-Free Pulsed Laser Deposition Methods. *Chem. Phys. Lett.* **2004**, *396* (1-3), 21–26.
- (162) Park, W. Il; Yi, G. C.; Kim, M.; Pennycook, S. J. ZnO Nanoneedles Grown Vertically on Si Substrates by Non-Catalytic Vapor-Phase Epitaxy. *Adv. Mater.* **2002**, *14* (24), 1841–1843.
- (163) Liu, X. Growth Mechanism and Properties of ZnO Nanorods Synthesized by Plasma-Enhanced Chemical Vapor Deposition. *J. Appl. Phys.* **2004**, *95* (6), 3141.
- (164) Ayudhya, S. K. N.; Tonto, P.; Mekasuwandumrong, O.; Pavarajarn, V.; Praserttham, P.; Kunjara Na Ayudhya, S. Solvothermal Synthesis of ZnO with Various Aspect Ratios Using Organic Solvents. *Cryst. Growth {&} Des.* **2006**, *6* (11), 2446–2450.
- (165) Holloway, T.; Mundle, R.; Dondapati, H.; Bahoura, M.; a.K. Pradhan. Aligned Al:ZnO Nanorods on Si with Different Barrier Layers for Optoelectronic Applications. *Chem. Phys. Lett.* **2012**, *534* (3), 48–53.
- (166) Peulon, S.; Lincot, D. Cathodic Electrodeposition from Aqueous Solution of Dense or Open-Structured Zinc Oxide Films. *Adv. Mater.* **1996**, *8* (2), 166.
- (167) Park, W. Il; Yi, G. C.; Kim, M.; Pennycook, S. J. Quantum Confinement Observed in ZnO/ZnMgO Nanorod Heterostructures. *Adv. Mater.* **2003**, *15* (6), 526–529.
- (168) Esken, D.; Noei, H.; Wang, Y.; Wiktor, C.; Turner, S.; Van Tendeloo, G.; Fischer, R. a.; Chem, J. M.; Esken, D.; Noei, H.; Wang, Y.; Wiktor, C.; Turner, S.; Tendeloo, V.; Fischer, R. a. ZnO@ZIF-8: Stabilization of Quantum Confined ZnO Nanoparticles by a Zinc Methylimidazolate Framework and Their Surface Structural Characterization Probed by CO₂ Adsorption. *J. Mater. Chem.* **2011**, *21*, 5907.
- (169) Ng, H. T.; Chen, B.; Li, J.; Han, J.; Meyyappan, M.; Wu, J.; Li, S. X.; Haller, E. E. Optical Properties of Single-Crystalline ZnO Nanowires on M-Sapphire. *Appl. Phys. Lett.* **2003**, *82* (13), 2023.

- (170) Senger, R. T.; Bajaj, K. K. Optical Properties of Confined Polaronic Excitons in Spherical Ionic Quantum Dots. *Phys. Rev. B* **2003**, *68* (4), 45313.
- (171) Izaki, M.; Omi, T. Electrolyte Optimization for Cathodic Growth of Zinc Oxide Films. *J. Electrochem. Soc.* **1996**, *143* (3), L53–L55.
- (172) Peulon, S. Mechanistic Study of Cathodic Electrodeposition of Zinc Oxide and Zinc Hydroxychloride Films from Oxygenated Aqueous Zinc Chloride Solutions. *J. Electrochem. Soc.* **1998**, *145* (3), 864.
- (173) Moulder, J. F.; Stickle, W. F.; Sobol, P. E.; Bomben, K. D. *Handbook of X-Ray Photoelectron Spectroscopy*; Perkin-Elmer Corporation: Eden Prairie, MN, 1992.
- (174) Tena-Zaera, R.; Elias, J.; Wang, G.; Lévy-Clément, C. Role of Chloride Ions on Electrochemical Deposition of ZnO Nanowire Arrays from O₂ Reduction. *J. Phys. Chem. C* **2007**, *111* (45), 16706–16711.
- (175) Wang, D.; Xing, G.; Gao, M.; Yang, L.; Yang, J.; Wu, T. Defects-Mediated Energy Transfer in Red-Light-Emitting Eu-Doped ZnO Nanowire Arrays. *J. Phys. Chem.* **2011**, 22729–22735.
- (176) Pal, P. P.; Manam, J. Color Tunable ZnO Nanorods by Eu³⁺ and Tb³⁺ Co-Doping for Optoelectronic Applications. *Appl. Phys. A* **2014**, *116* (1), 213–223.
- (177) Li, G. R.; Dawa, C. R.; Lu, X. H.; Yu, X. L.; Tong, Y. X. Use of Additives in the Electrodeposition of Nanostructured Eu³⁺/ZnO Films for Photoluminescent Devices. *Langmuir* **2009**, *25* (21), 2378–2384.
- (178) Ishizumi, A.; Kanemitsu, Y. Structural and Luminescence Properties of Eu-Doped ZnO Nanorods Fabricated by a Microemulsion Method. *Appl. Phys. Lett.* **2005**, *86* (25), 1–3.
- (179) Ohtake, T.; Hijii, S.; Sonoyama, N.; Sakata, T. Electrochemical Luminescence of n-Type ZnO Semiconductor Electrodes Doped with Rare Earth Metals under the Anodic Polarization. *Appl. Surf. Sci.* **2006**, *253* (4), 1753–1757.
- (180) Mote, V. D. Synthesis and Characterization of Cr Doped ZnO Nanocrystals. *World J. Condens. Matter Phys.* **2012**, *02* (04), 208–211.
- (181) Abdullah, K. Al; Bakour, B. Semiconductors Elaboration/ZnO Based Varistors for Improving

of Stability and Reliability of Electrical Systems Applications by Using the Rare-Earths. *Energy Procedia* **2012**, *19*, 1–14.

- (182) Yang, L.; Wang, Z.; Zhang, Z.; Sun, Y.; Gao, M.; Yang, J.; Yan, Y. Surface Effects on the Optical and Photocatalytic Properties of Graphene-like ZnO:Eu³⁺ Nanosheets. *J. Appl. Phys.* **2013**, *113* (3).
- (183) Lotey, G. S.; Singh, J.; Verma, N. K. Room Temperature Ferromagnetism in Tb-Doped ZnO Dilute Magnetic Semiconducting Nanoparticles. *J. Mater. Sci. Mater. Electron.* **2013**, *24* (9), 3611–3616.
- (184) Sin, J. C.; Lam, S. M.; Lee, K. T.; Mohamed, A. R. Preparation of Rare Earth-Doped ZnO Hierarchical Micro/nanospheres and Their Enhanced Photocatalytic Activity under Visible Light Irradiation. *Ceram. Int.* **2014**, *40* (4), 5431–5440.
- (185) Santos, G.; Dutra, J. D. L.; Junior, S. a; Freire, R. O.; Nivan, B.; Junior, C. Theoretical Spectroscopic Study of Europium Tris (Bipyridine) Cryptates. **2012**.
- (186) Tanner, P. a; Li, W.; Ning, L. Electronic Spectra and Crystal-Field Analysis of Europium in Hexanitritolanthanate Systems. *Inorg. Chem.* **2012**, *51* (5), 2997–3006.
- (187) Ma, Y.; Wang, Y. Recent Advances in the Sensitized Luminescence of Organic Europium Complexes. *Coord. Chem. Rev.* **2010**, *254* (9–10), 972–990.
- (188) Katsuki, D.; Sato, T.; Suzuki, R. Red Luminescence of Eu³⁺ Doped ZnO Nanoparticles Fabricated by Laser Ablation in Aqueous Solution. *Appl. Phys.* **2012**, 321–327.
- (189) Zhao, S.; Shu, F.; Li, Y.; Liu, C.; Shan, W.; Cui, Y.; Yang, L. Synthesis and Luminescence Properties of ZnO:Eu³⁺ Nano Crystalline via a Facile Solution Method. *J. Nanosci. Nanotechnol.* **2012**, *12* (3), 2607–2611.
- (190) Ortega, Y.; Fernández, P.; Piqueras, J. Growth and Cathodoluminescence of Eu Doped ZnO Nanoneedles and Branched Nanoneedle Structures. *J. Nanosci. Nanotechnol.* **2010**, *10* (1), 502–507.
- (191) Wang, M.; Huang, C.; Huang, Z.; Guo, W.; Huang, J.; He, H.; Wang, H.; Cao, Y.; Liu, Q.; Liang, J. Synthesis and Photoluminescence of Eu-Doped ZnO Microrods Prepared by Hydrothermal Method. *Opt. Mater. (Amst).* **2009**, *31* (10), 1502–1505.

- (192) Yang, Y.; Lai, H.; Tao, C.; Yang, H. Correlation of Luminescent Properties of ZnO and Eu Doped ZnO Nanorods. *J. Mater. Sci. Mater. Electron.* **2010**, *21*, 173–178.
- (193) Pan, C. J.; Chen, C. W.; Chen, J. Y.; Huang, P. J.; Chi, G. C.; Chang, C. Y.; Ren, F.; Pearton, S. J. Optical and Structural Properties of Eu-Diffused and Doped ZnO Nanowires. *Appl. Surf. Sci.* **2009**, *256* (1), 187–190.
- (194) Ebisawa, K.; Okuno, T.; Abe, K.; Zno, E. Photoluminescence Properties of Eu³⁺-Doped ZnO Nanoneedles. *Jpn. J. Appl. Phys.* **2008**, *47* (9), 7236–7238.
- (195) Tanner, P. A.; Yu, L. Photoluminescence of ZnO:Eu³⁺ Nanoflower. *J. Nanosci. Nanotechnol.* **2008**, *8* (3), 1307–1311.
- (196) Ashtaputre, S. S.; Nojima, a; Marathe, S. K.; Matsumura, D.; Ohta, T.; Tiwari, R.; Dey, G. K.; Kulkarni, S. K. Investigations of White Light Emitting Europium Doped Zinc Oxide Nanoparticles. *J. Phys. D. Appl. Phys.* **2007**, *41* (1), 15301.
- (197) Ishizumi, a; Takahashi, Y.; Yamamoto, a; Kanemitsu, Y. Fabrication and Optical Properties of Eu³⁺-Doped ZnO Nanospheres and Nanorods. *Mater. Sci. Eng. B* **2008**, *146* (1–3), 212–215.
- (198) Pauporte, T.; Pelle, F.; Supe, Ä. N. Luminescence of Nanostructured Eu³⁺/ZnO Mixed Films Prepared by Electrodeposition. *Society* **2007**, 15427–15432.
- (199) Joshi, B. N.; Yoon, H.; Kim, H. Y.; Oh, J. H.; Seong, T. Y.; James, S. C.; Yoon, S. S. Effect of Zinc Acetate Concentration on Structural, Optical and Electrical Properties of ZnO Thin Films Deposited by Electrostatic Spray on an ITO Substrate. *J. Electrochem. Soc.* **2012**, *159* (8), H716–H721.
- (200) Singh, T.; Pandya, D. K.; Singh, R. Concentration Dependent Structural and Optical Properties of Electrochemically Grown ZnO Thin Films and Nanostructures. *Appl. Surf. Sci.* **2013**, *270*, 578–583.
- (201) Inguanta, R.; Garlisi, C.; Spanò, T.; Piazza, S.; Sunseri, C. Growth and Photoelectrochemical Behaviour of Electrodeposited ZnO Thin Films for Solar Cells. *J. Appl. Electrochem.* **2013**, *43* (2), 199–208.
- (202) Kim, Y. J.; Shang, H.; Cao, G. Growth and Characterization of [001] ZnO Nanorod Array on ITO Substrate with Electric Field Assisted Nucleation. *J. Sol-Gel Sci. Technol.* **2006**, *38* (1), 79–84.

- (203) Hsu, C.-L.; Chang, S.-J.; Lin, Y.-R.; Wu, J.-M.; Lin, T.-S.; Tsai, S.-Y.; Chen, I.-C. Indium-Diffused ZnO Nanowires Synthesized on ITO-Buffered Si Substrate. *Nanotechnology* **2005**, *17* (2), 516–519.
- (204) Lupan, O.; Guérin, V. M. M.; Tiginyanu, I. M. M.; Ursaki, V. V. V; Chow, L.; Heinrich, H.; Pauporté, T. Well-Aligned Arrays of Vertically Oriented ZnO Nanowires Electrodeposited on ITO-Coated Glass and Their Integration in Dye Sensitized Solar Cells. *J. Photochem. Photobiol. A Chem.* **2010**, *211* (1), 65–73.
- (205) Venkatachalam, S.; Hayashi, H.; Ebina, T.; Nakamura, T.; Wakui, Y.; Nanjo, H. Preparation and Characterization of Epitaxial Growth of ZnO Nanotip Arrays by Hydrothermal Method. *J. Colloid Interface Sci.* **2013**, *395*, 64–67.
- (206) Wu, H.; Xue, M.; Ou, J.; Wang, F.; Li, W. Effect of Annealing Temperature on Surface Morphology and Work Function of ZnO Nanorod Arrays. *J. Alloys Compd.* **2013**, *565*, 85–89.
- (207) Teng, X.; Fan, H.; Pan, S.; Ye, C.; Li, G. Abnormal Photoluminescence of ZnO Thin Film on ITO Glass. *Mater. Lett.* **2007**, *61* (1), 201–204.
- (208) Ahn, C. H.; Kim, Y. Y.; Kim, D. C.; Mohanta, S. K.; Cho, H. K. A Comparative Analysis of Deep Level Emission in ZnO Layers Deposited by Various Methods. *J. Appl. Phys.* **2009**, *105* (1), 1–6.
- (209) Özgür, U.; Alivov, Y. I.; Liu, C.; Teke, A.; Reshchikov, M. A.; Doğan, S.; Avrutin, V.; Cho, S.-J.; Morkoç, H. A Comprehensive Review of ZnO Materials and Devices. *J. Appl. Phys.* **2005**, *98* (4), 041301.
- (210) Fan, J.; Gu, F.; Fa, C.; Fairbrother, A.; Andreu, T.; Lo, A. M.; Ramo, J.; Cabot, A.; Güell, F.; Fábrega, C.; Fairbrother, A.; Andreu, T.; López, A. M.; Morante, J. R.; Cabot, A. Visible Photoluminescence Components of Solution-Grown ZnO Nanowires: Influence of the Surface Depletion Layer. *J. Phys. Chem. C* **2012**, *116* (36), 19496–19502.
- (211) Zhou, H.; Alves, H.; Hofmann, D. M.; Kriegseis, W.; Meyer, B. K.; Kaczmarczyk, G.; Hoffmann, a. Behind the Weak Excitonic Emission of ZnO Quantum Dots: ZnO/Zn(OH)₂ Core-Shell Structure. *Appl. Phys. Lett.* **2002**, *80* (2), 210–212.
- (212) Norberg, N. S.; Gamelin, D. R. Influence of Surface Modification on the Luminescence of Colloidal ZnO Nanocrystals. *J. Phys. Chem. B* **2005**, *109*, 20810–20816.

- (213) Pradhan, D.; Leung, K. T. Vertical Growth of Two-Dimensional Zinc Oxide Nanostructures on ITO-Coated Glass: Effects of Deposition Temperature and Deposition Time. *J. Phys. Chem. C* **2008**, *112* (5), 1357–1364.
- (214) Han, M.; Oh, S.-J.; Park, J. H.; Park, H. L. X-Ray Photoelectron Spectroscopy Study of CaS:Eu and SrS:Eu Phosphors. *J. Appl. Phys.* **1993**, *73* (9), 4546.
- (215) Kang, J.-G.; Kim, T.-J.; Kang, H.-J.; Kang, S. K. Crystal Structures and Luminescence Properties of [Eu(ODA)·(phen)·4H₂O]⁺, [Tb(ODA)·(phen)·4H₂O]⁺ and [Tb(ODA)₃]³⁻ (ODA: Oxydiacetate, Phen: 1,10-Phenanthroline). *J. Photochem. Photobiol. A Chem.* **2005**, *174* (1), 28–37.
- (216) Lee, J. C.; Choi, K.-S.; Cho, H.-K.; Kang, J.-G. Synthesis and Luminescence of Eu(III) Complexes with Macrocyclic Azacrown Ethers and 1,10-Phenanthroline. *J. Lumin.* **2007**, *127* (2), 332–338.
- (217) Chen, R.; Ye, Q. L.; He, T.; Ta, V. D.; Ying, Y.; Tay, Y. Y.; Wu, T.; Sun, H. Exciton Localization and Optical Properties Improvement in Nanocrystal-Embedded ZnO Core-Shell Nanowires. *Nano Lett.* **2013**, *13* (2), 734–739.
- (218) Hassan, N. K.; Hashim, M. R.; Al-Douri, Y. Morphology and Optical Investigations of ZnO Pyramids and Nanoflakes for Optoelectronic Applications. *Opt. - Int. J. Light Electron Opt.* **2014**, *125* (11), 2560–2564.
- (219) Liao, X.; Yan, X.; Lin, P.; Lu, S.; Tian, Y.; Zhang, Y. Enhanced Performance of ZnO Piezotronic Pressure Sensor through Electron-Tunneling Modulation of MgO Nanolayer. *ACS Appl. Mater. Interfaces* **2015**, *7* (3), 1602–1607.
- (220) Zhao, J.; Zhang, W.; An, X.; Liu, Z.; Xie, E.; Yang, C.; Chen, L. Room-Temperature Ferromagnetism in ZnO Nanoparticles by Electrospinning. *Nanosci. Nanotechnol. Lett.* **2014**, *6* (5), 446–449.
- (221) Ansari, S. A.; Khan, M. M.; Ansari, M. O.; Lee, J.; Cho, M. H. Biogenic Synthesis, Photocatalytic, and Photoelectrochemical Performance of Ag – ZnO Nanocomposite. **2013**.
- (222) Son, D. I.; Kwon, B. W.; Park, D. H.; Seo, W.-S.; Yi, Y.; Angadi, B.; Lee, C.-L.; Choi, W. K. Emissive ZnO–graphene Quantum Dots for White-Light-Emitting Diodes. *Nat. Nanotechnol.* **2012**, *7* (7), 465–471.
- (223) Zhang, C.; Marvinney, C. E.; Xu, H. Y.; Liu, W. Z.; Wang, C. L.; Zhang, L. X.; Wang, J. N.;

- Ma, J. G.; Liu, Y. C. Enhanced Waveguide-Type Ultraviolet Electroluminescence from ZnO/MgZnO Core/shell Nanorod Array Light-Emitting Diodes via Coupling with Ag Nanoparticles Localized Surface Plasmons. *Nanoscale* **2014**, *7* (3), 1073–1080.
- (224) Zamiri, R.; Kaushal, A.; Rebelo, A.; Ferreira, J. M. F. Er Doped ZnO Nanoplates: Synthesis, Optical and Dielectric Properties. *Ceram. Int.* **2014**, *40* (1), 1635–1639.
- (225) Chen, Q.; Wang, J. Ferromagnetism in Nd-Doped ZnO Nanowires and the Influence of Oxygen Vacancies: Ab Initio Calculations. *Phys. Chem. Chem. Phys.* **2013**, *15* (41), 17793.
- (226) Ji, S.; Yin, L.; Liu, G.; Zhang, L.; Ye, C. A Facile Method for Effective Doping of Tb³⁺ into ZnO Nanocrystals. *Chem. Commun.* **2009**, No. 17, 2344.
- (227) Kang, J.-S.; Jeong, Y.-K.; Kang, J.-G.; Zhao, L.; Sohn, Y.; Pradhan, D.; Leung, K. T. Observation of Mediated Cascade Energy Transfer in Europium-Doped ZnO Nanowalls by 1,10-Phenanthroline. *J. Phys. Chem. C* **2015**, *119* (4), 2142–2147.
- (228) Lupan, O.; Pauporté, T.; Viana, B.; Aschehoug, P.; Ahmadi, M.; Cuenya, B. R.; Rudzevich, Y.; Lin, Y.; Chow, L. Eu-Doped ZnO Nanowire Arrays Grown by Electrodeposition. *Appl. Surf. Sci.* **2013**, *282*, 782–788.
- (229) Li, G.; Lu, X.; Su, C.; Tong, Y. Facile Synthesis of Hierarchical ZnO : Tb³⁺ Nanorod Bundles and Their Optical and Magnetic Properties. *J. Phys. Chem. C* **2008**, 2927–2933.
- (230) Sharma, a.; Dhar, S.; Singh, B. P.; Kundu, T.; Spasova, M.; Farle, M. Influence of Tb Doping on the Luminescence Characteristics of ZnO Nanoparticles. *J. Nanoparticle Res.* **2012**, *14* (2), 676.
- (231) Xiao, X. H.; Ren, F.; Zhou, X. D.; Peng, T. C.; Wu, W.; Peng, X. N.; Yu, X. F.; Jiang, C. Z. Surface Plasmon-Enhanced Light Emission Using Silver Nanoparticles Embedded in ZnO. *Appl. Phys. Lett.* **2010**, *97* (7), 71909.
- (232) Lin, Y.; Liu, X. Q.; Wang, T.; Chen, C.; Wu, H.; Liao, L.; Liu, C. Shape-Dependent Localized Surface Plasmon Enhanced UV-Emission from ZnO Grown by Atomic Layer Deposition. *Nanotechnology* **2013**, *24* (12), 125705.
- (233) Ko, C.-T.; Han, Y.-Y.; Chen, C.-H.; Shieh, J.; Chen, M.-J. Enormous Plasmonic Enhancement and Suppressed Quenching of Luminescence from Nanoscale ZnO Films by Uniformly Dispersed Atomic-Layer-Deposited Platinum with Optimized Spacer Thickness. *J. Phys. Chem. C* **2013**, *117* (49), 26204–26212.

- (234) Yoo, J.; Kim, J.-H.; Lee, K.; Lee, S.; Kim, S. S.-W.; Park, H.-K.; Kim, S. S.-W.; Bae, J.; Park, J.-J.; Choi, D. Dewetted Gold Nanoparticles on ZnO Nanorods for Three-Dimensionally Distributed Plasmonic Hot Spots. *Scr. Mater.* **2013**, *69* (9), 654–657.
- (235) Narayanan, R.; Deepa, M.; Srivastava, A. K.; Shivaprasad, S. M. Efficient Plasmonic Dye-Sensitized Solar Cells with Fluorescent Au-Encapsulated C-Dots. *ChemPhysChem* **2014**, *15* (6), 1106–1115.
- (236) Cheng, C. W.; Sie, E. J.; Liu, B.; Huan, C. H. A.; Sum, T. C.; Sun, H. D.; Fan, H. J. Surface Plasmon Enhanced Band Edge Luminescence of ZnO Nanorods by Capping Au Nanoparticles. *Appl. Phys. Lett.* **2010**, *96* (7), 71107.
- (237) Zhang, X.; Xia, Y.; He, T. Tuning Photoluminescence Properties of ZnO Nanorods via Surface Modification. *Mater. Chem. Phys.* **2012**, *137* (2), 622–627.
- (238) Gupta, A.; Kim, B. C.; Edwards, E.; Brantley, C.; Ruffin, P. Covalent Functionalization of Zinc Oxide Nanowires for High Sensitivity P-Nitrophenol Detection in Biological Systems. *Mater. Sci. Eng. B* **2012**, *177* (18), 1583–1588.
- (239) Sato, M.; Shimatani, K.; Iwasaki, Y.; Morito, S.; Tanaka, H.; Fujita, Y.; Nakamura, M. New Surface-Modified Zinc Oxide Nanoparticles with Aminotriethylene Oxide Chains Linked by 1,2,3-Triazole Ring: Preparation, and Visible Light-Emitting and Noncytotoxic Properties. *Appl. Surf. Sci.* **2011**, *258* (2), 786–790.
- (240) Kim, J.; Jeong, Y.; Sohn, Y.; Kang, J. Synthesis and Photophysical Properties of an Eu(II)-Complex/PS Blend: Role of Ag Nanoparticles in Surface-Enhanced Luminescence. *Langmuir* **2012**, *28* (25), 9842–9848.
- (241) Nishimura, F.; Kim, J.-H.; Yonezawa, S.; Takashima, M. Auger Electron Spectroscopy for Chemical State and Quantitative Analysis of Terbium Containing Oxide Fluoride Glasses. *J. Fluor. Chem.* **2014**, *160*, 52–56.
- (242) Appavoo, K.; Liu, M.; Sfeir, M. Y. Role of Size and Defects in Ultrafast Broadband Emission Dynamics of ZnO Nanostructures. *Appl. Phys. Lett.* **2014**, *104* (13), 133101.
- (243) Stein, G.; Würzberg, E. Energy Gap Law in the Solvent Isotope Effect on Radiationless Transitions of Rare Earth Ions. *J. Chem. Phys.* **1975**, *62* (1), 208–213.

- (244) Chang, S. L.; Park, M. C.; Kuang, Q.; Deng, Y.; Sood, A. K.; Polla, D. L.; Wang, Z. L. Giant Enhancement in UV Response of ZnO Nanobelts by Polymer Surface-Functionalization. *J. Am. Chem. Soc.* **2007**, *129* (40), 12096–12097.
- (245) Zhang, B.; Kong, T.; Xu, W.; Su, R.; Gao, Y.; Cheng, G.; Monolayers, S.; Zhang, B.; Kong, T.; Xu, W.; Su, R.; Gao, Y.; Cheng, G. Surface Functionalization of Zinc Oxide by Carboxyalkylphosphonic Acid Self-Assembled Monolayers. *Langmuir* **2010**, *26* (6), 4514–4522.
- (246) Costenaro, D.; Carniato, F.; Gatti, G.; Marchese, L.; Bisio, C. Preparation of Luminescent ZnO Nanoparticles Modified with Aminopropyltriethoxy Silane for Optoelectronic Applications. *New J. Chem.* **2013**, *37* (7), 2103.
- (247) Klaumünzer, M.; Kahnt, A.; Burger, A.; Mačković, M.; Münzel, C.; Srikantharajah, R.; Spiecker, E.; Hirsch, A.; Peukert, W.; Guldi, D. M. Surface Functionalization and Electronic Interactions of ZnO Nanorods with a Porphyrin Derivative. *ACS Appl. Mater. Interfaces* **2014**, *6* (9), 6724–6730.
- (248) Jiang, X.; Wang, H.; Yuan, R.; Chai, Y. Sensitive Electrochemiluminescence Detection for CA15-3 Based on Immobilizing Luminol on Dendrimer Functionalized ZnO Nanorods. *Biosens. Bioelectron.* **2015**, *63*, 33–38.
- (249) Patra, S.; Roy, E.; Madhuri, R.; Sharma, P. K. Imprinted ZnO Nanostructure-Based Electrochemical Sensing of Calcitonin: A Clinical Marker for Medullary Thyroid Carcinoma. *Anal. Chim. Acta* **2015**, *853*, 271–284.
- (250) Čepin, M.; Jovanovski, V.; Podlogar, M.; Orel, Z. C. Amino- and Ionic Liquid-Functionalised Nanocrystalline ZnO via Silane Anchoring – an Antimicrobial Synergy. *J. Mater. Chem. B* **2015**, *3* (6), 1059–1067.
- (251) Sangermano, M.; Vitale, A.; Dietliker, K. Photolabile Amines Producing a Strong Base as Photocatalyst for the in-Situ Preparation of Organic–inorganic Hybrid Coatings. *Polymer (Guildf)*. **2014**, *55* (7), 1628–1635.
- (252) Ibupoto, Z. H.; Mitrou, N.; Nikoleli, G.-P.; Nikolelis, D. P.; Willander, M.; Psaroudakis, N. The Development of Highly Sensitive and Selective Immunosensor Based on Antibody Immobilized ZnO Nanorods for the Detection of D-Dimer. *Electroanalysis* **2014**, *26* (2), 292–298.
- (253) Scott Bohle, D.; Spina, C. J. Cationic and Anionic Surface Binding Sites on Nanocrystalline Zinc Oxide: Surface Influence on Photoluminescence and Photocatalysis. *J. Am. Chem. Soc.*

2009, 131 (12), 4397–4404.

- (254) Beane, G. a.; Morfa, A. J.; Funston, A. M.; Mulvaney, P. Defect-Mediated Energy Transfer between ZnO Nanocrystals and a Conjugated Dye. *J. Phys. Chem. C* **2012**, 116 (5), 3305–3310.
- (255) Park, J. K.; Lee, K. W.; Lee, W.; Lee, C. E. Nonradiative Energy Transfer in ZnO Nanorods/dye-Doped Polymer Heterostructures. *Appl. Phys. Lett.* **2009**, 94 (23), 233301.
- (256) Rakshit, S.; Vasudevan, S. Resonance Energy Transfer from Beta-Cyclodextrin-Capped ZnO:MgO Nanocrystals to Included Nile Red Guest Molecules in Aqueous Media. *ACS Nano* **2008**, 2 (7), 1473–1479.
- (257) Main, K.; Shimada, R.; Fujita, Y.; Neogi, A. Energy Transfer Induced Enhancement of Localized Exciton Emission in ZnO Nanoparticle-Anthracene Hybrid Films. *Phys. status solidi - Rapid Res. Lett.* **2013**, 7 (12), 1089–1092.
- (258) Shimada, R.; Urban, B.; Sharma, M.; Singh, A.; Avrutin, V.; Morkoç, H.; Neogi, A. Energy Transfer in ZnO-Anthracene Hybrid Structure. *Opt. Mater. Express* **2012**, 2 (5), 526.
- (259) Nash, K. L. Aqueous Complexes in Separations of f-elements: Options and Strategies for Future Development. *Sep. Sci. Technol.* **1999**, 34 (6-7), 911–929.
- (260) Kang, J.-G.; Kim, T.-J.; Kang, H.-J.; Park, Y.; Nah, M.-K. Structural and Luminescence Properties of $[\text{Ln}(\text{ODA})(\text{phen})\cdot 4\text{H}_2\text{O}]^+$ Complexes (Ln=Sm and Dy, ODA=oxydiacetate, phen=1,10-Phenanthroline). *J. Lumin.* **2008**, 128 (12), 1867–1872.
- (261) Sammes, P. G.; Yahioğlu, G. 1,10-Phenanthroline: A Versatile Ligand. *Chem. Soc. Rev.* **1994**, 23 (5), 327.
- (262) Fronczek, F. R.; Banerjee, A. K.; Watkins, S. F.; Schwartz, R. W. Absolute Configuration and Circular Dichroism of the Lanthanide Complex: trisodiumtris(oxydiacetato)europate(III) Bis(sodium Tetrafluoroborate) Hexahydrate. *Inorg. Chem.* **1981**, 20 (8), 2745–2746.
- (263) Albin, M.; Whittle, R. R.; Horrocks, W. D. Laser Spectroscopic and X-Ray Structural Investigation of europium(III)-Oxydiacetate Complexes in Solution and in the Solid State. *Inorg. Chem.* **1985**, 24 (26), 4591–4594.
- (264) Mirochnik, a G.; Bukvetskii, B. V.; Zhikhareva, P. a; Karasev, V. E. Crystal Structure and

Luminescence of the [Eu(Phen)₂(NO₃)₃] Complex. The Role of the Ion-Coactivator. *Russ. J. Coord. Chem.* **2001**, 27 (6), 443–448.

- (265) Wu, P. G.; Brand, L. Resonance Energy Transfer: Methods and Applications. *Anal. Biochem.* **1994**, 218 (1), 1–13.
- (266) Wróbel, J.; Kurzydłowski, K. J.; Hummer, K.; Kresse, G.; Piechota, J. Calculations of ZnO Properties Using the Heyd-Scuseria-Ernzerhof Screened Hybrid Density Functional. *Phys. Rev. B* **2009**, 80 (15), 155124.

Appendix A

Copyright Permissions

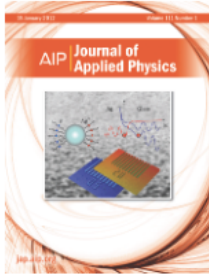
Figure 1.1:

10/31/2015 Rightslink® by Copyright Clearance Center



RightsLink®

[Home](#)
[Account Info](#)
[Help](#)

Title: A comprehensive review of ZnO materials and devices

Author: Ü. Özgür, Ya. I. Alivov, C. Liu, et al.

Publication: Journal of Applied Physics

Volume/Issue: 98/4

Publisher: AIP Publishing LLC

Date: Aug 30, 2005

Page Count: 103

Rights managed by AIP Publishing LLC.

Logged in as:
Jung-Soo Kang

Account #:
3000954321

LOGOUT

Order Completed

Thank you very much for your order.

Click [here](#) for Payment Terms and Conditions.

[Get a printable version for your records.](#)

License Number	3739390869304
Order Date	Oct 31, 2015
Publisher	AIP Publishing LLC
Publication	Journal of Applied Physics
Article Title	A comprehensive review of ZnO materials and devices
Author	Ü. Özgür, Ya. I. Alivov, C. Liu, et al.
Online Publication Date	Aug 30, 2005
Volume number	98
Issue number	4
Type of Use	Thesis/Dissertation
Requestor type	Student
Format	Print and electronic
Portion	Figure/Table
Number of figures/tables	1
Title of your thesis / dissertation	Photophysical and Optoelectronic Properties of Pristine, Doped and Surface-Functionalized Two-Dimensional Zinc Oxide Nanostructures
Expected completion date	Jan 2016
Estimated size (number of pages)	100
Total	0.00 USD

[ORDER MORE...](#)
[CLOSE WINDOW](#)

Copyright © 2015 [Copyright Clearance Center, Inc.](#) All Rights Reserved. [Privacy statement](#), [Terms and Conditions](#).
Comments? We would like to hear from you. E-mail us at customercare@copyright.com

Figure 1.2 and 1.3:

10/31/2015 Rightslink® by Copyright Clearance Center

 **Copyright Clearance Center**
Most Trusted. Most Cited. Most Read.

RightsLink®

[Home](#) [Account Info](#) [Help](#)  **Live Chat**

 **ACS Publications** **Title:** Defects in ZnO Nanorods Prepared by a Hydrothermal Method
Most Trusted. Most Cited. Most Read.

Author: K. H. Tam, C. K. Cheung, Y. H. Leung, et al

Publication: The Journal of Physical Chemistry B

Publisher: American Chemical Society

Date: Oct 1, 2006

Logged in as:
Jung-Soo Kang
Account #: 3000954321

[LOGOUT](#)

Copyright © 2006, American Chemical Society

PERMISSION/LICENSE IS GRANTED FOR YOUR ORDER AT NO CHARGE

This type of permission/license, instead of the standard Terms & Conditions, is sent to you because no fee is being charged for your order. Please note the following:

- Permission is granted for your request in both print and electronic formats, and translations.
- If figures and/or tables were requested, they may be adapted or used in part.
- Please print this page for your records and send a copy of it to your publisher/graduate school.
- Appropriate credit for the requested material should be given as follows: "Reprinted (adapted) with permission from (COMPLETE REFERENCE CITATION). Copyright (YEAR) American Chemical Society." Insert appropriate information in place of the capitalized words.
- One-time permission is granted only for the use specified in your request. No additional uses are granted (such as derivative works or other editions). For any other uses, please submit a new request.

If credit is given to another source for the material you requested, permission must be obtained from that source.

[BACK](#)

[CLOSE WINDOW](#)

Copyright © 2015 [Copyright Clearance Center, Inc.](#) All Rights Reserved. [Privacy statement](#), [Terms and Conditions](#).
Comments? We would like to hear from you. E-mail us at customercare@copyright.com

Figure 1.4:

10/31/2015 Rightslink® by Copyright Clearance Center

 **Copyright Clearance Center**

 **RightsLink®**

[Home](#) [Account Info](#) [Help](#)  **Live Chat**

 **ACS Publications** Most Trusted. Most Cited. Most Read.

Title: Controlled Growth of Two-Dimensional and One-Dimensional ZnO Nanostructures on Indium Tin Oxide Coated Glass by Direct Electrodeposition

Author: Debabrata Pradhan, Kam Tong Leung

Publication: Langmuir

Publisher: American Chemical Society

Date: Sep 1, 2008

Copyright © 2008, American Chemical Society

Logged in as:
Jung-Soo Kang
Account #:
3000954321

[LOGOUT](#)

PERMISSION/LICENSE IS GRANTED FOR YOUR ORDER AT NO CHARGE

This type of permission/license, instead of the standard Terms & Conditions, is sent to you because no fee is being charged for your order. Please note the following:

- Permission is granted for your request in both print and electronic formats, and translations.
- If figures and/or tables were requested, they may be adapted or used in part.
- Please print this page for your records and send a copy of it to your publisher/graduate school.
- Appropriate credit for the requested material should be given as follows: "Reprinted (adapted) with permission from (COMPLETE REFERENCE CITATION). Copyright (YEAR) American Chemical Society." Insert appropriate information in place of the capitalized words.
- One-time permission is granted only for the use specified in your request. No additional uses are granted (such as derivative works or other editions). For any other uses, please submit a new request.

If credit is given to another source for the material you requested, permission must be obtained from that source.

[BACK](#)

[CLOSE WINDOW](#)

Copyright © 2015 [Copyright Clearance Center, Inc.](#) All Rights Reserved. [Privacy statement](#). [Terms and Conditions](#).
Comments? We would like to hear from you. E-mail us at customer@copyright.com

Figure 1.5:

10/31/2015 Rightslink® by Copyright Clearance Center

 **Copyright Clearance Center**
Most Trusted. Most Cited. Most Read.

RightsLink®

[Home](#) [Account Info](#) [Help](#)  **Live Chat**

 **ACS Publications** **Title:** Nanoforest of Hydrothermally Grown Hierarchical ZnO Nanowires for a High Efficiency Dye-Sensitized Solar Cell

Author: Seung Hwan Ko, Daeho Lee, Hyun Wook Kang, et al

Publication: Nano Letters

Publisher: American Chemical Society

Date: Feb 1, 2011

Logged in as:
Jung-Soo Kang
Account # :
3000954321

[LOGOUT](#)

Copyright © 2011, American Chemical Society

PERMISSION/LICENSE IS GRANTED FOR YOUR ORDER AT NO CHARGE

This type of permission/license, instead of the standard Terms & Conditions, is sent to you because no fee is being charged for your order. Please note the following:

- Permission is granted for your request in both print and electronic formats, and translations.
- If figures and/or tables were requested, they may be adapted or used in part.
- Please print this page for your records and send a copy of it to your publisher/graduate school.
- Appropriate credit for the requested material should be given as follows: "Reprinted (adapted) with permission from (COMPLETE REFERENCE CITATION). Copyright (YEAR) American Chemical Society." Insert appropriate information in place of the capitalized words.
- One-time permission is granted only for the use specified in your request. No additional uses are granted (such as derivative works or other editions). For any other uses, please submit a new request.

If credit is given to another source for the material you requested, permission must be obtained from that source.

[BACK](#)

[CLOSE WINDOW](#)

Copyright © 2015 [Copyright Clearance Center, Inc.](#) All Rights Reserved. [Privacy statement](#), [Terms and Conditions](#).
Comments? We would like to hear from you. E-mail us at customercare@copyright.com

Chapter 4:

10/31/2015

Rightslink® by Copyright Clearance Center



RightsLink®

[Home](#)[Account Info](#)[Help](#)

ACS Publications
Most Trusted. Most Cited. Most Read.

Title: Observation of Mediated Cascade Energy Transfer in Europium-Doped ZnO Nanowalls by 1,10-Phenanthroline

Logged in as:
Jung-Soo Kang
Account #:
3000954321

Author: Jung-Soo Kang, Yong-Kwang Jeong, Jun-Gill Kang, et al

[LOGOUT](#)

Publication: The Journal of Physical Chemistry C

Publisher: American Chemical Society

Date: Jan 1, 2015

Copyright © 2015, American Chemical Society

PERMISSION/LICENSE IS GRANTED FOR YOUR ORDER AT NO CHARGE

This type of permission/license, instead of the standard Terms & Conditions, is sent to you because no fee is being charged for your order. Please note the following:

- Permission is granted for your request in both print and electronic formats, and translations.
- If figures and/or tables were requested, they may be adapted or used in part.
- Please print this page for your records and send a copy of it to your publisher/graduate school.
- Appropriate credit for the requested material should be given as follows: "Reprinted (adapted) with permission from (COMPLETE REFERENCE CITATION). Copyright (YEAR) American Chemical Society." Insert appropriate information in place of the capitalized words.
- One-time permission is granted only for the use specified in your request. No additional uses are granted (such as derivative works or other editions). For any other uses, please submit a new request.

[BACK](#)[CLOSE WINDOW](#)

Copyright © 2015 [Copyright Clearance Center, Inc.](#) All Rights Reserved. [Privacy statement.](#) [Terms and Conditions.](#) Comments? We would like to hear from you. E-mail us at customercare@copyright.com